LANDOLT-BÖRNSTEIN

Numerical Data and Functional Relationships in Science and Technology

New Series

Editor in Chief: K.-H. Hellwege

Group III: Crystal and Solid State Physics

Volume 4
Magnetic and Other Properties of Oxides and Related Compounds

Part a

J. B. Goodenough · W. Gräper · F. Holtzberg · D. L. Huber
R. A. Lefever · J. M. Longo · T. R. McGuire · S. Methfessel

Editors: K.-H. Hellwege and A. M. Hellwege

Springer-Verlag Berlin · Heidelberg · New York 1970

LANDOLT-BÖRNSTEIN

Zahlenwerte und Funktionen
aus Naturwissenschaften und Technik

Neue Serie

Gesamtherausgabe: K.-H. Hellwege

Gruppe III: Kristall- und Festkörperphysik

Band 4
Magnetische und andere Eigenschaften von Oxiden und verwandten Verbindungen

Teil a

J. B. Goodenough · W. Gräper · F. Holtzberg · D. L. Huber
R. A. Lefever · J. M. Longo · T. R. McGuire · S. Methfessel

Herausgeber: K.-H. Hellwege und A. M. Hellwege

1970 Springer-Verlag Berlin · Heidelberg · New York 1970

3 Crystallographic and magnetic properties of perovskite and perovskite-related compounds *)

3.0 Introduction — Einleitung

3.0.1 General remarks – Allgemeines

The perovskites form a family of compounds having a crystal structure similar to that of the mineral perovskite, $CaTiO_3$. There are two classes of materials crystallizing with this general structure type: primarily ionic materials having the ideal chemical formula ABX_3, (A = larger cation, B = smaller cation, X = anion), and alloys having the ideal formula $M^cXM^f_3$, (X = interstitial atom, M^c and M^f are metal atoms). Of these two classes, the former is much larger and the more important.

The stability of the ABX_3 perovskite structure is primarily derived from the electrostatic (Madelung) energy achieved if cations occupy corner-shared octahedra. Thus the first prerequisite for a stable ABX_3 perovskite is the existence of stable, polar octahedral-site building blocks. This, in turn, requires that the B cation have a preference for octahedral coordination and that there be an effective charge on the B cation. Since any A cation must occupy the relatively large anionic interstice created by corner-shared octahedra, a second prerequisite is an appropriate size for the A cation. Where it is too large, the B-X bond length cannot be optimized, and hexagonal stacking with face-shared octahedra becomes competitive. Where the A cation is too small, A-X bonding stabilizes structures having a smaller anionic coordination about the A cation. Thus ABX_3 perovskites are commonly found in fluorides and oxides having B cations with a preference energy for octahedral coordination. By contrast, the chlorides and sulfides, having larger anions, not only require the largest A cations, but also form layer structures, where the A cations are missing, because they have anionic *d* orbitals energetically available for orbital hybridization.

There are many perovskite-related structures, and these have been included in these tables. For example, the structure can tolerate mixed systems such as $A_{1-x}A'_xBX_3$ and $AB_{1-x}B'_xX_3$, A-cationic vacancies □ as in $□_{1-x}A_xBX_3$, and cationic ordering as in $A_2BB'X_6$. Although anion-deficient perovskites have been reported many times, the anion vacancies ⊕ are probably not distributed randomly. In compounds containing Fe^{3+} ions, for example, they appear to condense in pairs at individual *B*-site octahedra to convert the local anion interstice from an octahedron to a tetrahedron. In

Die Perowskite sind eine Gruppe von Verbindungen mit der gleichen Kristallstruktur wie das Mineral Perowskit, $CaTiO_3$. Man unterscheidet zwei Klassen von Substanzen, die in diesem allgemeinen Strukturtyp kristallisieren: in erster Linie Ionenverbindungen mit der idealen chemischen Formel ABX_3 (A = größeres Kation, B = kleineres Kation, X = Anion) und Legierungen mit der idealen Formel $M^cXM^f_3$ (X = Zwischengitteratom, M^c und M^f = Metallatome). Von diesen beiden Klassen ist die erstere wesentlich umfangreicher und wichtiger.

Die Stabilität der ABX_3-Perowskitstruktur beruht in erster Linie auf der elektrostatischen (Madelung-) Energie, die dann zustande kommt, wenn Kationen Oktaeder mit gemeinsamen Ecken besetzen. So ist die Existenz von stabilen, polaren Oktaeder-Bausteinen die erste Vorbedingung für ein stabiles ABX_3-Perowskit. Dies wiederum erfordert, daß das B-Kation die Oktaeder-Koordination bevorzugt und daß beim B-Kation eine effektive Ladung existiert. Da ein jedes A-Kation die relativ große Anionen-Lücke besetzen muß, die zwischen Oktaedern mit gemeinsamen Ecken entsteht, ist die passende Größe des A-Kations die zweite Vorbedingung. Wenn das A-Kation zu groß ist, läßt sich der optimale B-X-Bindungsabstand nicht erreichen, und eine hexagonale Packung von Oktaedern mit gemeinsamen Flächen kann ebenso auftreten. Wenn das A-Kation zu klein ist, ergibt die A-X-Bindung Strukturen mit einer kleineren Anionen-Koordination um das A-Kation. Daher sind ABX_3-Perowskite gewöhnlich unter den Fluoriden und Oxiden zu finden, in denen die B-Kationen Oktaeder-Koordination energetisch bevorzugen. Dagegen erfordern Chloride und Sulfide, die größere Anionen haben, nicht nur die größten A-Kationen, sondern sie bilden, weil sie anionische *d*-Elektronenbahnen mit der richtigen Energie für eine Bahn-Hybridisierung haben, auch Schichtstrukturen, bei denen die A-Kationen ganz fehlen.

Es gibt viele dem Perowskit verwandte Strukturen, die in diese Tabellen aufgenommen wurden. Zum Beispiel können gemischte Systeme wie $A_{1-x}A'_xBX_3$ und $AB_{1-x}B'_xX_3$ mit dieser Struktur auftreten, weiter A-Kationenlücken □ wie in $□_{1-x}A_xBX_3$ und geordnete Kationen wie in $A_2BB'X_6$. Über Perowskite mit Anionenlücken ist schon häufig berichtet worden, vermutlich sind die Anionenleerstellen ⊕ nicht willkürlich verteilt. In Verbindungen, die Fe^{3+}-Ionen enthalten, scheinen sie z. B. paarweise im Oktaeder eines einzelnen *B*-Platzes zusammenzutreffen und die

*) This work was sponsered by the U. S. Air Force.

compounds containing Ti^{4+} ions, on the other hand, it is more probable that local rearrangements of the anions form trigonal bipyramidal sites. Anion-deficient, ionic materials in which there are no A-cations, such as $\square WO_{3-x}$, have been shown to contain $\square BX_3$ blocks connected by "shear" planes across which the occupied octahedra share common edges (Fig. 22). On the other hand, anion deficiencies may occur randomly in the $M^cX_{1-x}M^f_3$ alloys. B-cation defects cannot occur, because the B-occupied octahedra form the basis of the ABX_3-perovskite structure. Where there are apparent B-cation vacancies, as in $A_mB_{m-1}X_{3m}$, there is either an interleaving of perovskite layers with A_2X_2 layers (Fig. 23) or an interleaving of cubic (perovskite) stacking of AO_3 layers with regularly spaced hexagonal stackings at which are located the B-ion vacancies (Fig. 24). Similarly, the series of compounds $(AX)_m(ABX_3)_n$ crystallize with an interleaving of rocksalt layers (Fig. 25). Interleaving of cubic-stacked AO_3 layers and hexagonal-stacked layers also occurs in ABX_3 compounds having too large an A cation to be accommodated by the perovskite structure (Fig. 3). Finally, there are a few alloys with interesting magnetic properties that can be classified as $A_2BB'X_6$ compounds if the symbols B and B' are allowed to represent atomic clusters rather than single cations. These are illustrated, for example, by the alloy $Al_2(AlCo_{12})(Co_8)B_6$ (Fig. 18). Sections 3.1 and 3.2 are devoted to descriptions of the perovskite and perovskite-related structures.

The ABX_3 perovskites exhibit several interesting physical properties such as ferroelectricity (as in $BaTiO_3$), ferromagnetism (as in $SrRuO_3$), weak ferromagnetism (as in $LaFeO_3$ or $HoFeO_3$), superconductivity (as in $SrTiO_{3-x}$), a large thermal conductivity due to exciton transport ($LaCoO_3$), insulator-to-metallic transitions of interest for thermistor applications (as in $LaCoO_3$), fluorescence compatible with laser action (as in $LaAlO_3$:Nd), and transport properties of interest for high-temperature thermoelectric power (as in La_2CuO_4). A few ABX_3 perovskites have been found that are simultaneously antiferromagnetic and ferroelectric [*Sm16, Mi7, Sm9*]. The simultaneous occurrence of ferroelectricity and ferromagnetism has been reported for systems like $Sr_{0.25}La_{0.75}MnO_3$-$ATiO_3$ (A = Ba, Pb, $Bi_{0.5}K_{0.5}$) [*To3, To6*]. Many of the $M^cXM^f_3$ perovskite alloys are ferromagnetic or ferrimagnetic, and a few exhibit first-order ferrimagnetic-to-ferromagnetic transitions. Nevertheless, the significance of the entire perovskite family for the field of magnetism*) lies not yet in their technological applications, but in their provision of an isostructural series of compounds having outer *d* electrons that are localized and spontaneously magnetic in

*) The technologically important dielectric properties are outside the scope of this summary. See Vol. III/3 of the New Series of Landolt-Börnstein.

dortige Anionenlücke von einem Oktaeder in einen Tetraeder umzuwandeln. Bei Verbindungen, die Ti^{4+}-Ionen enthalten, ist es dagegen wahrscheinlicher, daß die lokale Anordnung der Anionen trigonale Doppelpyramiden-Plätze bildet. Für Ionenverbindungen mit Anionenlücken, die keine A-Kationen haben, wie $\square WO_{3-x}$, ist gezeigt worden, daß sie $\square BX_3$-Blöcke enthalten, die durch „Gleit"-ebenen verbunden sind, in denen die besetzten Oktaeder gemeinsame Kanten innehaben (Fig. 22). In $M^cX_{1-x}M^f_3$-Legierungen können jedoch Anionenlücken auch beliebig auftreten. B-Kationenlücken können nicht vorkommen, weil die von B besetzten Oktaeder die Basis der ABX_3-Perowskitstruktur bilden. Wo scheinbare B-Kationenleerstellen auftreten, wie in $A_mB_{m-1}X_{3m}$, sind entweder A_2X_2-Schichten zwischen Perowskitschichten eingeschoben (Fig. 23), oder kubische (Perowskit-) Anordnungen von AO_3-Schichten wechseln mit regelmäßig verteilten hexagonalen Anordnungen, in denen die B-Ionenlücken auftreten, ab (Fig. 24). Ähnlich kristallisieren die Verbindungen der Reihe $(AX)_m(ABX_3)_n$ mit einer Einschiebung von Steinsalzschichten (Fig. 25). Einschiebungen von kubisch gepackten AO_3-Schichten und hexagonal gepackten Schichten treten auch in solchen ABX_3-Verbindungen auf, deren A-Kation für die Perowskit-Struktur zu groß ist (Fig. 3). Schließlich gibt es einige wenige Legierungen mit interessanten magnetischen Eigenschaften, die als $A_2BB'X_6$-Verbindungen eingeordnet werden können, wenn man unter den Symbolen B und B' Atomgruppen statt einzelner Kationen versteht, Dies gilt z. B. für die Legierung $Al_2(AlCo_{12})(Co_8)B_6$ (Fig. 18). Die Abschnitte 3.1 und 3.2 sind der Beschreibung der Perowskit- und verwandter Strukturen gewidmet.

Die ABX_3-Perowskite weisen einige interessante physikalische Eigenschaften auf, wie Ferroelektrizität (in $BaTiO_3$), Ferromagnetismus (in $SrRuO_3$), schwachen Ferromagnetismus (in $LaFeO_3$ oder $HoFeO_3$), Supraleitfähigkeit (in $SrTiO_{3-x}$), große Wärmeleitfähigkeit durch Excitonentransport (in $LaCoO_3$), für Thermistoren interessante Übergänge zwischen Nichtleiter und metallischem Leiter (in $LaCoO_3$), für Laser-Anwendungen geeignete Fluoreszenz (in $LaAlO_3$:Nd), und Transporteigenschaften, die für Thermospannungen bei hohen Temperaturen von Interesse sind (in La_2CuO_4). Einige wenige ABX_3-Perowskite wurden gefunden, die sowohl ferromagnetisch als auch ferroelektrisch sind [*Sm16, Mi7, Sm9*]. Das gleichzeitige Auftreten von Ferroelektrizität und Ferromagnetismus wurde bei Systemen wie $Sr_{0.25}La_{0.75}MnO_3$-$ATiO_3$ (A = Ba, Pb, $Bi_{0.5}K_{0.5}$) [*To3, To6*] beschrieben. Viele $M^cXM^f_3$-Perowskitlegierungen sind ferromagnetisch oder ferrimagnetisch, und einige zeigen Übergänge erster Ordnung von Ferri- zu Ferromagnetismus. Trotzdem liegt die Bedeutung der gesamten Perowskit-Familie für den Magnetismus*) noch nicht in der technologischen Anwendung, sondern im Vorhandensein einer isostrukturellen Reihe von Verbin-

*) Die technologisch wichtigen dielektrischen Eigenschaften liegen nicht im Rahmen dieser Zusammenstellung. Siehe Band III/3 der Neuen Serie des Landolt-Börnstein.

one member, collective and spontaneously magnetic in another, and collective and Pauli paramagnetic in yet another. This permits a systematic experimental investigation of the properties of the *d* electrons on passing through the transition from a localized character, where crystal-field plus superexchange and/or double-exchange theories apply, to an uncorrelated (except below a superconducting transition temperature) collective-electron character, where the conventional band theory applies. In addition, the simplicity of the perovskite ABX_3 structure minimizes competitive magnetic interactions between neighboring magnetic cations. Therefore from a study of magnetic order, as revealed by neutron diffraction, together with detailed structural information, as revealed by x-ray diffraction, it has been possible to test the semiempirical rules for 180° cation-anion-cation isotropic superexchange interactions between localized electrons, the double-exchange hypothesis, antisymmetric exchange, and predictions of magnetic order and spontaneous atomic moments due to collective electrons.

Section 3.3 presents the general phenomenological exchange Hamiltonian for localized electrons and summarizes the microscopic models for isotropic superexchange, double exchange, and antisymmetric exchange. From these models, general rules for the interactions responsible for magnetic order are developed for comparison with the tabulated magnetic data.

Section 3.4 presents the fundamental physical concepts needed to construct a qualitative phase diagram for the outer *d* electrons as a function of the number n_l of electrons per relevant orbital, the magnitude of a nearest-neighbor transfer energy *b*, and the temperature *T*. It also summarizes the various characters of several physical properties imparted by outer electrons to show how they can be used to distinguish the electronic phases in different perovskites. Information from the tabulated data is used to show the influence of covalence and intra-atomic exchange, which help determine the parameter *b*, on the character of the electrons. Spontaneous collective-electron magnetism is seen to occur only in a narrow transitional interval of *b* between localized-electron magnetism and collective-electron Pauli paramagnetism.

Section 3.5 provides schematic energy diagrams for the alloys $M^cXM_3^f$. These are shown to be useful guides to predictions of the magnitudes of the atomic moments and the magnetic order.

dungen mit äußeren *d*-Elektronen, die lokalisiert und spontan magnetisch in der einen Verbindung, kollektiv und spontan magnetisch in einer anderen, und kollektiv und Pauli-paramagnetisch in noch einer weiteren sind. Dies erlaubt systematische experimentelle Untersuchungen der Eigenschaften der *d*-Elektronen, indem man von einem lokalisierten Zustand, in dem Kristallfeld plus Superaustausch- und/oder Doppelaustausch-Theorien gelten, zu einem Zustand unkorrelierter Kollektivelektronen (außer bei Temperaturen unterhalb des Übergangs zur Supraleitung) übergeht, in dem die konventionelle Bändertheorie anzuwenden ist. Weiterhin führt die Einfachheit der Perowskit-ABX_3-Struktur zu minimalen konkurrierenden Wechselwirkungen zwischen benachbarten magnetischen Kationen. Aufgrund der Untersuchung der magnetischen Ordnung, die man durch die Neutronenbeugung kennt, und einer genauen Kenntnis der Struktur, wie man sie durch Röntgenbeugung gewonnen hat, war es deshalb möglich, die halbempirischen Gesetze über die isotrope 180°-Kation-Anion—Kation—Superaustausch—Wechselwirkung zwischen lokalisierten Elektronen, die Doppelaustausch-Hypothese, den antisymmetrischen Austausch und Voraussagen für magnetische Ordnung und spontane Atom-Momente, die von Kollektivelektronen herrühren, zu prüfen.

Der Abschnitt 3.3 enthält den allgemeinen phänomenologischen Hamilton–Austausch–Operator für lokalisierte Elektronen und faßt die mikroskopischen Modelle für den isotropen Superaustausch, den Doppelaustausch und den antisymmetrischen Austausch zusammen. Aus diesen Modellen werden allgemeine Regeln für die Wechselwirkungen, die für die magnetische Ordnung verantwortlich sind, zum Vergleich mit den tabellierten Daten entwickelt.

Der Abschnitt 3.4 enthält die grundlegenden physikalischen Ideen, die für die Herstellung eines qualitativen Phasendiagramms für die äußeren *d*-Elektronen als Funktion der Elektronenzahl n_l pro betreffenden Bahnzustand, der Größe einer Übertragungsenergie *b* zwischen nächsten Nachbarn und der Temperatur *T* notwendig sind. Außerdem werden hier verschiedene Charakteristika einiger durch die äußeren Elektronen gegebenen physikalischen Eigenschaften zusammengestellt, um zu zeigen, wie man mit ihrer Hilfe die elektronischen Phasen verschiedener Perowskite unterscheiden kann. Auf Grund der tabellierten Werte wird der Einfluß von Kovalenz und intra-atomarem Austausch, die den Parameter *b* mitbestimmen, auf den Charakter der Elektronen gezeigt. Spontane Magnetisierung der Kollektivelektronen tritt, wie man sieht, nur in einem schmalen Übergangsintervall von *b* zwischen dem Magnetismus lokalisierter Elektronen und dem Pauli-Paramagnetismus der Kollektivelektronen auf.

Der Abschnitt 3.5 enthält schematische Energiediagramme für die Legierungen $M^cXM_3^f$. Es wird gezeigt, daß sie zu brauchbaren Voraussagen über die Größe der Atom-Momente und die magnetische Ordnung führen können.

In the introductions to the sections 3.2 ··· 3.5 we have referenced the principle theoretical contribution discussed, but no attempt was made to do this systematically for the experimental contributions, which are thoroughly referenced in the tables. — In the crystallographic tables, the crystal parameters quoted either represent the most complete analysis, in our judgment, or belong to the most complete set of parameters for a series of similar compounds. They do not necessarily represent the historical reference that established the unit-cell dimensions.

Literature was considered up to 1969.

Finally, we would like to thank DAVID MAHONEY for his willing assistance, the library and publications personnel of Lincoln Laboratory for their efficient support, and Mrs. G. E. BOYD for her help with all the foreign references.

In den Einleitungen zu den Abschnitten 3.2 ··· 3.5 haben wir die grundlegenden theoretischen Beiträge, die diskutiert werden, mit Literaturhinweisen versehen; für die experimentellen Beiträge haben wir dies nicht systematisch durchzuführen versucht, da die entsprechenden Tabellen vollständig mit Literaturhinweisen versehen sind. — In den kristallographischen Tabellen stellen die angeführten Kristallparameter entweder die nach unserer Beurteilung vollständigste Analyse dar, oder sie gehören zum vollständigsten Satz von Parametern für eine Reihe ähnlicher Verbindungen. Sie geben nicht notwendigerweise den historischen Literaturhinweis, der die Dimensionen der Einheitszelle festlegte.

Die Literatur wurde bis 1969 berücksichtigt.

Schließlich möchten wir DAVID MAHONEY für seine bereitwillige Hilfe, den Angestellten der Bibliothek und der Veröffentlichungsabteilung des Lincoln-Laboratoriums für ihre wirksame Unterstützung und Mrs. G. E. BOYD für ihre Hilfe bei der ausländischen Literatur danken.

3.0.2 Symbols and units used in tables and figures

Crystallographic structure

symmetry	symmetry classification for perovskite structures: C = cubic, H = hexagonal, R = rhombohedral, O = orthorhombic ($a < c/\sqrt{2}$), O' = orthorhombic ($c/\sqrt{2} < a$), T = tetragonal, M = monoclinic, Tr = triclinic
a, b, c [Å]	lattice parameters
α, β, γ [deg]	angle between crystallographic axes
$\Theta_{trans}, \Theta_{ord}$ [°K]	crystallographic transition and ordering temperatures
Θ_D [°K]	Debye temperature
T_{melt} [°K]	melting temperature
c_{ij}	elastic constants
ε_i	crystalline strains
$r_{A,B,B'}$ [Å]	radius of A, B, B' cation

Magnetic properties (static measurements)

magnetic order	see magnetic structure type from Fig. 26
$n_A, n_{\|}^A$	atomic moment and component of atomic moment parallel to net ferromagnetic moment in numbers of Bohr magnetons: $p_A = n_A \mu_B$
$\overline{n}_m$	net magnetization per molecule in numbers of Bohr magneton: $p_m = \overline{n}_m \mu_B$
n_{eff}	$n_{eff} = \sqrt{8C_m}$ is the effective paramagnetic moment: $p_{eff} = n_{eff} \mu_B$
Θ_C [°K]	Curie temperature
Θ_N [°K]	Néel temperature; extrapolated Néel temperature
Θ_r [°K]	temperature for spin reorientation
Θ_p [°K]	paramagnetic Curie temperature ($\Theta_p < 0$ if antiferromagnetic coupling)
Θ' [°K]	temperature below which parasitic $n_{\|}^A$ deviates appreciably from 0.05
C_m [emu °K mole^{-1}]	molar Curie constant determined from Curie-Weiss law $\chi_m = C_m/(T - \Theta_p)$
χ_g [emu/g], [cm^3/g]	specific paramagnetic susceptibility
χ_m [emu/mole]	molar paramagnetic susceptibility
p_A, p^A [μ_B]	atomic moment, atomic moment of element A
$p_m, p^{(xy)}$	molecular moment (of molecule xy)
p^*	effective paramagnetic moment: $p^* = \sqrt{\chi_m T}$
J_{nn}/k [°K]	isotropic exchange constant of Eq. (16) for near-neighbor interactions
d	Ln-Fe interaction parameter defined by $M(t) = \sigma_0(0)\, B(t)\, [1 + (d/t)]$, where $t = T/\Theta_C$ and $B(t)$ is the Brillouin function
σ_w [erg/cm^2]	domain wall energy density
W_{nn}	net near-neighbor Weiss molecular field constant: $H_{wi} = \sum_{j=1}^{z} W_{ij} M_j$

σ [Gauss cm³/g] / [emu/g]	magnetic moment per gram = specific magnetization
σ_o [emu/g]	specific parasitic (weak) magnetization as obtained from $\sigma = \sigma_o + \chi_g H_a$
σ_{sp}	spontaneous specific magnetization
H_a [Oe]	externally applied field
H_{crit} [Oe]	critical applied field for antiferromagnetic-ferromagnetic transition or for spin-flop transition
H_c	coercivity
α	cant angle
b_1, b_2 [dyn/cm²]	magnetoelectric coefficients
λ_{100}	magnetostriction constant for [100] direction: $\lambda_{100} = -4b_1/3(c_{11} - c_{12})$
C_{ijk}	components of the tensor describing the quadratic dependence of magnetization on applied field: Eq. (36)
μ_B	the Bohr magneton = 5585 emu/g
T [erg/g]	torque: $T = \sigma \times H_a$

Magnetic properties (resonance measurements)

H_A	effective crystalline-anisotropy field
H_{ex}	exchange field
H_D	spin-canting field (Dzialoshinskii field)
H_{int}	internal magnetic field at the nucleus
H_n	axial hyperfine field arising from nuclear polarization
H_{hyp}	hyperfine field $\boldsymbol{I}\cdot\mathbf{A}\cdot\boldsymbol{S}$, where $\boldsymbol{I}$ = nuclear spin, $\boldsymbol{S}$ = net atomic spin, and the components of the interaction tensor are A_s, A_{ns}, A_σ, A_π, A_{2p}.
$f_s^A, f_\sigma^A, f_\pi^A$	fraction of unpaired s, p_σ or p_π electron spins involved in covalent bonding: $f_s^A = 2SA_s/A_{ns} = \frac{1}{3}N_e^2\lambda_s^2$, $f_\sigma^A = 2SA_\sigma/A_{2p} = \frac{1}{3}N_e^2\lambda_\sigma^2$, $f_\pi^A = 2SA_\pi/A_{2p} = \frac{1}{4}N_t^2\lambda_\pi^2$. See Eq. (4) for N_e, N_t, λ_s, λ_σ, λ_π.
ε, ΔE	nuclear quadrupole coupling constant and quadrupole splitting
F_{ij}, G_{ij}	dipolar and quadrupolar magnetoelastic coefficients: $\delta g_i = \sum_{j=1}^{6} F_{ij}\varepsilon_j$ and $d_i = \sum_{j=1}^{6} G_{ij}\varepsilon_j$, where $\mathscr{H}_{\text{spin-lattice}} = \mu_B \boldsymbol{H}_a \cdot \delta\mathbf{g}\cdot\boldsymbol{S} + \boldsymbol{S}\cdot\mathbf{d}\cdot\boldsymbol{S}$
ν_R [Hz]	resonance frequency for NMR
$\Delta\nu$ [Hz]	half-line width
T_1 [sec]	nuclear spin-lattice relaxation time
T_2 [sec]	nuclear spin-spin relaxation time
T_{1e} [sec]	nuclear spin-lattice relaxation time during a locking pulse

Optical measurements

n	index of refraction
ε_o	low-frequency dielectric constant
ϱ [°/cm]	Faraday rotation
ν_{TO}, ν_{LO} [Hz]	frequency of transverse and longitudinal optical modes

Transport measurements

Θ_{cs}	superconducting critical temperature
E_F	Fermi energy
E_a	activation energy for a small-polaron hop
ϱ [Ωcm]	electrical resistivity
S [μV/°K]	Seebeck coefficient
e [esu]	magnitude of the electronic charge
c, n_i, $n_\pm$ [cm⁻³]	charge-carrier density
μ [cm²/Vsec]	charge-carrier mobility
τ [sec]	charge-carrier collision time
m^* [g]	charge-carrier effective mass
D_0 [cm²/sec]	charge-carrier diffusion coefficient at $E_a = 0$
$N_\pm$	density of unoccupied states: $2(2\pi m_\pm^* kT/h^2)^{3/2}$

General properties

T [°K]	temperature
p	pressure
c_p	specific heat at constant pressure

Abbreviations for text and indices

AFMR	antiferromagnetic resonance
APR	acoustic paramagnetic resonance
BPW	Bethe-Peierls-Weiss method
C, cub	cubic
DS	Danielson-Stevens method
DTA	differential thermal analysis
ESR	electron spin resonance = paramagnetic resonance
f.c.	face-centered permutation
FMR	ferromagnetic resonance
F_R	ferromagnetic with reduced n_A
H, hex, hex (nL)	hexagonal, hexagonal n-layer structure
I.R.	infrared
Ln	Lanthanon = any of the rare-earth elements
MF	molecular field approximation
M, mon	monoclinic
NAR	nuclear acoustic resonance
NMR	nuclear magnetic resonance
ncub	noncubic
O, O', orth	orthorhombic (O: $a < c/\sqrt{2}$; O': $c/\sqrt{2} < a$)
P&S	reference to preparation and structural information
Prep.	reference to material preparation
Prop.	reference to material properties
pscub	pseudocubic
psmon	pseudomonoclinic
R, rh	rhombohedral
RW	Rushbrooke-Wood method
S. G.	space group
S.S.	solid solution
T, tetr	tetragonal
Tr, tr	triclinic

3.1 Descriptions of stoichiometric ABX_3 and $M^cXM^f_3$ structures

3.1.1 The ideal perovskite structure

The ideal perovskite structure has the cubic unit cell of Fig. 1 with space group Pm3m. Fig. 1 (a) shows the corner-sharing octahedral units (BX_3 array in ABX_3 and XM^f_3 array in $M^cXM^f_3$), which form the stable skeleton of the structure. The A cation (or M^c atom) occupies the body-center position. Fig. 1 (b) shows the unit cell with the A cation (or M^c atom) at the origin, or corner position. This shows the face-centered-cubic character (with Cu_3Au-type order) of the AX_3 or $M^cM^f_3$ subarrays. Fig. 1 (c) shows the cubic perovskite on an hexagonal basis, with the c axis along the cubic [111] direction. The alternate AX_3 and B ionic layers each have cubic stacking. Also indicated is the ordering of B and B' layers in the ordered $A(B'_{2/3}B_{1/3})X_3$ structures.

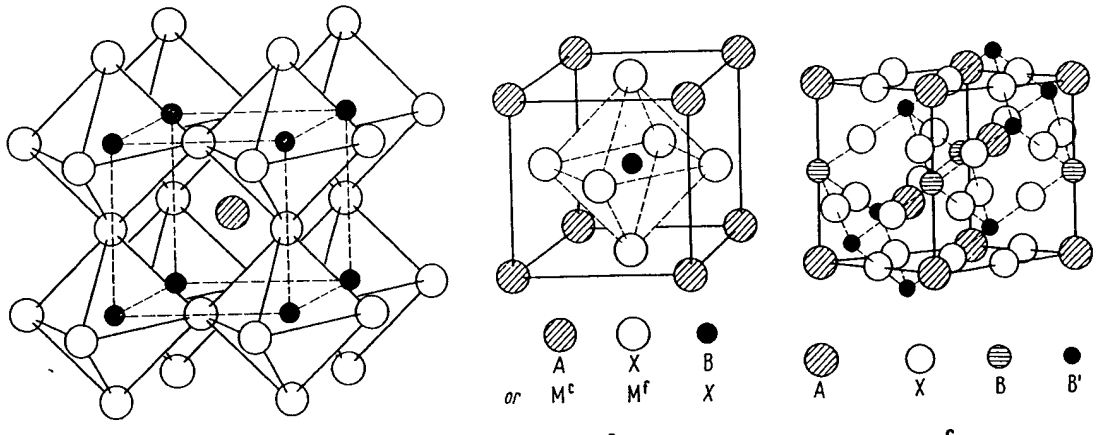

Fig. 1. ABX_3, $M^cXM^f_3$. Ideal perovskite structure: a) B cation (or X atom) at origin. b) M^c atom (or A cation) at origin. c) A cation at origin in hexagonal basis [*Ga10*].

The alloys $M^cXM_3^f$ are stabilized by covalent M-X bonding and by metallic M-M bonding, so that they are generally cubic. Only in phases exhibiting complex magnetic order are there distortions to lower symmetry. On the other hand, the ABX_3 perovskites, which are primarily stabilized by the Madelung energy, are rarely cubic at normal temperatures. Madelung energy calculations are available [*Ro15a, Sa2b, Mi1*].

Although cubic at high temperatures, most ABX_3 compounds exhibit distortions to lower symmetry below some temperature Θ_{trans} as a result of atomic displacements. Such displacive transitions can be described by a finite set of normal vibrational modes that become soft, their vibrational frequency increasing with $T > \Theta_{trans}$. From LANDAU's [*La2*] theory of phase transitions, it may be argued [*Ha1, Co2*] that at a second-order displacive transition, the frequency of one normal mode becomes zero. Thus the occurrence of ferroelectricity in perovskite-type crystals such as **$BaTiO_3$** has been correlated both theoretically and experimentally [*An2, Co1, Ba17, Co28, Ne8, Sh26*] with the existence of a transverse optic mode of lattice vibration having wave number $k \approx 0$ and a temperature-dependent frequency $\omega \sim (T - \Theta_{trans})^{1/2}$.

Similarly, in the case of **$LaAlO_3$** softening of a single normal mode can produce the $R\bar{3}c$-to-cubic transition, and this transition is probably second-order. Investigation [*Ha1*] of the atomic displacements involved in other distortions from cubic symmetry, on the other hand, has shown that several normal modes are involved, and these displacive transitions are first-order.

$SrTiO_3$ exhibits a tetragonal (D_{4h}^{18} with $c/a = 1.00056$) to cubic transition at $\Theta_{trans} = 110$ °K [*Ly2, Ri5*] that appears to illustrate the softening of a triply degenerate phonon at the R point of the Brillouin zone in the cubic phase. For $T < \Theta_{trans}$, it splits into two zone-center phonons having a frequency dependence $\omega \sim (\Theta_{trans} - T)^{0.31}$ [*Fl2*]. In the presence of an external electric field E_a the symmetry is further reduced to C_{4v} if $E_a \parallel c$-axis, or C_{2v} if $E_a \perp c$-axis, and the critical modes have the same symmetry as the ferroelectric TO modes. "Anticrossing" of the modes occurs for $E_a = 1.5$ kV/cm and 15 kV/cm [*Ne7, Wo19*]. Thus the observed [*He5*] maximum in the electric susceptibility of **$SrTiO_3$** at very low temperatures does not appear to be associated with a ferroelectric transition.

Theoretical interest in the analytic description of these phase transitions continues [*Go1a, Mu4a, Ta14a, Th3*].

The physical origins of the various crystallographic distortions may be separated into three parts: relative ionic sizes, electron ordering among localized electrons, and electron ordering among collective electrons.

3.1.2 The influence of relative ionic sizes

3.1.2.1 Tolerance factor

The first prerequisite for a stable perovskite structure is the existence of a stable BX_3 skeletal subarray. If the B-cation radius is $r_B < 0.51$ Å in oxides, for example, the B cation does not achieve its optimum B-O separation in an octahedral site and therefore stabilizes a structure with a smaller anion coordination. The Al^{3+} ion is borderline, being stable in four, five or six coordination. However, Ga^{3+}, Ge^{4+} and V^{5+} ions are definitely more stable in tetrahedral sites at ambient pressures.

Given the BX_3 skeletal subarray, additional stabilization is achieved by accommodating a large A cation within this skeleton. Because there is an optimum A-X bond length, the presence of an A atom generally distorts the BX_3 array so as to optimize the A-X bonding. However, if this distortion is too large, then other space groups become competitive. GOLDSCHMIDT [*Go2*] defined the tolerable limits on the size of the A cation via a tolerance factor

$$t = (r_A + r_X)/\sqrt{2}\,(r_B + r_X) \qquad (1)$$

where r_A, r_B, r_X are empirical radii of the respective ions. By geometry, the ideal cubic structure should have $t = 1$. The perovskite structure occurs only within the range $0.75 < t < 1.00$. However, this is not a sufficient condition, since the A and B cations must, in themselves, be stable in twelvefold (12 or 8 + 4 or 6 + 6) and sixfold coordinations. This sets lower bounds for the cationic radii. In oxides these bounds are $r_A > 0.90$ Å and $r_B > 0.51$ Å. In addition, MEGAW [*Me5*] noted that, if $0.75 < t < 0.9$, a cooperative buckling of the corner-shared octahedra to optimize the A-X bond lengths enlarges the unit cell; on the other hand, if $0.9 < t < 1$, such buckling may not be found, although small distortions to rhombohedral symmetry occur. These structures are to be distinguished from perovskites that exhibit additional distortions as a result of electron ordering. The cubic phase is found at high temperatures or where the A-X bond is more ionic (especially if $t \approx 1$).

Where the A cation is too small ($r_A < 0.9$ Å) to accommodate twelve nearest neighbors, a structure in which the A and B cations are both six-coordinated becomes competitive. From the phase diagram of Fig. 2 for the oxides $A^{3+}B^{3+}O_3$, which has been adapted from SCHNEIDER, ROTH, and WARING [*Sc13*], the initial competition is the C-M_2O_3 structure, which contains two unusual types of corner-shared, six-coordinated sites. The C-M_2O_3 structure consists of a face-centered-cubic array of cations with anions occupying $\frac{3}{4}$ of the tetrahedral interstices in an ordered manner. Thus each cation has six out of eight near-neighbor anions at the corners of a circumscribing cube: $\frac{1}{4}$ of the cations have two anions missing at the ends of a body diagonal and $\frac{3}{4}$ of the cations have two anions missing at the end of a face diagonal of the circumscribing cube. This arrangement minimizes the electrostatic repulsive forces between the cations.

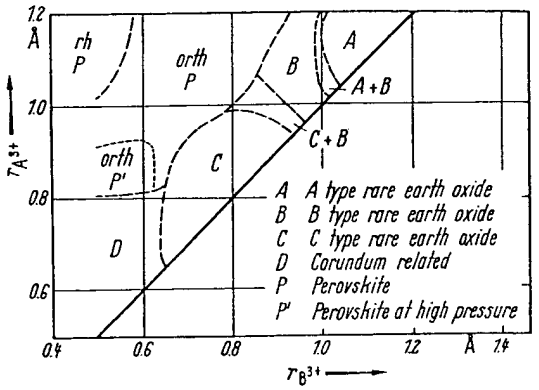

Fig. 2. General $r_A - r_B$ phase diagram for $A^{3+}B^{3+}O_3$ compounds based on ionic-size considerations. Exceptions may occur where considerations other than ionic radii r_A, r_B become important, as in the case A = Bi. A similar plot for $A^{2+}B^{4+}O_3$ perovskites is not useful because secondary considerations are amplified by ferroelectric distortions and the possibility of different layer sequences where larger A cations are present. [Adapted from *Sc13*].

Given smaller A cations, however, electrostatic screening between face-shared octahedra can be achieved by displacements of the cations away from the shared face, and the structure competitive with perovskite is generally built from an hexagonal-close-packed anion array, which has octahedral holes sharing common faces along the *c*-axis. With one octahedral hole per anion and a cation/anion ratio 2/3, the cations are ordered among these holes so as to minimize the electrostatic energy. If the A and B cations carry the same charge, as in $A^{3+}B^{3+}O_3$, only pairs of cations share common octahedral-site faces and there is no ordering of A and B within the cationic array. This allows the electrostatic force between two cations sharing a common octahedral face to be reduced by displacements of the cations away from each other, thus distorting the octahedra. The result is the corundum structure of $\mathbf{Al_2O_3}$. If the cations A and B carry different charges, as in $A^{2+}B^{4+}O_3$, then the A and the B cations order into alternate puckered cationic (111) planes of the rhombohedral corundum structure to form the ilmenite structure. However, where there is a large difference in the cationic charges, as in $\mathbf{Li^+Sb^{5+}O_3}$ and $\mathbf{Li^+Nb^{5+}O_3}$, two other alternatives become competitive: (1) The A^+ ions order in strings of face-shared octahedra so as to permit the B^{5+}-ion octahedra to share only edges with near-neighbor occupied octahedra. This structure is illustrated by $\mathbf{LiSbO_3}$ [*Ed1*]. (2) After ordering B^{5+} and Li^+ ions whithin each cationic (111) plane of the corundum structure in such a way that B^{5+} and Li^+ ions share common octahedral-site faces, each A^+ cation is then displaced into the far face of its octahedron, where it is equally spaced from B^{5+} cations above and below so long as the B^{5+} cations remain in the centers of their octahedra. This is the structure of paraelectric $\mathbf{LiNbO_3}$ and $\mathbf{LiTaO_3}$ [*Ab3*].

Where the A cation is too large ($t > 1.0$), the close-packed AX_3 layers of Fig. 1(c) tend to change their stacking sequence from cubic to hexagonal. However, the change from the all-cubic stacking of the rhombohedral perovskite structure to the all-hexagonal stacking of the hexagonal (hex. 2L) $\mathbf{CsNiCl_3}$ structure goes via the three intermediate steps shown in Fig. 3 [*Lo1*]. The first step is the hexagonal $\mathbf{BaTiO_3}$ structure of Fig. 3(c). It is a six-layer structure with stacking sequence *a-b-c-a-c-b-a*, corresponding to one hexagonal stacking out of three. In this structure (hex. 6L), two-out-of-three B cations form pairs sharing a common octahedral-site face, and one-out-of-three B cation shares only common octahedral-site corners as in the perovskite structure. Many ordered compounds $A_3B_2B'O_9$ are known to have this structure. The second step, illustrated by the hexagonal $\mathbf{BaMnO_3}$ structure of Fig. 3(d), alternates hexagonal and cubic stackings with the sequence *a-b-c-b-a*. This four-layer structure (hex. 4L), contains only B-cation pairs sharing common octahedral-site faces. The electrostatic forces between paired B-cations in Figs. 3(c), (d) displace the paired cations from one another along the *c* axis, exactly as in the corundum

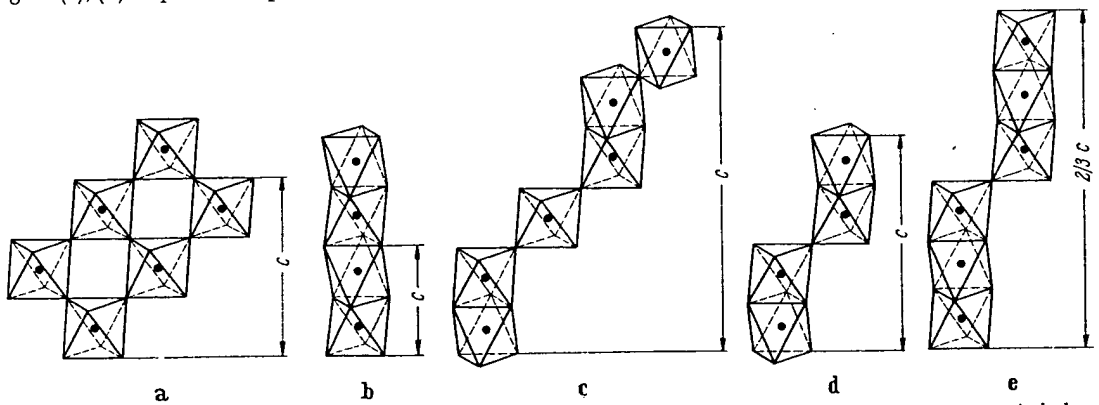

Fig. 3. Stable structures intermediate to a) cubic perovskite and b) the two-layer hexagonal $CsNiCl_3$ structure, c) six-layer hexagonal $BaTiO_3$ structure, d) four-layer hexagonal $BaMnO_3$ structure, e) nine-layer hexagonal $BaRuO_3$ structure. [Adapted from *Ca2*].

structure. The third step is the nine-layer (hex. 9L) structure of **$BaRuO_3$**, which has two hexagonal stackings out of three in the sequence *a-b-c-b-c-a-c-a-b-a*. Here the B cations form strings of three sharing common octahedral-site faces along the *c*-axis. Electrostatic forces displace the two end-member B cations away from the center B cation of each string, as shown in Fig. 3(e). Because cubic stacking is stabilized by hydrostatic pressure, it is possible to convert under pressure and high temperature the hexagonal structures to the perovskite structure through the successive sequence of steps. This is well illustrated by the **$Ba_{1-x}Sr_xRuO_3$** system as shown in Fig. 4(a). These particular intermediate structures appear to be stabilized by the cation displacements, but at the cost of alternating the stacking sequence. The (hex. 4L) structure, which has the maximum alternation of stacking, is not always found, and the intermediate structures tend to be stabilized by smaller B cations, as illustrated in Fig. 4(b).

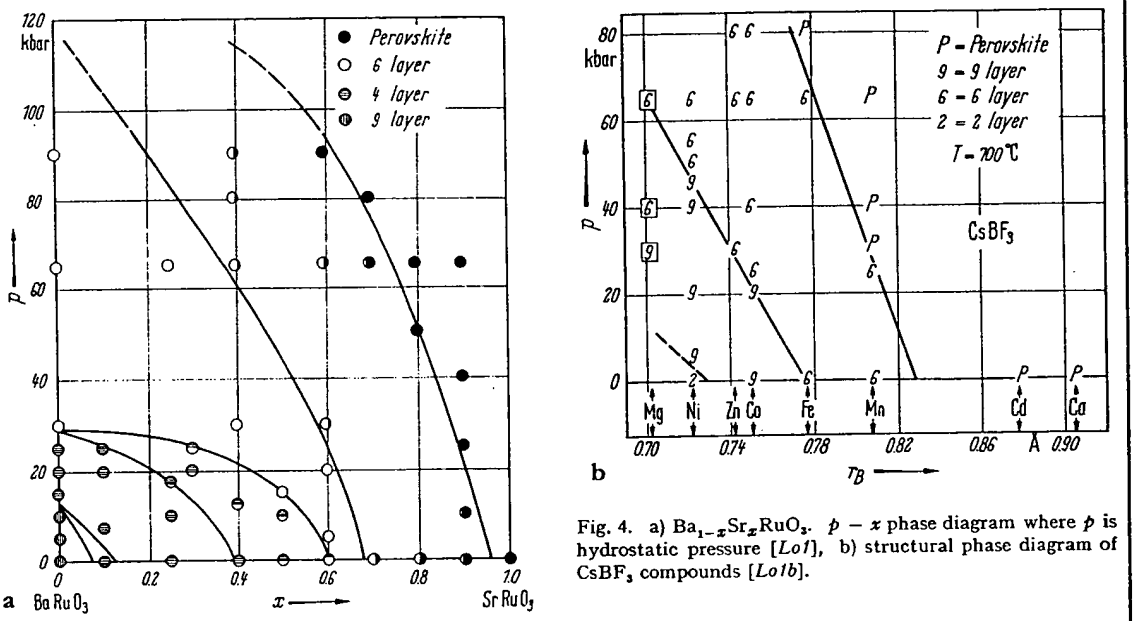

Fig. 4. a) $Ba_{1-x}Sr_xRuO_3$. $p - x$ phase diagram where p is hydrostatic pressure [*Lo1*], b) structural phase diagram of $CsBF_3$ compounds [*Lo1b*].

3.1.2.2 O-orthorhombic structure

Cooperative buckling of corner-shared octahedra, although indexed on a monoclinic pseudocell in earlier work, may produce the orthorhombic primitive cell of Fig. 5 containing four formula units. It was first identified in single crystals of **$GdFeO_3$** [*Ge1*] and later confirmed [*Co21*]. Powder photographs taken with CrK_α radiation could be indexed on the monoclinic pseudocell containing a single **$GdFeO_3$** molecule, which is the origin of the earlier classification. The pseudocell dimensions of **$GdFeO_3$** are $a = c = 3.87$ Å, $b = 3.83$ Å, $\beta = 92.8°$, where $2b_{\text{pseudocell}} = c_{\text{true cell}}$. The true orthorhombic cell is referred to in the tables as O-orthorhombic and is distinguished from the O'-orthorhombic structure by a lattice-parameter ratio

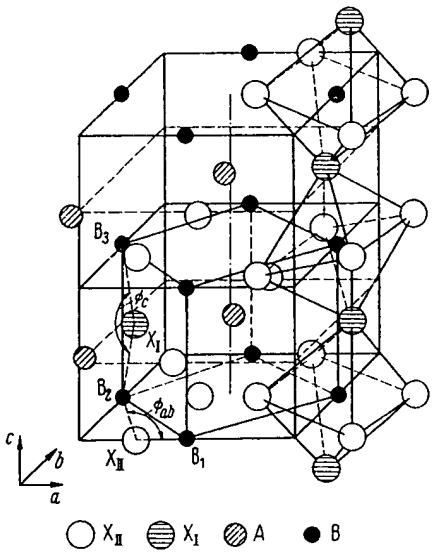

Fig. 5. $GdFeO_3$. O-orthorhombic structure.
$\phi_{ab} = \sphericalangle B_1X_{II}B_2$, $\phi_c = \sphericalangle B_2X_IB_3$.
Fig. from [*Ve12*], structure [*Ge1*], coordinates[*Co21*].

ion	position	coordinates		
		x	y	z
Gd^{3+}	4(c)	−0.018	0.060	¼
Fe^{3+}	4(b)	½	0	0
O_I^{2-}	4(c)	0.05	0.470	¼
O_{II}^{2-}	8(d)	−0.29	0.275	0.05

$c/a > \sqrt{2}$, where $a < b$. The O'-orthorhombic structure, which has $c/a < \sqrt{2}$, is the result of a superposed Jahn-Teller (with or without spin-orbit coupling) distortion. It is also to be distinguished from ferroelectric O_B^*-orthorhombic and O_B^F-orthorhombic distortions in which each B cation is removed from the center of symmetry of its interstice. Other orthorhombic distortions have been reported for **$NdGaO_3$** [*Br26*] and **$NaCoF_3$** [*Ok5*].

The O-orthorhombic unit cell has the probable space group Pbnm with A cations in positions 4(c): $\pm(x, y, \frac{1}{4}; \frac{1}{2} - x, \frac{1}{2} + y, \frac{1}{4})$, the B cations in 4(b): $(\frac{1}{2}, 0, 0; \frac{1}{2}, 0, \frac{1}{2}; 0, \frac{1}{2}, 0; 0, \frac{1}{2}, \frac{1}{2})$, eight anions X_{II} in 8(d): $\pm(x, y, z; \frac{1}{2} - x, \frac{1}{2} + y, \frac{1}{2} - z; \bar{x}, \bar{y}, \frac{1}{2} + z; \frac{1}{2} + x, \frac{1}{2} - y, \bar{z})$, and the remaining four anions X_I in 4(c). Coordinates for the ions in **$GdFeO_3$** are also given in Fig. 5.

The buckling of the corner-shared octahedra decreases the cation-anion-cation angle Φ from 180°. If the B cations and the anions are distinguished as $B_1(\frac{1}{2}, 0, 0)$, $B_2(0, \frac{1}{2}, 0)$, $B_3(\frac{1}{2}, 0, \frac{1}{2})$, $X_{II}(\frac{1}{2} + x, \frac{1}{2} - y, \bar{z})$, and $X_I(\frac{1}{2} - x, \frac{1}{2} + y, \frac{1}{4})$, then the two representative angles are $\Phi_{ab} = (B_1 - X_{II} - B_2)$ and $\Phi_c = (B_2 - X_I - B_3)$. GILLEO [*Gi4*] has estimated that in **$La(Co_{0.2}Mn_{0.8})O_3$** these angles are $\Phi_{ab} = 150° \pm 3°$ and $\Phi_c = 177° \pm 3°$ with $B_1 - O_{II} = 1.95$ Å, $B_2 - O_{II} = 2.10$ Å, $B_1 - O_I = B_3 - O_I = 1.96$ Å. The angles in **$GdFeO_3$** are similar.

3.1.2.3 Rhombohedral structures

Where there is no buckling of the octahedra, the perovskites ABX_3 may have a small deformation from cubic to rhombohedral symmetry. Where this deformation does not enlarge the unit cell, it is possible to index it either on a unit cell containing two formula units, as shown in Fig. 6, or on a unit cell containing one formula unit. The corresponding rhombohedral angles are $\alpha \approx 60°$ or $\alpha \approx 90°$. In the early literature, detailed anion positions were not known, and it was common to use the smaller cell with $\alpha \approx 90°$. However, the anions are generally displaced so as to require the larger unit cell of Fig. 6, which has $\alpha \approx 60°$.

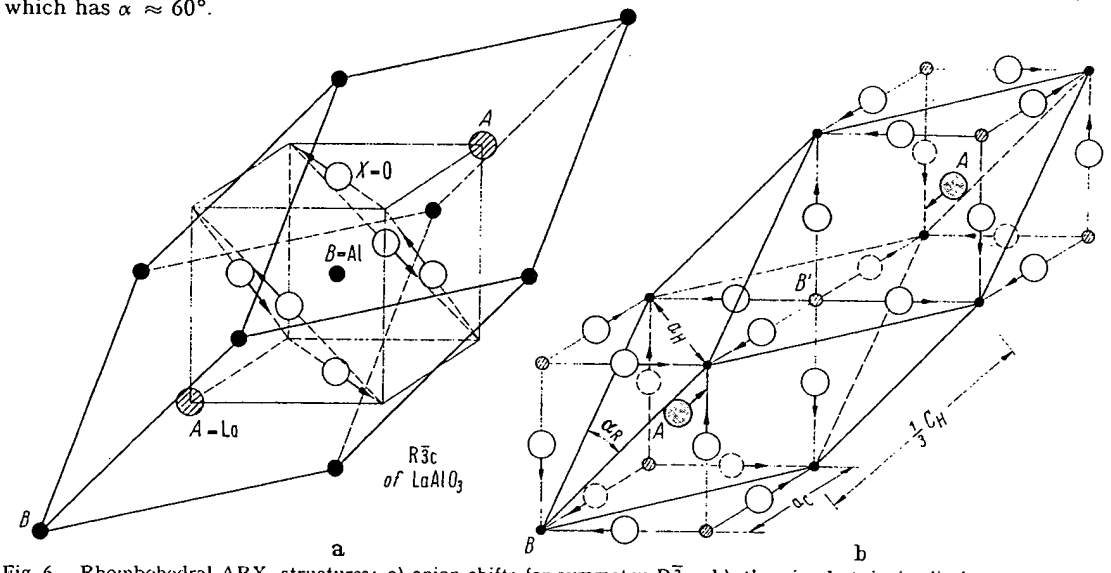

Fig. 6. Rhombohedral ABX_3 structures: a) anion shifts for symmetry R$\bar{3}$c; b) the simplest ionic displacements, corresponding to symmetry R$\bar{3}$m for ordered $A_2BB'X_6$ structures having $r_{B'} > r_B$ [*Ra3*].

Anion displacements from their ideal positions may be of three different types: (1) AX_3(111) planes remain equidistant from neighboring B-cation (111) planes, leaving all the B-cations equivalent. Within these planes, three A—X distances are reduced and three are enlarged via cooperative rotations of the B-cation octahedra, as shown in Fig. 6(a). (2) The anions may move within pseudocubic {110} planes including the B-B axes so as to create two distinguishable B positions: B positions having a shorter B-X separation and B' positions having a larger B'-X separation. This gives the symmetry R$\bar{3}$m, which allows the A cations to be displaced along the [111] axis so as to make the separations B-A ≠ B'-A. (3) In the most general case, the anion displacements may be decomposed into R$\bar{3}$c and R$\bar{3}$m components. The resulting symmetry R$\bar{3}$ also gives distinguishable B and B' positions via its R$\bar{3}$m component.

Although the distinction between these possibilities has been determined in only a few cases, it appears that R$\bar{3}$c can be anticipated unless there is a physical reason for creating two distinguishable positions B and B'. This conclusion is based on the fact that **$LaAlO_3$** has been shown to have the symmetry R$\bar{3}$c by neutron diffraction, [*De14*] nuclear quadrupole resonance [*Mu5*], electron-spin resonance, [*Ki3*] and x-ray techniques [*Ge4b, De17*]. It is strongly supported by the observation [*Ra3*] that **$LaCoO_3$** has the symmetry R$\bar{3}$c at low temperatures, where all of the trivalent cobalt are in their low-spin state, but has the symmetry R$\bar{3}$ at higher temperatures where thermal activation creates a nearly equal population of high-spin and low-spin cobalt ions. These are crystallographically distinguishable, via different ionic radii, as B and B'.

3.1.3 The influence of localized-electron ordering

3.1.3.1 Crystal-field theory

Crystal-field theory rests on the assumption that the outer electrons to be described are localized at discrete atomic positions. This assumption is valid for outer f electrons; it is valid for d electrons in fluorides and in many oxides. Given this assumption, the Schroedinger equation $\mathscr{H}\psi = E\psi$ that describes the localized orbitals and their energies contains the Hamiltonian

$$\mathscr{H} = \mathscr{H}_0 + V_{el} + V_{cub} + (V_{LS} + V_{ncub} + V_\lambda + \sum_j V_{ij}) \tag{2}$$

where $\mathscr{H}_0$ is the Hamiltonian for a hydrogen-like, spherical potential, V_{el} is the atomic correction for spherical symmetry that enters if there is more than one outer d electron, and V_{cub} is the energy correction due to the cubic component of the crystalline fields. For outer d electrons, V_{el} and V_{cub} are generally $\approx$1 eV, and the ion is in a high-spin or a low-spin state depending upon the relative magnitudes of these two terms. In the case of $3d$ electrons, the perturbations listed within the parentheses are all <0.1 eV, and they must be considered simultaneously. $V_{LS} = \lambda \boldsymbol{L}\cdot\boldsymbol{S}$ is the spin-orbit coupling energy, and covalent mixing reduces slightly the parameter λ from its free-atom value. V_{ncub} is the noncubic component of the crystalline field, V_λ is the elastic coupling energy associated with cooperative local distortions, and V_{ij} is the magnetic exchange energy coupling localized atomic moments on neighboring cations.

Solution of the zero-order equation $\mathscr{H}_0\psi = E\psi$ gives hydrogenic wave functions $f_{l,m} = R_l(r)\,Y_l^m(\theta,\phi)$. From the spherical harmonics $Y_l^m(\theta,\phi)$, the d electrons ($l = 2$) have the following angular dependence and azimuthal-angular-momentum quantum number m derived from $L_z f = -i\hbar\partial f/\partial\phi = m\hbar f$:

$$\begin{aligned} f_A &\sim (3z^2 - r^2)/r^2 &&= (3\cos^2\theta - 1); && m = 0 \\ (f_D \pm i f_E) &\sim 2(zx \pm iyz)/r^2 &&= \sin 2\theta \exp(\pm i\phi); && m = \pm 1 \\ (f_B \pm i f_C) &\sim (x^2 - y^2 \pm i2xy)/r^2 &&= \sin^2\theta \exp(\pm i2\phi); && m = \pm 2 \end{aligned} \tag{3}$$

where θ, ϕ are conventional spherical coordinates. The perturbation V_{el} reflects the fact that outer electrons of parallel spin are excluded from one another and therefore screen each other less from the positive atomic nucleus than do those of antiparallel spin. This correction is responsible for Hund's highest-multiplicity rule for the free atoms. It influences the radial part of the wave function, and hence the relative energies of states of different spin, but not the angular part.

Given the cartesian axes at a B cation formed by the principal axes of its octahedral interstice, the five d orbitals of Eq. (3) are separated into two symmetry groups; f_A and f_B, which are directed along the cartesian axes toward near-neighbor anions, have E_g symmetry and are referred to as e_g orbitals; f_C, f_D, and f_E, which are more stable because they are directed away from the near-neighbor anions, have T_{2g} symmetry and are referred to as t_{2g} orbitals. The principal contribution to the cubic-field splitting 10 Dq of T_{2g} and E_g energies is due to covalent mixing, not to electrostatic energies as calculated on a point-charge model. If covalent mixing with the near-neighbor anionic and A-cationic orbitals is introduced, then the crystalline localized orbitals of t_{2g} and e_g symmetry become

$$\begin{aligned} \psi_t &= N_t(f_t - \lambda_\pi\phi_\pi + \lambda_A\phi_A) \\ \psi_e &= N_e(f_e - \lambda_s\phi_s - \lambda_\sigma\phi_\sigma) \end{aligned} \tag{4}$$

where f_t and f_e are linear combinations of the atomic f_C, f_D, f_E and f_A, f_B orbitals. The symmetrized anionic p_π, s and p_σ orbitals are ϕ_π, ϕ_s and ϕ_σ; the symmetrized A-catonic s, p orbitals are ϕ_A. The covalent-mixing parameters λ_σ, λ_π, λ_A, λ_s are roughly proportional to the overlap integral for atomic orbitals on neighboring ions and inversely proportional to their energy separation. Initially, the energy separations of cationic d and ϕ_σ or ϕ_π are given by $E_M - E_I$, the difference between the Madelung energy and ionization potentials for the "effective" ionic charges, so that by symmetry

$$10\,Dq = \Delta_M + (\lambda_\sigma^2 - \lambda_\pi^2)(E_M - E_I),\ \lambda_\pi < \lambda_\sigma \tag{5}$$

where Δ_M is any electrostatic contribution to 10 Dq. The one-electron crystal-field splitting of the d-state manifold is shown in Fig. 7(a). The relationship $\lambda_\pi < \lambda_\sigma$ has been confirmed by nuclear magnetic resonance studies of **$KMnF_3$**, **$KNiF_3$** and **K_2NiCrF_6** [*Sh30, Hu4*]. In these experiments the fractional occupancies by unpaired spins of the $2s$, $2p_\sigma$, and $2p_\pi$ orbitals are:

$$fx_s \equiv 2SA_s/A_{2s} \sim N_e^2\lambda_s^2, \quad fx_\sigma = 2SA_\sigma/A_{2p} \sim N_e^2\lambda_\sigma^2, \quad fx_\pi = 2SA_\pi/A_{2p} \sim N_t^2\lambda_\pi^2$$

where A_s is the isotropic component and A_σ, A_π the anisotropic components of the hyperfine interaction tensor A_{ij} entering the nuclear spin-electron spin coupling energy $\Sigma_j \boldsymbol{I}_i\cdot\mathbf{A}_{ij}\cdot\boldsymbol{S}_j$. Interpretation of the phenomenological parameters λ_π, λ_σ and 10 Dq has been discussed extensively [*Hu4*].

With more than one outer d electron or d hole, it is necessary to introduce V_{el}, which is responsible for Hund's highest multiplicity rule (highest net S and L) for the free atoms. For four outer electrons, the atomic ground term is therefore ^5D. In a crystal, this rule may break down as a result of the crystalline

fields. Schematically, the Hund splitting Δ_{ex} for states of different spin and the one-electron splitting 10 Dq may be represented on the same energy diagram, as shown in Fig. 7(b). It follows from this figure that with four to eight outer d electrons, the magnitude of the net ground-state spin depends upon whether (Δ_{ex} − 10 Dq) is positive or negative. If $\Delta_{ex} > 10$ Dq, the ion is in a high-spin state; if $\Delta_{ex} < 10$ Dq,

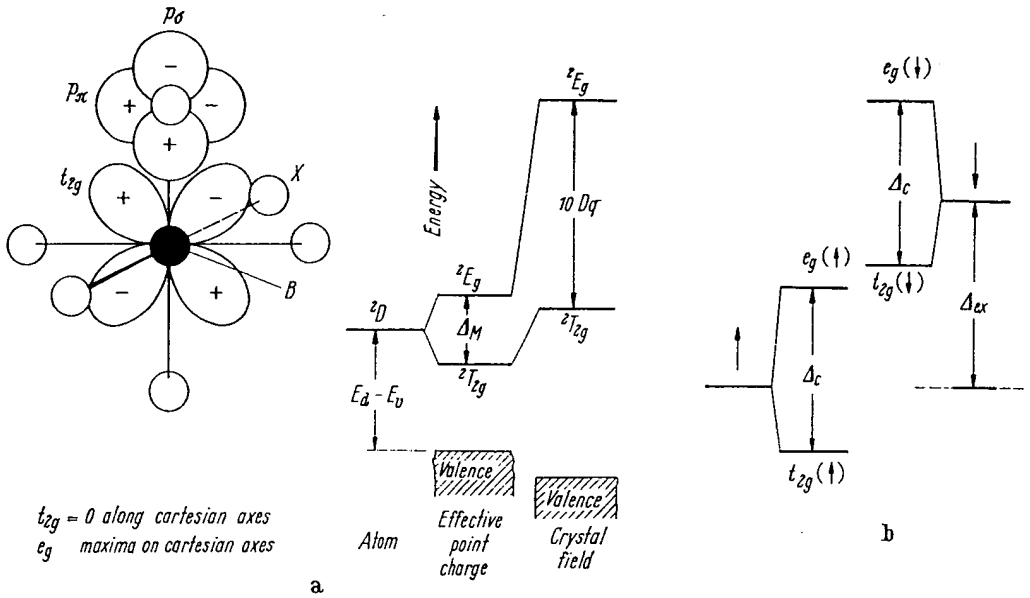

Fig. 7. One-electron crystal-field splitting of the d-state manifold of a transition-metal B cation in a cubic perovskite: a) $\Delta_{ex} = 0$ and b) schematically for $\Delta_{ex} \neq 0$, corresponding to more than one outer d electron.

Hund's rule breaks down and the ion is in a low-spin state. Since Δ_{ex} decreases with larger radial extension of the crystalline wave functions, it decreases with increasing covalent-mixing parameters λ_σ, λ_π. Simultaneously, from Eq. (5) it follows that 10 Dq increases with increasing covalency. Therefore there is a critical amount of covalent bonding beyond which Hund's rule breaks down. Covalency with a particular anionic sublattice increases with cationic charge and on going to the right through any long period of the periodic table. In oxides with the perovskite structure, only divalent and trivalent ions of the first long period are high-spin. Of these, trivalent nickel is low-spin and trivalent cobalt exhibits a variable high-spin to low-spin population as a function of temperature.

In general, it is necessary to use a multi-electron notation for the outer d electrons. Whereas atomic D states are split by the crystalline fields as shown in Fig. 7, atomic F states are split as shown in Fig. 8.

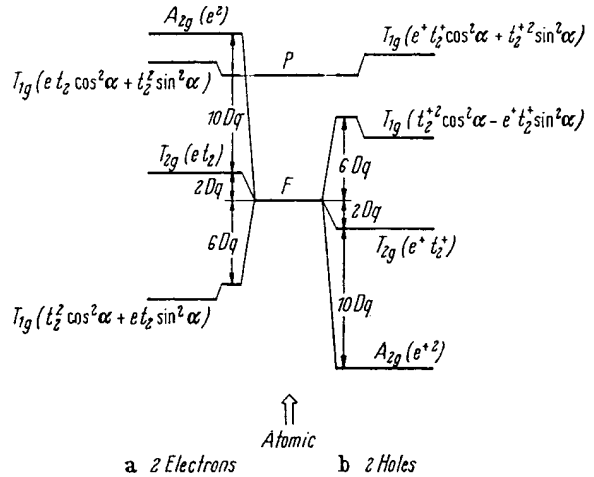

Fig. 8. Octahedral-site splitting of atomic F states: a) two-electron ^3F states and b) two-hole ^3F states.

Because the operator $L_z = -i\hbar\partial/\partial\phi$ is imaginary, the crystal-field splitting of f_B and f_C quenches the orbital angular momentum associated with these orbitals, so that the e_g orbitals have $m = 0, 0$ and the t_{2g} orbitals have $m = 0, \pm 1$. An isomorphism between f_C, f_D, f_E and atomic P orbitals simplifies calculation of V_{LS}. It is possible to treat the t_{2g} orbitals as atomic P orbitals if the sign of the spin-orbit-coupling

parameter λ is reversed [*Gr9*]. Therefore ground states having an orbital degeneracy and $m \neq 0$ are split by V_{LS} into $(2J + 1)$ multiplet states corresponding to states of different $J = L + S$. However, the order of the levels is inverted (largest J lowest for less than five d electrons, smallest J lowest for more than five d electrons) because of the change in sign of λ. According to the Landé interval rule, the separation between states J and $J + 1$ is $|\lambda|(J + 1)$. The first-order multiplet splittings, which do not include mixing of higher states of similar symmetry, are shown in Fig. 9 for Fe^{2+} and Co^{2+} ions. Note that the term is now identified by its symmetry character T_{2g} or T_{1g} rather than by its atomic orbital-momentum character D or F. Tab. 1 summarizes the various symmetry notations for different spin states.

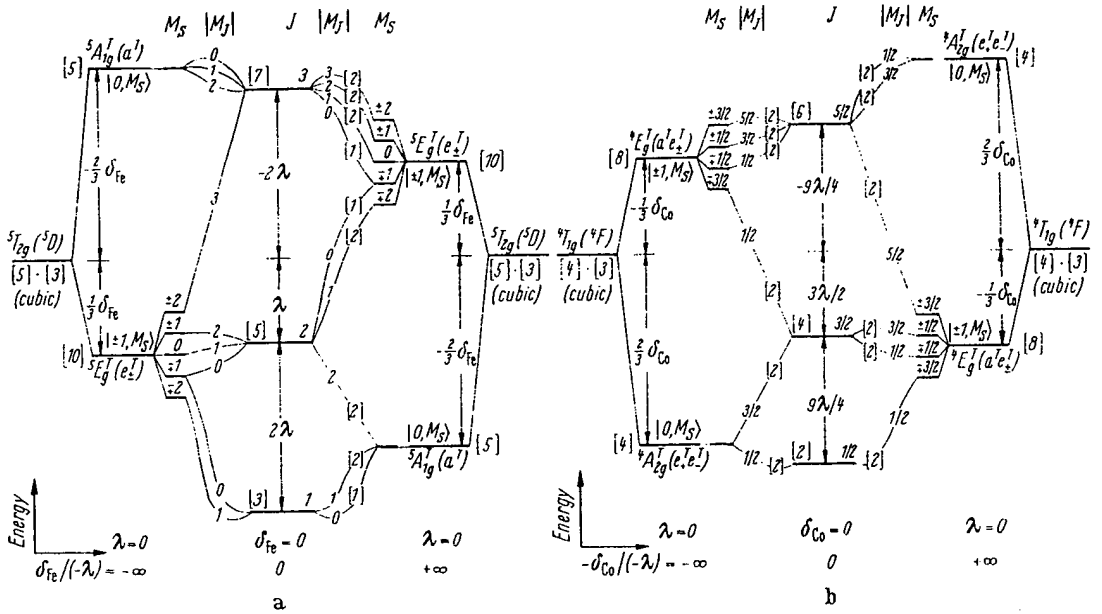

Fig. 9. Schematic spin-orbit plus trigonal-field, or tetragonal-field, splittings of cubic-field levels as a function of the ratio $\delta/(-\lambda)$ for a) ${}^5T_{2g}$ level of Fe^{2+} and b) ${}^4T_{1g}$ level of Co^{2+}.

Spin-orbit coupling introduces an axial symmetry to the charge distribution, where the spin (or atomic-moment) defines the axis. Therefore, if there is a noncubic component to the crystalline field ($V_{\text{n cub}} \neq 0$), then there is a spin-lattice interaction via the orbital-lattice interaction that introduces a magnetic anisotropy. For localized electrons, this is a local, one-ion anisotropy. Conversely, if the spins are ordered below some transition temperature, then the local interstices have time to relax about the noncubic charge distribution, thereby distorting the octahedral site. Therefore there is an intimate connection between the noncubic symmetry and the magnitude of the multiplet splitting. The noncubic component is usually parametrized as

$$V_{\text{n cub}} = \delta(L_z^2 - \tfrac{2}{3}), \tag{6}$$

and Fig. 9 includes the total perturbation $V_{LS} + V_{\text{n cub}}$ of the one-electron and two-electron ground states.

With one or two holes in a half-shell, the one-electron and two-electron energy diagrams are inverted. In these cases $M_L = \Sigma_i m_i = 0$, so that $V_{LS} = 0$, and there is no multiplet splitting.

Tab. 1 also displays the general ground-state wave functions for a magnetically ordered phase having collinear spins. The coefficients a_1, a_2, a_3 of the Kramers' doublets and b_1, b_2 of the singlets all depend upon the relative magnitudes of the five perturbation terms $V_{LS} + V_{\text{n cub}} + V_\lambda + \mathcal{H}_Z$ where $\mathcal{H}_Z$ is the Zeeman energy due to the internal molecular field resulting from magnetic order. The molecular-field approximation is used for the first-order, isotropic magnetic-coupling energy $\mathcal{H}_{ex}$, which is the dominant term in $\sum_j V_{ij}$ [see discussion of Eq. (13)]. This gives

$$\mathcal{H}_Z \approx 2J_p \langle S \rangle S_z \tag{7}$$

where J_p, the sum of all near-neighbor exchange parameters, can be determined from the temperature dependence of the magnetic susceptibility and z is along the axis of the average spin $\langle S \rangle$ on the neighboring cations. This term contributes to the spectroscopic-splitting factor g, and hence to the net atomic moment, if $V_{LS} \neq 0$. In Tab. 1, the components of the wave functions are designated by the notation $|M_L, M_S>$, where M_L, M_S are the azimuthal quantum numbers for the net orbital and spin momenta.

Tab. 1. Lowest terms and ground state wave function for octahedral-site cations having n localized outer d electrons

n	Ion	$t^n e^m$	V_{el}	V_{cub}	V_{LS}	$V_{LS} + V_{n\,cub}(\delta < 0) + \mathscr{H}_Z$	$V_{LS} + V_{n\,cub}(\delta > 0) + \mathscr{H}_Z$
1	Ti^{3+}, V^{4+}, W^{5+}, Re^{6+}	t^1e^0	^2D	$^2T_{2g}$	$J = \frac{1}{2}$	$\mid +1, +\frac{1}{2} >$	$a_1 \mid 0, +\frac{1}{2} > + a_2 \mid +1, -\frac{1}{2} >$
2	V^{3+}, Cr^{4+}, Mo^{4+}	t^2e^0	^3F	$^3T_{1g}$	$J = 2$	$\mid +1, +1 >$	$b_1 \mid +1, -1 > + b_2 \mid 0, 0 > + b_3 \mid -1, +1 >$
3	V^{2+}, Cr^{3+}, Mn^{4+}, Mo^{3+}	t^3e^0	^4F	$^4A_{2g}$	$J = \frac{3}{2}$	$\mid 0, +\frac{3}{2} >$	$\mid 0, +\frac{3}{2} >$
4	Cr^{2+}, Mn^{3+}	t^3e^1	^5D	^5E_g	$J = 2$	$^5B_{1g} \mid 0, +2 >$	$^5A_{1g} \mid 0, +2 >$
	Fe^{IV}, Ru^{IV}, Os^{IV}	t^4e^0		$^3T_{1g}$	$J = 0$	$b_1 \mid +1, -1 > + b_2 \mid 0, 0 > + b_1 \mid -1, +1 >$	$b_1' \mid +1, -1 > + b_2' \mid 0, 0 > + b_1' \mid -1, +1 >$
5	Mn^{2+}, Fe^{3+}	t^5e^2	^6S	$^6A_{1g}$	$J = \frac{5}{2}$	$\mid 0, +\frac{5}{2} >$	$\mid 0, +\frac{5}{2} >$
	Ir^{IV}	t^5e^0		$^2T_{2g}$	$J = \frac{1}{2}$	$a_1 \mid 0, +\frac{1}{2} > + a_2 \mid +1, -\frac{1}{2} >$	$a_1' \mid 0, +\frac{1}{2} > + a_2' \mid +1, -\frac{1}{2} >$
6	Fe^{2+}, Co^{3+}	t^4e^2	^5D	$^5T_{2g}$	$J = 1$	$a_1 \mid -1, +2 > + a_2 \mid 0, +1 > + a_3 \mid +1, 0 >$	$b_1 \mid +1, -1 > + b_2 \mid 0, 0 > + b_1 \mid -1, +1 >$
	Co^{III}, Rh^{III}, Pt^{IV}	t^6e^0		$^1A_{1g}$	$J = 0$	$\mid 0, 0 >$	$\mid 0, 0 >$
7	Co^{2+}	t^5e^2	^4F	$^4T_{1g}$	$J = \frac{1}{2}$	$a_1 \mid -1, +\frac{1}{2} > + a_2 \mid 0, +\frac{1}{2} > + a_3 \mid +1, -\frac{1}{2} >$	$a_1' \mid -1, +\frac{1}{2} > + a_2' \mid 0, +\frac{1}{2} > + a_3' \mid +1, -\frac{1}{2} >$
	Ni^{III}	t^6e^1		^2E_g	$J = \frac{1}{2}$	$^2B_{1g} \mid 0, +\frac{1}{2} >$	$^2A_{1g} \mid 0, +\frac{1}{2} >$
8	Ni^{2+}, Pd^{2-}	t^6e^2	^3F	$^3A_{2g}$	$J = 1$	$\mid 0, +1 >$	$\mid 0, +1 >$
9	Cu^{2+}	t^6e^3	^2D	^2E_g	$J = \frac{1}{2}$	$^2B_{1g} \mid 0, +\frac{1}{2} >$	$^2A_{1g} \mid 0, +\frac{1}{2} >$

3.1.3.2 Jahn-Teller distortions

If the cubic-field ground state of the B cation is an orbitally two-fold-degenerate E_g state, then the t_{2g} orbitals are either full or half-filled, so that $M_L = 0$, and there is no spin-orbit coupling ($V_{LS} = 0$). JAHN and TELLER [*Ja6*] have shown that, if there is no perturbation available to remove a ground-state orbital degeneracy, then there will be a spontaneous distortion to lower local symmetry below some transition temperature $\Theta_{trans} < T_{melt}$ where T_{melt} is the melting point. Since the energy gained by a local distortion is reduced by the work done against the elastic restoring forces of the crystal, transition temperatures Θ_{trans} are small for isolated ions. However, if all of the B cations are similar, then cooperative distortions are possible, and the net energy gained per ion is much greater because of the elastic-coupling energy V_λ of Eq. (2). Such a cooperative phenomenon is characterized by thermal hysteresis and a definite (usually first-order) transition temperature. Since they are due to electronic ordering, such transitions are martensitic.

VAN VLECK [*Va15*] pointed out that the normal vibrational modes that split an E_g electronic state are themselves twofold-degenerate with symmetry E_g. One mode gives the interstice a tetragonal distortion, the other an orthorhombic distortion. It follows that, from first-order theory, there is no static distortion of the interstice, only a dynamic coupling between the electronic charge density and the vibrational modes. Moreover, this dynamic coupling greatly enhances the two E_g vibrational modes and gives a dynamic splitting of the electronic E_g state. This mechanism has important consequences for the acoustic properties and, as discussed in 3.3, for the sign of the magnetic superexchange coupling.

Inclusion in the theory of higher-order coupling terms and anharmonic elastic terms shows that a static, tetragonal ($c/a > 1$) distortion of the interstice is stable below some Θ_{trans} [*Ka10*]. This sign for the static distortion was first established experimentally through the interpretation [*Go15*] and further study of cooperative tetragonal-to-cubic transitions in spinel systems. However, application to the perovskites requires a solution of the lowest-energy cooperative distortion via inclusion of the elastic-coupling energy V_λ. GOODENOUGH [*Go6*] proposed that individual tetragonal ($c/a > 1$) octahedra order their long axes alternately along [100] and [010] axes of the pseudocubic cell. KANAMORI [*Ka10*] generalized this solution to include an orthorhombic component to the local-octahedron distortions. This gives B-B separations within (001) planes having a long (l) and a short (s) B-X separation and along the [001] axis two intermediate (m) B-X separations where $s < m < (l + s)/2$. This prediction was later verified by HEPWORTH and JACK [*He9*] for □ **MnF_3** and by OKAZAKI [*Ok1*] for **$KCuF_3$** (see Fig. 10). Superposition of this distortion on an O-orthorhombic cell stabilizes the unique axis along the orthorhombic c-axis, and

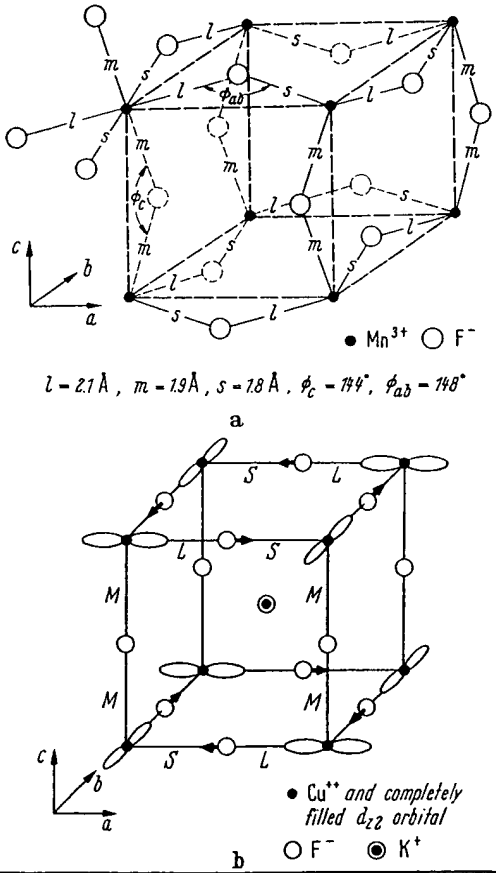

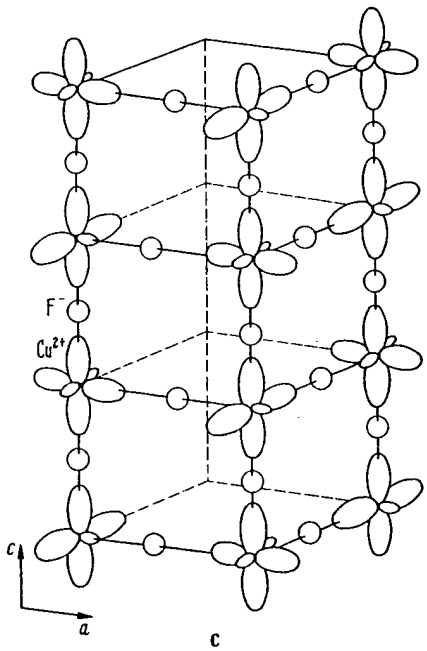

Fig. 10. Cooperative Jahn-Teller distortions in a) □MnF_3 and b) $KCuF_3$. c) Configuration of hole-orbitals at Cu^{2+} ions of tetragonal $KCuF_3$ [*He9, Ok1*].

the axial ratios of the O-orthorhombic cell are transformed from $a < c/\sqrt{2}$ to $c/\sqrt{2} < a$. To signal the fact that a Jahn-Teller distortion (with or without spin-orbit coupling) has been superposed on a distortion due to relative ionic sizes, the notation O'-orthorhombic is used in Tab. 2 wherever $c/\sqrt{2} < a$.

The important B cations that exhibit dynamic and static JAHN-TELLER stabilizations in the absence of spin-orbit coupling are: Cu^{2+} $^2E_g(t_{2g}^6e_g^3)$, Cr^{2+} and Mn^{3+} $^5E_g(t_{2g}^3e_g^1)$, Ni^{III} $^2E_g(t_{2g}^6e_g^1)$, where Roman numerals are used for the valence state of a low-spin cation. Tab. 2 shows that O'-orthorhombic symmetry above a magnetic-ordering temperature is associated with these ions, provided the d electrons are localized, and only with these ions, with the exception of $\mathbf{LaVO_3}$ and $\mathbf{CeVO_3}$, where sharply enhanced distortions appear abruptly below Θ_N [*Ro3*; *Go10*]. The cubic $^3T_{1g}$ state of V^{3+} is orbitally threefold-degenerate, so that it may induce small distortions above Θ_N, larger distortions below Θ_N (see discussion *Go14*). $\mathbf{LaNiO_3}$ remains $R\bar{3}c$ because the e_g electrons are collective. In $\mathbf{La_2Li_{0.5}Ni_{0.5}O_4}$ crystals, on the other hand, the ordered Ni^{III} ions have localized e_g electrons, and there is a tetragonal ($c/a > 1$) distortion. The sign of this distortion is manifest by the large c/a ratio. Strictly speaking, this is not a Jahn-Teller distortion, since the K_2NiF_4 structure is tetragonal, but ordering of the localized electron of unpaired spin in the tetragonal field distorts the Ni^{III} octahedra to tetragonal symmetry with axes parallel to the unique axis. Pure Jahn-Teller distortions can be distinguished from distortions associated with spin-orbit coupling because they are independent of magnetic order and generally occur at a Θ_{trans} above the magnetic-ordering temperature.

3.1.3.3 Spin-orbit coupling

B cations having cubic-field ground-state terms T_{2g} or T_{1g} are orbitally threefold-degenerate with $M_L = 0, \pm 1$, so that $V_{LS} \neq 0$. The combined perturbations $V_{LS} + V_{ncub}$ separate into secular equations for different M_J, as shown in Fig. 9. With a single outer electron, the $^2T_{2g}$ cubic-field term is split in two, the energies for different M_J shifting by

$$E_{3/2} = \tfrac{1}{3}\delta - \tfrac{1}{2}\lambda$$
$$E_{1/2}^{\pm} = -\tfrac{1}{6}\delta + \tfrac{1}{4}\lambda \pm \tfrac{1}{2}\{\delta^2 + \lambda\delta + (\tfrac{3}{2}\lambda)^2\}^{1/2} \quad (8)$$

where $\lambda > 0$. In a cubic field

$$E_{3/2} = E_{1/2}^{-} = E_{1/2}^{+} - \tfrac{3}{2}\lambda, \quad (9)$$

and spin-orbit coupling leaves an orbitally twofold-degenerate ground state. Therefore it is necessary to consider an additional Jahn-Teller stabilization via $V_{ncub} + V_\lambda + \mathscr{H}_Z$. GOODENOUGH [*Go14*] has shown that it is necessary to consider two temperature regions: $T > \Theta_N$ and $T < \Theta_N$, where Θ_N is the temperature below which the spins order collinearly. In the paramagnetic domain $T > \Theta_N$, the molecular fields vanish ($\langle S \rangle = 0$) and, from Eq. (7), $\mathscr{H}_Z = 0$. In this case, the ground-state energy varies as (δ^2/λ). Since the work done against elastic restoring forces is $q_2\delta^2$, there is a spontaneous Jahn-Teller distortion, corresponding to $\delta > 0$, at a $\Theta_{trans} > \Theta_N$ only if the product λq_2 is relatively small. In the magnetically ordered state ($T < \Theta_N$), on the other hand, there is an internal molecular field H_{int} at each atom, which produces a Zeeman splitting of the orbitals of different spin. The magnitude of this splitting depends upon the spectroscopic splitting factor, which has the components

$$g_\parallel = 2 - 2g_1(\delta/\lambda) \text{ and } g_\perp = 2 + g_1(\delta/\lambda) \quad (10)$$

where $g_1 > 0$. Therefore the Zeeman splitting in the molecular fields is maximized by making $\delta < 0$ and having the spins parallel to the unique axis defined by δ. Further, this energy is linear in δ, so that a spontaneous distortion should occur at some $\Theta_{trans} < \Theta_N$. A similar argument holds for the orbitally twofold-degenerate $J = 1$ and $J = \frac{1}{2}$ states of octahedral-site Fe^{2+} $^5T_{2g}$ and Co^{2+} $^4T_{1g}$.

In summary, if multiplet splitting leaves a ground state with a twofold, accidental orbital degeneracy, then there is a spontaneous Jahn-Teller distortion at some Θ_{trans} that removes this degeneracy. If $\Theta_{trans} > \Theta_N$, then $\delta > 0$. However, this alternative requires special crystallographic conditions that do not appear to be met in perovskites. On the other hand, a $\Theta_{trans} \leq \Theta_N$ and $\delta < 0$ can be generally anticipated wherever the spins order collinearly and the d electrons are localized. Further, from Eqs. (3) and (6), it follows that T_{2g} states (one outer t_{2g} electron) have $\delta < 0$ if the site symmetry is tetragonal ($c/a > 1$), whereas T_{1g} states (two outer t_{2g} electrons) have $\delta < 0$ if it is tetragonal ($c/a < 1$). Alternatively, distortions of the site symmetry may be to trigonal symmetry. A $\delta < 0$ corresponds to $\alpha < 60°$ for T_{2g} states, to $\alpha > 60°$ for T_{1g} states. These relationships are also summarized in Tab. 1. Experimentally, Fe^{2+} $^5T_{2g}$ octahedra become trigonal ($\alpha < 60°$) below Θ_N, as exhibited by $\mathbf{KFeF_3}$, whereas Co^{2+} $^4T_{1g}$ octahedra become tetragonal ($c/a < 1$) below Θ_N, as exhibited by $\mathbf{KCoF_3}$. Where $\Theta_{trans} = \Theta_N$, the magnetic-ordering temperature may be first-order. In addition, the spontaneous distortions introduce large magnetostriction and magnetic anisotropy.

The cubic-field ground state of V^{3+} $^3T_{1g}$ is orbitally threefold-degenerate. As a result, any spontaneous distortion must correspond to $\delta < 0$, i.e., tetragonal ($c/a < 1$) or trigonal ($\alpha > 60°$). However, as in the other cases a $\Theta_{trans} \lesssim \Theta_N$ is to be expected in the perovskite structure. The V^{3+} ion generally occurs in an O-orthorhombic perovskite, and superposition of a tegragonal ($c/a < 1$) distortion with coincident unique axes again results in O'-orthorhombic symmetry. The perovskite $\mathbf{LaVO_3}$ exhibits an abrupt contraction of the c-axis on cooling through Θ_N.

3.1.4 The influence of collective-electron ordering

3.1.4.1 Band theory

Conventional band theory rests on three principal assumptions: (1) A description of the outer electrons may be built up from solutions of a single electron moving in a periodic potential. (2) Multiplet structure on individual atoms may be disregarded. (3) Electron-phonon interactions may be treated as a small perturbation. For an infinite crystal, the unperturbed solution of running waves in a periodic potential gives the Bloch functions and energies

$$\psi_{km} = \exp(i\boldsymbol{k}\cdot\boldsymbol{r})\, u_{km}(\boldsymbol{r});\ E_k = E_0 + \hbar^2k^2/2m^* \tag{11}$$

where $\hbar\boldsymbol{k}$ is the momentum of an electron of effective mass m^* and $u_k(\boldsymbol{r})$ is a periodic function. In the tight-binding approximation appropriate for narrow bands, the Bloch functions are

$$\psi_k(\boldsymbol{r}) = 1/\sqrt{N}\sum_{n=1}^{N}\exp(i\boldsymbol{k}\cdot\boldsymbol{R}_n)\, w(\boldsymbol{r}-\boldsymbol{R}_n)$$

where $w(\boldsymbol{r}-\boldsymbol{R}_n)$ is a localized wave function for the atom at $\boldsymbol{R}_n$ defined by

$$w(\boldsymbol{r}-\boldsymbol{R}_n) = 1/\sqrt{N}\sum_{n}\exp[i\boldsymbol{k}\cdot(\boldsymbol{r}-\boldsymbol{R}_n)]u_k(\boldsymbol{r})$$

and $u_k(\boldsymbol{r})$ is a localized crystalline orbital. At the Brilloin-zone boundries defined by

$$2\boldsymbol{k}\cdot\boldsymbol{K} + |\mathrm{K}|^2 = 0, \tag{12}$$

where $\boldsymbol{K}$ is a reciprocal lattice vector, there are energy discontinuities in energy-momentum space. In polar insulators, this introduces an energy gap E_g between occupied, primarily anionic states and empty, primarily cationic states. Cooperative displacements δ of the cationic sublattice relative to the anionic sublattice may increase this gap, thereby stabilizing the total energy of the occupied states by $\varepsilon_2\delta^2$. Since the resulting elastic-strain energy is $q_2\delta^2$, there can be a spontaneous displacement only for the exceptional case $q_2 < \varepsilon_2$ and a ground state corresponding to a small distortion parameter δ. In this case vibrational entropy may stabilize the higher symmetry at the higher temperatures. This differs from the usual criterion for spontaneous distortions, where a term linear in δ is identified. There appear to be two situations occuring in perovskites where the requirement $q_2 < \varepsilon_2$ is met: (1) Where B-cations have empty d orbitals, there is a critical range of covalent-mixing parameters through which the site preference changes from octahedral to tetrahedral. In this range q_2 is very small for B-cation displacements within an octahedron that reduce the coordination number from six towards four. The origin of the small q_2 is a balance of the electrostatic energy lost and covalent-bond energy gained on going to smaller anion coordination. (2) The high polarizability of the outer core electrons of Pb^{2+} and Bi^{3+} ions makes q_2 relatively small, so that displacements that permit a relatively large ε_2 can occur spontaneously.

What distinguishes these spontaneous distortions from those due to an ordering of localized electrons is the displacement of the cations from the centers of symmetry of their interstices. (The Jahn-Teller distortions, with or without spin-orbit coupling, leave the cations in the centers of symmetry of their interstices.) Unlike the structures, such as corundum, where pairs of octahedra share a common face, these cationic displacements from the centers of symmetry of their interstices do not follow from point-charge electrostatic arguments. In polar insulators, these displacements lead to ferroelectricity or antiferroelectricity, and they often induce displacements of neighboring cations. Further, where the requirement $q_2 \approx \varepsilon_2$ occurs just above Θ_{trans}, there must be a strong interaction of the bonding (mostly anionic) electrons with those vibrational modes that anticipate the cooperative ionic displacements below Θ_{trans}. These "soft" vibrational modes impart several anomalous physical properties, including a high electric susceptibility.

3.1.4.2 Distortions due to B-X bonding

Transition-metal cations having no outer d electrons have the following site preferences:

Sc^{3+}	$\underline{Ti^{4+}}$	$\underline{V^{5+}}$	Cr^{6+}	Mn^{7+}
Y^{3+}	Zr^{4+}	$\underline{Nb^{5+}}$	$\underline{Mo^{6+}}$	Tc^{7+}
	Hf^{4+}	$\underline{Ta^{5+}}$	$\underline{W^{6+}}$	$\underline{Re^{7+}}$

where cations at the left of each row have definite octahedral-site (or larger anion coordination) preference and those to the right have definite tetrahedral-site preference. Those underlined by a solid line may be stabilized in the octahedral sites of a perovskite-type structure, but they tend to induce spontaneous ferroelectric or antiferroelectric distortions, the ions moving cooperatively out of the centers of symmetry of their interstices. The ions underlined by dashed lines only occur in ordered perovskites $A_2BB'O_6$ and $A_3BB'_2O_9$. In general, they are found in tetrahedral sites or in strongly distorted octahedral sites. However, in the ordered perosvkites they are able to strongly polarize the anion near neighbors so as to stabilize the octahedral symmetry.

It is significant that spontaneous ferroelectric distortions are only induced by B cations if these are transition-metal cations having empty d orbitals. It is also significant that the change from octahedral-site to tetrahedral-site preference is associated with a relative stabilization of the d orbitals (larger atomic number in any long period) as well as with a decrease in ionic size. (The ionic radii decrease in the order Y^{3+}, Sc^{3+}, Hf^{4+}, Zr^{4+}, Ta^{5+}, Nb^{5+}, Ti^{4+}, W^{6+}, Mo^{6+}, Re^{7+}, V^{5+}, Tc^{7+}, Cr^{6+}, Mn^{7+}). The greater the relative stability of the d orbitals, the larger are the parameters λ_σ and λ_π of Eq. (4), and these are enhanced by any displacement that decreases a B-X separation. Such an enhancement stabilizes the occupied states at the expense of the d states, and a net stabilization can occur if the d states are empty. Also the smaller the cationic size, the smaller the elastic resistance to displacements within an octahedral interstice. (Phenomenological ionic models for the ferroelectric distortions have also been given [*Me7, Ha33*].)

There are three B-cation displacements relative to their octahedral interstices that would simultaneously stabilize the occupied anionic p_π orbitals relative to the unoccupied t_{2g} orbitals: (1) *Tetragonal symmetry*. Displacements along an [001] axis that create alternate long and short B-X distances along this axis would stabilize s, p_σ and the two p_π orbitals per anion on this axis and strongly polarize the charge density toward the short B-X separation. (2) *Orthorhombic symmetry*. Displacement along a [110] axis that created two shortest and two longest B-X distances would stabilize the s, p_σ and the two p_π orbitals per anion on two out of the three cartesian axes. (3) *Rhombohedral symmetry*. Displacement along a [111] axis would stabilize the s, p_σ and the two p_π orbitals per anion on all the anions. These three possibilities are illustrated in Fig. 11.

Such distortions also induce changes in the A-X separations, and the particular cooperative distortion that is stabilized depends upon the character of the A-X bonding. The covalency contribution to the A-X bond increases with formal A cationic charge; for a fixed charge it decreases with increasing atomic number of the A cation down any column of the periodic table. If A-X covalent bonding is relatively strong and the perovskite is distorted to O-orthorhombic symmetry, all ferroelectric distortions may be quenched because the p_π orbitals are stabilized by σ-bonding with the A cations. This appears to be illustrated by $\mathbf{CaTiO_3}$, and almost so by $\mathbf{SrTiO_3}$. On the other hand, if the A atom is stabilized by a polarization of its outer core electrons (Pb^{2+} and Bi^{3+} as discussed in 3.1.4.3), then a tetragonal, ferroelectric distortion is stabilized so as to allow a cooperative displacement of the A and B cations, the A cation moving along the [001] axis to stabilize two p_π orbitals per anion not on [001] axes. This is illustrated by the $\mathbf{PbTiO_3}$ structure of Fig. 12. If the covalency contribution to the A-X bonding is relatively weak, then the B-X covalency contribution should dominate. For large A cations ($t > 0.9$), this would stabilize a ferroelectric, rhombohedral distortion at lowest temperatures, as illustrated by $\mathbf{BaTiO_3}$. As the temperature increases, successive distorted structures ($R_B^F \rightarrow O_B^F \rightarrow T_B^F \rightarrow C$) introduce incremental additions to the entropy. However, a small A cation and weak A-X covalency contribution may lead to a ferroelectric distortion superposed on the O-orthorhombic structure to give the O_B^*-orthorhombic structure of $\mathbf{CdTiO_3}$ or $\mathbf{NaTaO_3}$ shown in Fig. 13. Even more complex distortions are found in $\mathbf{NaNbO_3}$ [*Vo6*]. The room-tem-

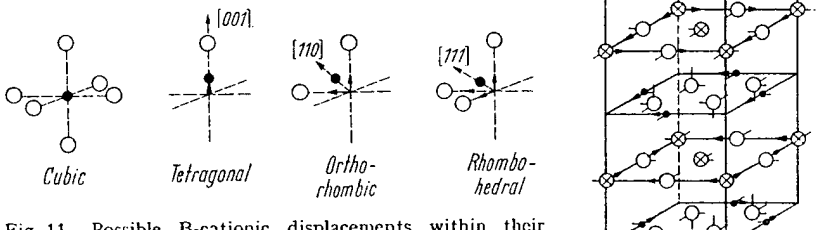

Fig. 11. Possible B-cationic displacements within their octahedra in ferroelectric or antiferroelectric distortions.

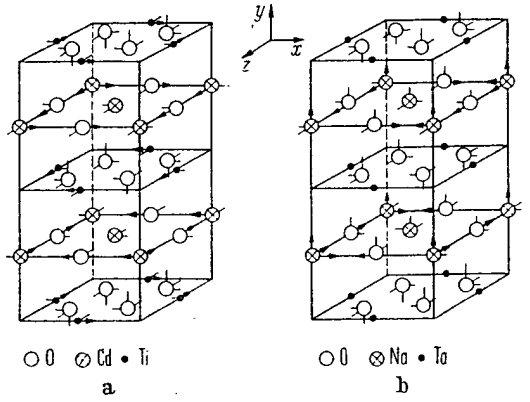

Fig. 13. Ionic displacements in a) $CdTiO_3$ and b) $NaTaO_3$ [*Ka22*].

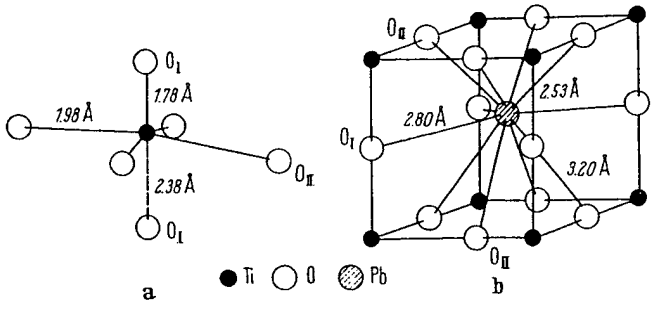

Fig. 12. Tetragonal $PbTiO_3$: a) environment of Ti and b) environment of Pb [*Sh21*].

perature form has parallel pairs of (001) NbO_2 planes coupled antiparallel to give an antiferroelectric phase, as shown in Fig. 14. The Na atoms are also displaced antiparallel to one another.

3.1.4.3 Distortions due to core polarization: Pb^{2+} and Bi^{3+}

Lead and bismuth are heavy ions, and the $6s$ orbitals are sufficiently more stable than the $6p$ orbitals that Pb^{2+} and Bi^{3+} ions are commonly stable. However, the outer $6s^2$ core electrons have a relatively large radial extension, making the ionic radius large, and this reduces the overlap of the $6p$ orbitals with the orbitals on near-neighbor anions. This reduction in overlap reduces the strength of the A-X bond. However, hybridization of $6s$ and $6p$ orbitals, which costs the energy separation of $6s$ and $6p$ orbitals, produces a polarization of the outer-core electrons, so that the effective ionic radius is much smaller on one side of the cation than on the other. This permits the formation of a much more stable bond on one side of the cation, and the energy gained in this bonding may be greater than the hybridization energy required to polarize the core. It is for this reason that Pb^{2+} and Bi^{3+} ions are stabilized in many crystals with an asymmetric anion coordination.

There are three possible displacements of the A cations that would stabilize the anion p_π orbitals (which σ-bond with the A cations): (1) *Tetragonal symmetry*. Displacement of the A cations along [001] axes to stabilize the two p_π orbitals per anion not on [001] axes, as found for **$PbTiO_3$** (see Fig. 12). (2) *Orthorhombic symmetry*. Displacement of the A cations along [110] axes to stabilize strongly one p_π orbital per anion on [001] axes and less strongly one p_π orbital per anion not on [001] axes. The smallest induced distortion of the B-cation octahedra occurs for an antiferroelectric displacement of the type illustrated by **$PbZrO_3$**, Fig. 15. (3) *Rhombohedral symmetry*. Displacement of the A cations along [111] axes to stabilize strongly one p_π orbital per anion. To be cooperative, such a distortion must be ferroelectric, as in **$BiFeO_3$**, Fig. 16. Further, since the A cation is moved toward a B cation, there is an electrostatic repulsion between them that displaces the B cation from the center of symmetry of its interstice.

Given spontaneous distortions due to A-cation displacements, there remains the possibility that electron ordering among localized d electrons on B cations can superpose an additional distortion. Whether this is the origin of the triclinic symmetry reported for ferromagnetic **$BiMnO_3$**, where Mn^{3+} is a Jahn-Teller ion, is not known.

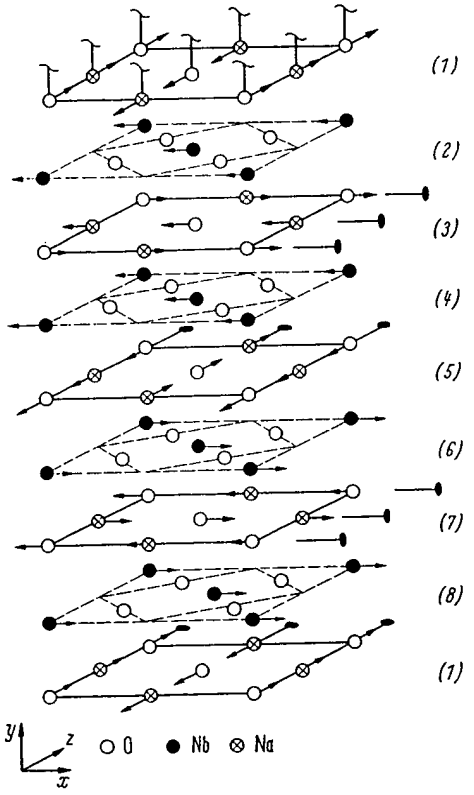

Fig. 14. Ionic displacements in orthorhombic $NaNbO_3$. The shifts of the anions in NbO_2 planes and the small x shifts of the Nb ions have been omitted for clarity [*Vo6*].

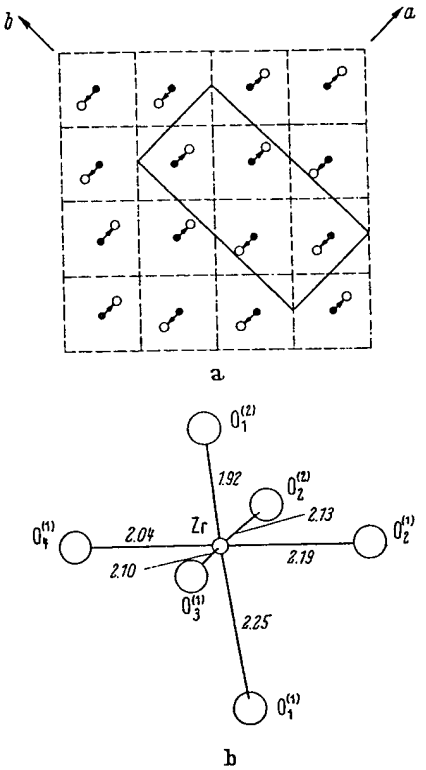

Fig. 15. a) Pb-ion shifts (≈0.26 Å) in a (001) plane of antiferroelectric $PbZrO_3$. b) Distorted Zr octahedra as a result of simultaneous anion displacements. Zr-O distances are given in [Å] [*Sa8*, *Jo5*].

3.1.4.4 Competitive phases

A few compounds have atomic radii compatible with the formation of a perovskite phase and yet are stabilized in other structures at ordinary temperature and pressure. Two important competitive structures of this type are represented by **$YAlO_3$** and **$PbRuO_3$**. Both of these compounds convert to the perovskite structure under hydrostatic pressure.

The hexagonal **$YAlO_3$** structure of Fig. 17(a) consists of close-packed layers having the sequence *b-a-b'-a-b-c-b'-c-b*, where *b* is an A-cation layer, *b'* is a B-X layer with anions stacked beneath A cations (*b* stacking) and B cations in the trigonal bipyramids formed by face-shared tetrahedra in the hexagonal *a-b-a* or *c-b-c* anion-stacking sequence. The structure apparently forms because both the A cations and the B cations simultaneously approach the lower limit for cationic size: $r_B = 0.51$ Å, $r_A = 0.90$ Å. The small Al^{3+} ion is relatively stable in the five-fold coordination of the trigonal-bipyramid sites, and the small Y^{3+} ion is more stable in an eightfold (or 6 + 2) coordination instead of a twelvefold (or 9 + 3) coordination. These site preferences reflect an increased stabilization of the bonding, anionic orbitals as a result of closer cation-anion distances.

The antiferromagnetic, ferroelectric compound **$YMnO_3$** has a similar structure, but with an *a*-axis $\sqrt{3}$ larger than that of **$YAlO_3$** to give six molecules per unit cell. The Mn^{3+} ion can be stabilized in a trigonal-bipyramid site because it has four outer *d* electrons with configuration $e_g^2 e_\pi^2 a_1^0$, where the empty a_1 orbital is directed along the *c*-axis to bond covalently with the two collinear oxygen ions. The larger unit cell and the ferroelectricity are reflected in the complex magnetic order shown in Fig. 17(b). Below Θ_N, exchange striction favors antiferromagnetic Mn-O-O-Mn interactions. The ferroelectric transition that occurs above 600 °C is apparently due to the relatively large size of the Mn^{3+} ion, which creates a large enough interstice for the Y^{3+} ion that it is stabilized by a displacement from the center of symmetry of its interstice so as to lower its near-neighbor anion coordination from eight toward seven.

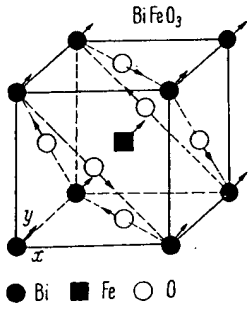

Fig. 16. Structure of $BiFeO_3$ showing displacements in perovskite subcell [*Mi0*].

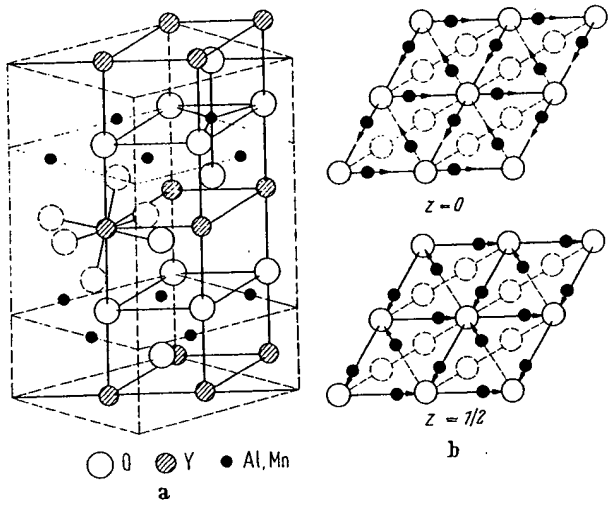

Fig. 17. a) Comparison of the unit cells of $YAlO_3$ (solid lines) and $YMnO_3$ (dashed lines). b) Magnetic structure of $YMnO_3$ [*Be36, Be39*].
$a = 3.678$ Å, $c = 10.52$ Å for $YAlO_3$.

Cubic **$PbRuO_3$** gives an x-ray pattern of the pyrochlore structure, corresponding to chemical formula $A_2B_2O_7$, and therefore may be written as **$Pb_2Ru_2O_6\oplus$**. This structure is competitive with the perovskite structure in several $PbB^{4+}O_3$ compounds. It has been shown [*Lo4*] that the anion vacancies $\oplus$ are located at the centers of Pb^{2+}-ion tetrahedra sharing common corners and that the electrostatic repulsion between the Pb ions may be counteracted by a transfer of the two outer-core electrons per Pb ion to the $\oplus$ sites, which act as traps for four electrons per vacancy. Thus the outer core electrons at the Pb^{2+} ions induce a completely new structure rather than a ferroelectric-type displacement of the A-cations within the perovskite structure. This new structure contains B cations in corner-shared octahedra, as in perovskite, but the B-X-B angle is reduced to about 135°. This structure is also stabilized in $AgSbO_3$ [*Sc22*] presumably because there is a small effective charge on the Ag^+ ions. The pyrochlore $A_2B_2O_7$ structure itself is competitive if attempts are made to force a low valence state on one of the cations.

3.1.5 Structures encountered with ordered B, B' cations

3.1.5.1 Same B atom

There are three ways of creating two different cations from the same atom:

(1) Two A cations of different valence can create two different valence states of the same B atom, and these may order at lower temperature as a result of different cationic charge. The ordering temperature may be quite low, since only electron transfers are required for cationic ordering. This is illustrated by $(La_{0.5}Ca_{0.5})$ $(Mn^{3+}_{0.5}Mn^{4+}_{0.5})O_3$, which has the Mn^{3+}, Mn^{4+} ordering in a rocksalt-type array. Because $Mn^{3+}(t_{2g}^3e_g^1)$ is a Jahn-Teller ion having localized outer d electrons, there is also a cooperative distortion to tetragonal ($c/a > 1$) symmetry of the Mn^{3+}-occupied octahedra, and the ordering of these distortions gives a macroscopic distortion to tetragonal ($c/a < 1$) symmetry (see Fig. 26).

(2) Where the energy difference between the high-spin and low-spin states of the B cation are nearly equal, the populations of the two energy states approach each other at higher temperatures. In $LaCoO_3$, high-spin Co^{3+} and low-spin Co^{III} are separated by only $E_{3+} - E_{III} \approx 0.08$ eV, and the populations of the two spin states are nearly equal at 400 °K. This temperature is sufficiently low that ordering of the two different spin states occurs above this temperature, and the symmetry changes from $R\bar{3}c$ to $R\bar{3}$ [*Ra3*]. In this case, it is the difference in ionic size and covalent bonding, which results in a difference in the effective ionic charge – not the formal ionic charge – that is the driving force for the ionic ordering.

(3) Disproportionation of B^{m+} cations into $B^{(m-1)+}$ and $B^{(m+1)+}$ cations may create ions of different size and charge that become ordered. This is illustrated by $\square PdF_3$, which has been shown by magnetic susceptibility measurements to be $Pd^{2+}Pd^{IV}F_6$ [*Ba19*]. (The A cation is missing.) Such a disproportionation permits the formation of $(PdF_6)^{2-}$ clusters in which the anionic orbitals are stabilized by strong covalent mixing with the σ-bonding $4d$ orbitals of e_g symmetry. This is accomplished by a shifting of the F^- ions toward the Pd^{4+} ions and away from the Pd^{2+} ions. Simultaneously, the anionic shift reduces covalent mixing in the occupied, antibonding $4d$ orbitals of e_g symmetry at the Pd^{2+} ions. These orbitals are therefore localized and further stabilized by intra-atomic exchange (Hund splitting), so that each Pd^{2+} ion carries an atomic moment of $2\mu_B$. Were there no disproportionation, the single electron per low-spin Pd^{III} ion would occupy antibonding e_g orbitals that were more unstable than the occupied, localized e_g orbitals at the Pd^{2+} ions. However, the transformation $2\,Pd^{III} \rightarrow Pd^{2+} + Pd^{IV}$ costs ionization energy, and this is usually too large (as in $LaNiO_3$) for disproportionation to occur.

3.1.5.2 Different B atoms

There are many examples of ordered B, B' structures in compounds having different B atoms: $A_2^+B^{+3}B'^{+3}F_6$; $A_2^{2+}B^{3+}B'^{5+}O_6$, $A_2^{2+}B^{2+}B'^{6+}O_6$, $A_2^{2+}B^{+}B'^{7+}O_6$; $A_2^{3+}B^{2+}B'^{4+}O_6$, $A_2^{3+}B^{+}B'^{5+}O_6$, and $A_3^{2+}B_2^{3+}B'^{6+}O_9$. In the $A_2BB'X_6$ group, ordering is on alternate (111) planes of B cations, in the $A_3B_2B'X_9$ group the B' cations occupy every third B-cation (111) layer, Fig. 1(c). The probability for an ordered arrangement of the B, B' cations is determined by the differences between their ionic charges and their ionic radii [*Fe22*, *Fe23*, *Ga1*, *Ga10*]. To first approximation, the order-disorder transition temperature Θ_{ord} induced by the charge difference $\Delta q = (q' - q)$ at cations B' and B is $\Theta_{ord} \sim (\Delta q)^2$. Thus superstructure has been observed in all the known compounds having $(\Delta q)^2 = 36$ and 16, whereas those having $(\Delta q)^2 = 4$ are disordered unless there is a relatively large difference in ionic sizes. The minimum difference in ionic size that results in ordered $A_2^{2+}B^{3+}B'^{5+}O_6$ compounds is $|r_B - r_{B'}|/r_B \approx 0.09$, and this has been achieved where B' = Nb or Ta, having empty d orbitals for the formation of stable $(B'O_6)^{7-}$ clusters, while the B cation has no relatively stable, empty d orbitals.

Given the formation of $(B'X_6)$ octahedra, a confusion arises as to where the structure corresponds to an ordered $A_2BB'O_6$ perovskite built up of corner-shared octahedra plus A cations and where it corresponds to the isostructural $(NH_4)_3FeF_6$ structure, which consists of discrete $(B'X_6)$ octahedra separated by A and B cations. (The cubic K_2NaAlF_6 structure with space group T_h^6(Pa3) is similar to $(NH_4)_3FeF_6$, but has a lower symmetry because there are very small rotations of the $(B'X_6)$ octahedra.) Some authors [*Fe22*] select as a criterion for the perovskite structure the cationic radius ratio $r_B/r_A < 0.8$ where $r_B > r_{B'}$. This decision is based on the observation that a plot of the cubic lattice parameter a_0 vs. B-cation radius r_B is a straight line for $r_B/r_A < 0.8$, but bends over for $r_B/r_A > 0.8$. However, this probably reflects the ratio at which electrostatic forces inhibit (or reverse) any A-cation displacements rather than the ratio at which discrete $(B'X_6)$ octahedra are formed. For most physical properties this criterion is probably arbitrary.

Without electron-ordering distortions superposed on the size effects, ordered $A_2BB'X_6$ perovskites can be described by either the O-orthorhombic cell of Fig. 5 or by the rhombohedral $R\bar{3}$ (or $R\bar{3}m$) cell of Fig. 6. Where $\alpha = 60°$, a tetramolecular cubic cell may be chosen provided the A cations are not displaced from their ideal positions. Like cubic $(NH_4)_3FeF_6$, the cubic cell has the space group O_h^5(Fm3m) with B cations in 4(b) $(\frac{1}{2}, \frac{1}{2}, \frac{1}{2})$; f.c., A cations in 8(c) $\pm$ $(\frac{1}{4}, \frac{1}{4}, \frac{1}{4})$; f.c., B' cations in 4(a) (0, 0, 0); f. c., and X-anions in 24(e) $\pm$ (u, 0, 0; 0, u, 0; 0, 0, u); f.c. with $0.2 < u < 0.25$. However, even where $\alpha = 60°$, motions of the A cations along the [111] axes may occur, thereby destroying the cubic symmetry.

If an electron-ordering transition superposes a distortion at every other octahedron of Fig. 5, either the B or the B' octahedra remaining cubic, cooperative elastic interactions between the distorted octahedra give a further reduction in symmetry. The resulting monoclinic cell [*Fi9, Bl8*], which is pseudotriclinic, is not to be confused with the pseudomonoclinic symmetry reported in early work for the O-orthorhombic structures. The origin of the superposed electron-ordering transition could be either a Jahn-Teller ordering of localized electrons or a ferroelectric-type displacement of the anions about a ($B'X_6$) octahedron.

Several $Ca_2B^{3+}Ta^{5+}O_6$ and $Sr_2B^{3+}Nb^{5+}O_6$ perovskites having B = rare-earth atom exhibit the monoclinic symmetry of a distorted O-orthorhombic cell [*Fi8*]. Since the $4f$ electrons at the rare-earth ions are localized, it is tempting to attribute this to a Jahn-Teller distortion with spin-orbit coupling. Although Fig. 9 shows that the octahedral site splitting of one-electron $4f$ orbitals gives orbitally threefold-degenerate levels having an accidental degeneracy that is not removed by spin-orbit coupling, nevertheless there are two reasons why this explanation cannot be correct: (1) There is no magnetic ordering of the $4f$ electrons at room temperature and (2) $\mathbf{Sr_2GdNbO_6}$ shows the distortion even though Gd^{3+} has a half-filled $4f^7$ shell, which has no orbital degeneracy associated with the ground state. It is therefore concluded that the additional distortions are due to the potentially ferroelectric cations Nb^{5+} and Ta^{5+}.

3.1.5.3 Complex alloys $A_2BB'X_6$, where $B = M_{13}$, $B' = M_8$

Several complex interstitial alloys have a formal structural relationship to the ordered perovskite $A_2BB'X_6$ as well as interesting magnetic properties. In this group, having space group Fm3m, the B position is occupied by a thirteen-atom cluster consisting of a metal atom at position 4(a) at the center of a cubo-octahedral, twelve-atom cluster of M atoms at positions 48(h); the B' position is occupied by a simple cube of eight M' atoms at 32(f). The three principal axes of each cluster are along the cubic axes of the perovskite cell, as shown schematically in Fig. 18, so that each X atom at positions 24(e) has eight near neighbors. The eight A atoms of the tetra-molecular cell are at the 8(c) positions. The 4(b) position at the center of the M_8' clusters is empty. Alloys with this structure include the ferromagnetic borides $Al_2[(AlM_{12})(M_8')]B_6$, where M = Fe, Co, Ni, as well as $Cr_{23}C_6$.

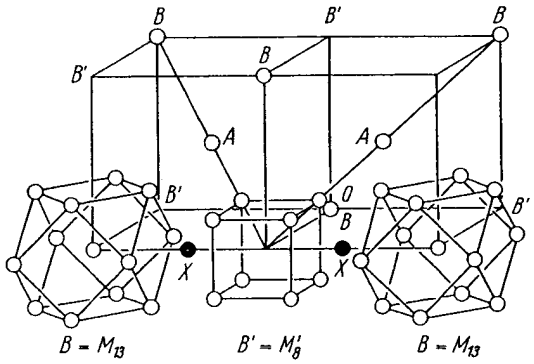

Fig. 18. One quadrant of the $A_2BB'X_6$ structure showing the atomic positions of the $B = M_{13}$ and $B' = M_8'$ clusters [*We19*].

3.1.6 First-order magnetic transition in $M^cXM_3^f$ perovskites

Many perovskites $M^cXM_3^f$ exhibit first-order phase changes at magnetic-ordering transitions. Most of these are reported to be cubic-to-cubic transitions, but in $\mathbf{ZnCMn_3}$ it is a tetragonal (ferrimagnetic)-to-cubic (ferromagnetic) transition. These crystallographic changes are induced by a complex interplay of collective electrons in overlapping bands. Because of the intimate connection with the magnetic properties and because of the necessarily speculative character of any model at this time, discussion of these compounds is deferred to 3.5.

3.1.7 Data: Crystallographic properties of ABX_3, $A_2BB'X_6$, $A_3B'_2BX_9$ and $A(B_xB'_yB''_z)X_3$ compounds with perovskite or perovskite-related structure (Tab. 2)

Tab. 2.

Within any section, the compounds are in general first ordered according to the atomic number of the B cation and then by the basicity of the A cation. For the ordered perovskites of Tab. 2b, c, d, the compounds are further ordered by the atomic number of the other B cation. The order of the sections is as follows:

Tab. 2a – ABX_3

$A^{2+}LiH_3$
$A(H_2O)(Li_{1/3})_3$; A = I^{-1}, Br^{-1}
$A^{+}B^{2+}X_3$; X = F^{-1}, Cl^{-1}, Br^{-1}
$A^{+}B^{5+}O_3$; B = V, Nb, Sb, Ta, I, Pa, U
$A^{2+}B^{4+}O_3$; B = Ti, V, Cr, Mn, Fe, Co, Ni, Ge, Zr, Mo, Tc, Ru, Sn, Ce, Pr, Hf, Re, Ir, Pb, Th, U, Np, Pu
$A^{2+}B^{4+}X_3$ or $A^{3+}B^{3+}X_3$; X = S or Se, B = Ti, Zr, Ta, In, Ga
$A^{3+}B^{3+}O_3$; B = Al, Sc, Ti, V, Cr, Mn, Fe, Co, Ni, Ga, Y, Nb, Rh, In, Ho, Er, Tm, Yb, Lu

Tab. 2b – $A_2BB'X_6$

$A_2BB^{3+}X_6$; X = F^{-1}, Cl^{-1}, B^{3+} = Al, Sc, Ti, V, Cr, Mn, Fe, Co, Ni, Cu, Ga, Ag, In, Ce, Pr, Au, Tl
$A^{2+}A^{3+}B^{3+}B^{4+}O_6$; B^{4+} = Ti, Ir
$A_2BB^{n+}O_6$; B^{4+} = Ti, Mn, Ge, Zr, Ru, Ir
B^{5+} = V, Nb, Sb, Ta, Bi, Pa, Pu
B^{6+} = Mo, Te, W, $Re^{6+,5+}$, $Os^{6+,5+}$, $U^{6+,5+}$, Np^{6+}, Pu^{6+}
B^{7+} = Tc, Re, Os, I

Tab. 2c – $A_3BB'_2O_9$

$A_3BB_2^{5+}O_9$; B^{5+} = Nb, Ru, Sb, Ta
$La_3Co_2B^{5+}O_9$; B^{5+} = Nb, Sb
$A_3B_2B^{6+}O_9$; B^{6+} = Mo, W, Re, U

Tab. 2d – $A^{2+}(B_xB'_yB''_z)O_3$

Abbreviations in Tab. 2:

Symmetry: C = cubic, H = hexagonal, M = monoclinic, O = orthorhombic ($a < c/\sqrt{2}$), O' = orthorhombic ($c/\sqrt{2} < a$), R = rhombohedral, T = tetragonal, Tr = triclinic.

Remarks: for abbreviations, see p. 131.

Tab. 2a. ABX_3 compounds

Compound	Sym	a Å	b Å	c Å	angle	Ref.	Remarks	Magnetic Data
$A^{2+}Li^{+}H_3^{-1}$								in 3.3.4, Tab.
$BaLiH_3$	C	4.023				*Me25*	P & S [*Me26*]; Neutron diffraction shows S.G. Pm3m [*Ma11a*]	
$BaLiD_3$	C	4.02				*Ma11a*	Neutron diffraction shows S.G. Pm3m [*Ma11a*]	
$SrLiH_3$	C	3.833				*Me25*	P & S [*Me26*]	
$EuLiH_3$	C	3.796				*Me24*		
$BaLiF_3$	C	3.996				*Lu1*	P & S [*Ro20, Be22a, Bu3a*]	
$A(H_2O)(Li_{1/3})_3$; A = I^{-1}, Br^{-1}								
$I(H_2O)(Li_{1/3})_3$	C	4.296				*We6*		
$Br(H_2O)(Li_{1/3})_3$	C	3.99				*Ke14*		
$A^{+}B^{2+}X_3$; X = F^{-1}, Cl^{-1}, Br^{-1}								
$CsMgF_3$	H	6.04		14.45		*Lo1b*	Hex (6L), high pressure phase	
	H	6.16		22.13		*Lo1b*	Hex (9L), high pressure phase	
	T	9.39		8.72		*Lu1*	Prep. [*Be22a, Bu3a*]	
$RbMgF_3$	M	8.19	8.19	8.19	$\beta = 98° 30'$	*Lu1*	S.S. with Co, Hex (6L), Θ_C = 15 °K (50% Co) [*Sh1a*]	
$KMgF_3$	C	3.973				*Re6*	P & S [*De22, Lu1, Be53*], I.R. spectra [*Pe5, Yo2*] NMR, F^{19} [*Al1a*], elastic properties [*Re7a*]	
$NaMgF_3$	O	5.363	5.503	7.676		*Ch5*	P & S [*Lu1, Be53, Ru8, Ba1*], NMR, F^{19} [*Al1a*]	
	T	3.942		3.933		*Ch5*	T = 760 °C, tetr. 760 < T < 900 °C	
	C	3.955				*Ch5*	T = 900 °C, cubic $T \geq$ 900 °C	
NH_4MgF_3	C	4.06				*Ch8a*	Pseudocubic	
$CsMgCl_3$	H	7.278		6.19		*Yd1*	Hex (2L)	
$KMgCl_3$	O	6.954	6.971	9.922		*Br28*	Absorption spectra: Ni [*Br28*], ESR: Mn [*Zd1*]	
$CsCaF_3$	C	4.523				*Lu1*		
$RbCaF_3$	C	4.457				*Lu1*		
$KCaF_3$	C	8.76				*Br9*	P & S [*Lu1*]	
$CsCaCl_3$	C	5.396				*Yd1*		
$CsTiCl_3$	H	7.297		6.048		*Yd1*	Hex (2L)	

Compound	Sym	a Å	b Å	c Å	angle	Ref.	Remarks	Magnetic Data
$A^+B^{2+}X_3$; X = F^{-1}, Cl^{-1}, Br^{-1} (continued)								in 3.3.4, Tab.
$CsVCl_3$	H	7.23		6.03		*Se1b*	Hex (2L), P&S [*Yd1*]	
$RbVCl_3$	H	7.04		6.0		*Gr8a*	Hex (2L), optical and magnetic properties	
$KVCl_3$	H	6.90		5.98		*Se1b*	Hex (2L), P&S [*Yd1*]	
$RbCrF_3$	T	6.149		8.088		*Vo1*	P&S [*Co27*]	
$KCrF_3$	T	6.04		8.01		*Co27*		6
	C	4.158				*Co27*	T = 500 °C, P&S [*Ed2, Vo1, Kn3, Yo1, Pe2a*]	
	T	8.544		7.968		*Sc1*	Neutron diffraction	
$NaCrF_3$	M	5.695	5.885	7.639	$\beta = 87°48'$	*Vo1*	a and b axis said to double	
$(NH_4)CrF_3$	T	6.232		7.954		*Vo1*		
$TlCrF_3$	T	6.194		8.064		*Vo1*		
$CsCrCl_3$	H	7.249		6.228		*Yd1*	Hex (2L), P&S [*Se2*]	
$RbCrCl_3$	H	7.03		6.08		*Se2*	Hex (2L) pseudohexagonal	
$CsMnF_3$	H	6.213		15.074		*Za1*	Hex (6L), Θ_N = 54 °K, P&S [*Si14, Be19*], neutron diffraction [*Pi1*], optical properties [*St28, St30*], NMR [*Mi4, We11*], AFMR [*Wi14*], magnetic properties [*Le3, Le4, Se1*], S.S. with K and Na [*Be19a*]	
	C	4.328				*Lo1b*	High pressure phase, P&S [*Sy1*]	
$RbMnF_3$	C	4.2396				*Wa8*	P&S [*Si14, Be19, Co25, Ho17*], cubic to T = 20 °K [*Te4*], dielectric properties [*Ig1, Ch4a*], compressibility [*St29*], I.R. spectra [*Ax2, Pe5*], bibliography [*Fr10a*]	6
$KMnF_3$	C	4.186				*Be3*	P&S [*Be14, Si14, Cr4, Be2, Be4, Kn3, Ok2, Ok3, Ok4, Be53, Ok6, Ho17, Gu1a*], S.S. with Co + Ni [*Ha28*], I.R. spectra [*Ax2, Pe5, Yo2*], bibliography [*Fr10a*]	6
	O	5.885	5.885	8.376		*Be3*	T = 95 °K, $(c/a > \sqrt{2})$ 184 > T > 84 °K [*Be3, De3, Ok6*]	
	O	5.900	5.900	8.330		*Be3*	T = 65 °K, $(c/a < \sqrt{2})$ T < 84 °K [*Be3, De3, Ok6*]	
$NaMnF_3$	O	5.568	5.760	8.000		*Si14*	Prep. [*Ho17, Be19b*], a and b axis doubled [*Si14*], P&S [*Ma9*]	6
$(NH_4)MnF_3$	C	4.238				*Si14*	P&S [*Cr4, Ho17, Co25*], neutron diffraction [*Pi1*]	6
$TlMnF_3$	C	4.250				*Ki9*		6
$CsMnCl_3$	H	7.288		27.44		*Ke7*	Hex (9L), Θ_N = 69 °K, AFMR [*Ke1, Sh5*]	
$RbMnCl_3$	H	7.164		17.798		*Ke7*	Hex (6L), Θ_N = 86 °K, AFMR & ESR [*Ke1, Sh3, Sh5*]	
$KMnCl_3$	T	10.024		9.972		*Cr6*	Cubic T > 458 °C, AFMR&ESR [*Ke1, Sh5*]	6

Compound	Sym	a Å	b Å	c Å	angle	Ref.	Remarks	Magnetic Data
$A^+B^{2+}X_3$; X = F^{-1}, Cl^{-1}, Br^{-1} (continued)								in 3.3.4, Tab.
$CsFeF_3$	H	6.158		14.855		*Ke19*	Hex (6L), structure [*Ba5*], $\Theta_C = 60$ °K [*Po9a, Po9b*]	
	C	4.283				*Lo1b*	High pressure phase	
$RbFeF_3$	C	4.173				*Wa12*	P&S [*Ke19*], neutron diffraction [*Wa14*], cubic $T > 97$ °K, tetr. $97 > T > 86$ °K, orth. $86 > T > 45$ °K, mon. $T < 45$ °K [*Te11*]	6
$KFeF_3$	C	4.122				*Ok6*	P&S [*Kn3, Ma29, Ok2, Ok3, Ok4*], neutron diffraction [*Sc1*]	
	R	4.108			$\alpha = 89°\ 51'$	*Ok6*	$T = 78$ °K, rhombohedral $T < 121$ °K	6
$NaFeF_3$	O	5.495	5.672	7.890		*Tr2*	P&S [*Vo1, Ma9, Po9a*]	6
NH_4FeF_3	C	4.177				*Po9a*		6
$TlFeF_3$	C	4.188				*Vo1*	P&S [*Po9a*]	6
$CsFeCl_3$	H	7.237		6.045		*Yd1*	Hex (2L), P&S [*Se2a*]	
$RbFeCl_3$	H	7.060		6.020		*Se2a*	Hex (2L)	
$CsCoF_3$	H	6.194		22.61		*Ba5*	Hex (9L), magnetic properties [*Ru6*], P&S [*Ba4*]	
	H	6.09		14.67		*Lo1b*	Hex (6L), high pressure phase	
$RbCoF_3$	C	4.116				*Ru6*	P&S [*Ru8, Cr4*], S.S. with Mg [*Sh1a*]	6
$KCoF_3$	C	4.069				*Ok6*	P&S [*Kn3, Ma29, Ok2, Ok3, Ok4, Ru8, Cr4*] I.R. spectra [*Ax1, Ax2, Pe5, Yo2, Pe2a*]	6
	T	4.057		4.049		*Ok6*	$T = 78$ °K	
$NaCoF_3$	O	5.420	5.603	7.792		*Ru6*	P&S [*Ru8, Og2, Tu5, Ma10*]	6
NH_4CoF_3	C	4.127				*Ru6*	P&S [*Cr4, Ru8*]	6
$TlCoF_3$	C	4.138				*Ru6*	P&S [*Ru8*]	6
$CsCoCl_3$	H	7.202		6.032		*Yd1*	Hex (2L), complete structure and magnetic properties [*So1*]	
$RbCoCl_3$	H	6.996		5.996		*En1*	Hex (2L)	
$CsNiF_3$	H	6.236		5.225		*Ba2*	Hex (2L)	
	H	6.15		22.32		*Lo1b*	Hex (9L), high pressure phase	
	H	6.05		14.54		*Lo1b*	Hex (6L) high pressure form: $\Theta_C = 111$ °K	
$RbNiF_3$	H	5.843		14.31		*Ru5*	Hex (6L), P&S [*Si14*], $\Theta_C = 139$ °K, magnetic properties [*St19b, Mc1a, Sm32, Sm31, Sh1, Go3, Ku2, Go3a*], S.S. with Co [*Bo13, Su11, Pi16*], optical properties [*Sm32, Sm31, Sm21, Sm22, Sh1, Ty1, Pi8, Pi14, Pi15, Za1a, Be19c, Pi16*], Raman scattering [*Ch14a*], NMR [*Sm32a*]	
	C	4.074				*Ka4*	High pressure phase, P&S [*Sy1*]	6
$KNiF_3$	C	4.015				*Ok6*	P&S [*Ok3, Ok4, Kn3, Ma10, Ru5, Ok2*], I.R. spectra [*Pe5, Ba17a*]	6
	C	4.002				*Ok6*	$T = 78$ °K	

Compound	Sym	a Å	b Å	c Å	angle	Ref.	Remarks	Magnetic Data
$A^+B^{2+}X_3$; X = F^{-1}, Cl^{-1}, Br^{-1} (continued)								in 3.3.4, Tab.
$NaNiF_3$	O	5.360	5.524	7.688		*Ru8*	P&S [*Og2, Ru5, Ok5*]	6
NH_4NiF_3	C	8.145				*Ru5*	P&S [*Ru8*]	6
$TlNiF_3$	H	5.87		14.37		*Ko4*	Hex (6L)	
	C	4.10				*Ko4*	High pressure phase, P&S [*Sy1*]	
$CsNiCl_3$	H	7.169		5.940		*Yd1*	Hex (2L), P&S [*As4*], structure determination [*Ti4*]	
$(CH_3)_4NNiCl_3$	H	9.019		6.109		*St44*	Hex (2L)	
$CsNiBr_3$	H	7.488		12.480		*As4*	Related to Hex (2L)	
$CsCuF_3$	H	12.55		11.56		*Ba2*	Related to Hex (2L), optical properties [*Sc10a*]	
$RbCuF_3$	T	6.001		7.894		*Ru6*	Optical properties [*Sc10a*]	6
$KCuF_3$	T	5.855		7.846		*Ru6*	P&S [*Ed2, Kn3, Ok1, Ok2, Ok6,*] neutron diffraction [*Sc1*], optical properties [*Pe2a, Oe1, Sc10a*]	6
	T	4.121		3.913		*Ok6*	T = 78 °K	
$NaCuF_3$	M	11.01	11.37	7.521	β = 86° 54'	*Ru6*	P&S [*Ru3*]	6
NH_4CuF_3	T	6.09		7.78		*Cr4*		
$TlCuF_3$	T	6.083		7.866		*Ru6*	P&S [*Ru3*]	6
$CsCuCl_3$	H	7.20		18.00		*Yd1*	Related to Hex (2L), P&S [*Sc7, We9*] magnetic properties Θ_p = −3.5 °K, μ_{eff} (300 °K) = 1.95 μ_B [*Ri8c, Fi2*]	
$KCuCl_3$	M	4.029	13.785	8.736	β = 97° 20'	*Ki10*	Not perovskite, magnetic properties Θ_N = 17.5 °K [*Ma1, Sh5*]	
NH_4CuCl_3	M	4.066	14.189	9.003	β = 97° 30'	*Ki10*	Not perovskite	
$KCuBr_3$	M	4.05	14.43	9.30	β = 96° 5'	*Ki10*	Not perovskite, magnetic properties [*In3*]	
$CsZnF_3$	T	9.90		9.05		*Lu1*		
	H	6.09		14.67		*Lo1b*	Hex (6L), high pressure phase	
$RbZnF_3$	C	4.110				*Ba1*	P&S [*Cr4, Lu1*]	
	H	5.896		14.44		*Ba1*	Hex (6L) high temperature form	
$KZnF_3$	C	4.055				*Kn3*	P&S [*Lu1, Ma29*], thermal conductivity [*Su8*], optical properties: Ni, Mn [*Fe11, Fe15*], I.R. spectra [*Yo2, Pe2a*]	
$NaZnF_3$	O	5.404	5.569	7.743		*Tu5*	P&S [*Lu1, Ru8, Ba1, Ma9, Ma10, Sc10*]	
NH_4ZnF_3	C	4.115				*Cr4*		
$AgZnF_3$	C	3.98				*De22*		
$TlZnF_3$	H	5.934		14.52		*Vo1*	Hex (6L)	
$CsGeCl_3$	R	5.444			α = 89° 38'	*Ch15*	Nuclear quadrupole resonance [*Vo0*]	
	C	5.475				*Ch15*	Cubic T > 155 °C, ferroelectric transition at 155°C	

	C	5.475				*Ch15*	Cubic $T > 155$ °C, ferroelectric transition at 155°C	

Compound	Sym	*a* Å	*b* Å	*c* Å	angle	Ref.	Remarks	Magnetic Data
$A^+B^{2+}X_3$; X = F^{-1}, Cl^{-1}, Br^{-1} (continued)								in 3.3.4, Tab.
$CsSrF_3$						*Yd1*	[*Be22a, Bu3a*] no cell dimensions	
$CsSrCl_3$	C	5.589						
$CsPdF_3$							Prep. + Prop. [*Ba20, Fi3*]	
$CsCdF_3$	C	4.47				*Kl1*	P & S [*Co27a*]	
$RbCdF_3$	C	4.395				*Vo1*	Mn emission [*Kl1*], P & S [*Co27a*]	
$KCdF_3$	T	6.101		8.652		*Ba5b*	P & S [*Ma29, Br9, Kl1, Co27a, Co26, Vo1*], Mn emission [*Kl1*]	
$(NH_4)CdF_3$	T	4.368		4.447		*Co27a*		
$TlCdF_3$	C	4.400				*Co27a*	T_{melt} = 765 °C	
$CsCdCl_3$	C	5.20				*Fe20*	Slight distortion [*Na15*], P & S [*Si3*]	
	H	7.418		18.39		*Si3*	Hex (6 L)	
$CsCdBr_3$	C	10.70				*Na15*	P & S [*Na19*]	
$CsSnCl_3$	C	5.58				*Do5*		
$CsSnBr_3$	C	5.94				*Do5*		
$CsEuF_3$	C	4.77				*Bo31*		6
$CsHgCl_3$	C	10.88				*Na15*	P & S [*Na19, Na18*]	
$CsHgBr_3$	C	5.77				*Na15*	P & S [*Na19*]	
$CsPbF_3$	C	4.81				*Sc9*		
$CsPbCl_3$	T	5.590		5.630		*Mo2*	Phase transition at 40 °C [*Sa2a*]	
	C	5.599				*Mo2*	Cubic $T > 47$ °C [*Mo3*]	
$CsPbBr_3$	C	5.874				*Mo2*		
$A^+B^{5+}O_3$								
AVO_3							Not perovskite, A = Na, K, Rb, Cs and Ag	
$RbNbO_3$						*Fe7*	Not perovskite	
$KNbO_3$	O	5.720	5.739	3.984		*Wo15*	Structure [*Ka19, Vo4, Vo5*], crystal growth [*Bu2, Sh25*], optical properties [*Ka8, Ch13*]; S.S. with: $BaTiO_3$ [*Br2*], $NaNbO_3$ [*Du3, Te8c*], Li [*Ni2a*]	
	T	4.00		4.07		*Wo15*	T = 260 °C, Tetr. 435 > T > 225 °C, S.S. with $KTaO_3$ (see $KTaO_3$)	
	C	4.024				*Wo15*	T = 500 °C, cubic $T > 435$ °C	
	R	4.016			$\alpha = 89° 50'$	*Sh23*	$T = -140$ °C, neutron diffraction	
$NaNbO_{2.5}$	C	4.2				*Ad1*	$2Na + Nb_2O_5$	

Compound	Sym	a Å	b Å	c Å	angle	Ref.	Remarks	Magnetic Data
$A^+B^{5+}O_3$ (continued)								in 3.3.4, Tab.
$NaNbO_3$	O	5.505	5.568	15.518		*Vo6*	Structure determined, P&S [*Vo4, Vo5, We10, Ba18, Fe7, Wo15*]; S.S. with: $KNbO_3$ [*Du3, Te8c*], $NaTaO_3$ [*Iw4, Is7, Is14*], $SrNb_2O_6$ [*Is16, Te7*], $CdTiO_3$ [*Le2*], $AgNbO_3$ [*Br24*], Cd and Sr [*Te8b*]	
$NaNbO_3$	O	5.51	5.57	7.77		*Wo17*	50 kV/cm applied to crystal; other phase transformations [*Te6, So1b, Le5, Fr1, Sh20a, Cr6a, So1a, Is5a*]; heat of transformations [*Te8a*]	
$Na_{0.975}K_{0.025}NbO_3$	O	5.528	5.582	7.782		*We10*	Structure determined	
$LiNbO_3$	H	5.1483		13.8631		*Ab4*	Not perovskite, see text	
$AgNbO_3$	M	7.888	7.888	15.660	$\beta = 90° 34'$	*Fr2*	S.S. with $KNbO_3$ [*We5*]	
	C	3.595				*Fr2*	$T = 550$ °C, cubic $T > 550$ °C	
$AgSbO_3$	C	10.32				*Sc22*	Defect pyrochlore	
$RbTaO_3$	T	3.92		4.51		*Sm11*	[*Fe7*] says not perovskite	
$KTaO_3$	C	3.9885				*Vo4*	P&S [*Vo5*], crystal growth [*Sh25, Wi4, We13*], optical properties [*Fr20, Pr2, Di7, Di8, Be27, Ax1, Pe4, Jo15, Sh20, Ka7, Sc5, St20, La7a*], Faraday rotation [*Ba7*], electrooptic properties [*Fr20, Fa7, Fa8, Fr21, Fr22, Ge13, Zo3*], S.S. with: $KNbO_3$ [*Fu3, Ha2, Ch13, Ge9, We12, We14, Di6, Hi2a, La7a*], Ca [*Se4*]; Raman spectrum [*Fl1a, Pe6, Fl1b*]; ESR: Eu, Gd [*Un1*], Fe, Ni [*Ha9a, We18b*]; ultrasonic attenuation [*Ba17b*]; Nuclear spin resonance [*Gr7a*]	
$NaTaO_3$	O	5.494	5.513	7.751		*Ka22*	Crystal structure, P&S [*Vo4, Vo5*], S.S. with: $NaNbO_3$ [*Is14, Is7*]	
$NaTaO_3$	C	3.929				*Is5*	630 °C, cubic $T \geq 630$ °C, tetr. $630 > T > 550$ °C	
$LiTaO_3$	H	5.154		13.783		*Ab2*	Not perovskite, neutron diffraction [*Ab3*] (see text)	
$CuTaO_3$						*Sh12*	Actually $Cu_{0.5}$ TaO_3, see "Bronze" section	
$AgTaO_3$	M	7.862	7.862	3.914	$\beta = 90° 21'$	*Fr2*	P&S [*Br27*]	
	C	3.949				*Fr2*	485 °C; cubic $T > 485°$	
$CsIO_3$	C	4.674				*Bo30*	P&S [*Na15*]	
$RbIO_3$	R	4.541			$\alpha = 89° 44'$	*Bo30*	P&S [*Na15*]	
KIO_3	M	8.94	8.94	8.94	$\beta = 89° 12'$	*Na16*	Perovskite (?), P&S [*Na15*]	
	R	4.410			$\alpha = 89° 25'$	*Sm3*	P&S [*Ri9*]	
$TlIO_3$	R	4.510			$\alpha = 89° 20'$	*Sm3*		
NH_4IO_3	C	9.18				*Na15*		
$CsPaO_3$	C	4.368				*Ke5*		

Compound	Sym	a Å	b Å	c Å	angle	Ref.	Remarks	Magnetic Data
$A^+B^{5+}O_3$ (continued)								in 3.3.4, Tab.
$KPaO_3$	C	4.341				*Ke5*		
$NaPaO_3$	O	5.82	5.97	8.36		*Ke5*		
$RbUO_3$	C	4.323				*Ke12*	P&S [*Ru3a, Ip1*], Prop. [*Ke13*]	6
KUO_3	C	4.290				*Ke12*	P&S [*Ru3a, Ch1b*], Prop. [*Ke13*]	6
$NaUO_3$	O	5.775	5.905	8.25		*Ke12*	P&S [*Ru3a*], Prop. [*Ke13*]	6
$A^{2+}B^{4+}O_3$								
$BaTiO_3$	C	4.012				*Me1*	T = 200 °C, cubic 120 < T < 1372 °C [*Ed5*], cubic T > 133 °C [*We11a*], high temperature phase [*Me4, Me6, Me2, Ka23*]	
	T	3.994		4.034		*Me1*	T = 20 °C, tetragonal 5 < T < 120 °C; structure determination: by x-rays [*Ev2, Ev3, Ev4, Ch2*], by neutrons [*Sh18, Fr4*], by electron microscope [*Pl2*]; P&S [*De1, Sa5*], further remarks: *)	
	O	5.682	5.669	3.990		*Vo5*	T = −10° C, orthorhombic −90 < T < 5 °C [*Ka24*]	
	R	3.998			α = 89° 52'	*Ka24*	T = −100 °C, rhombohedral T < −90 °C	
	H	5.735		14.05		*Bu4*	Hex (6L); structure determination [*Bu4, Ev1*]. Further remarks:**)	
$SrTiO_3$	C	3.905				*Me4*	T = 293 °K; cubic T > 110 °K, thermal expansion $\alpha = 9.4 \cdot 10^{-6}$ Å/deg., may be tetr. with c/a = 1.00008 [*Ly2*]	
	T	3.8972		3.8991		*Ly2*	T = 100 °K, Tetr. 65 < T < 110 °K, c/a = 1.00056, on single crystal [*Ly2*]. Further remarks:***) See page 156	
	O					*Ly2*	$a:b:c$ 0.9998:1:1.0002, orthorhombic 35 < T < 65 °K [*Ly2*]	
	R					*Ly2*	Possibly rhombohedral at 10°K	

*) Complete bibliography to 1961 [*Ha7*]; Raman scattering [*Di8, Dv2, Pa6, Pi3, Ri8, Di8a, Ro19a*]; study of structural changes [*Ca4, Co15a, Fo6, Me6, Sc8, Ka24, We11a*]; pressure dependence of dielectric properties [*Go27, Ka1, Le9, Me23, Mo7, Mo8, Po3, Po4, Po5, Po6, Sa3*]; radiation damage [*Sc6, We3*]; refractive index [*Sh31, Ho3, Ho3a*]; thermal conductivity [*Di9, Ma23, Su7, In2b*]; surface layers [*Or1, Le12, Ho10, Du1, Cr2, Ca1, Br3*]. Optical properties [*Mu11, Mu12, Mu13, Ve8, Ve6, Ha15, Jo1, Co30, Sh24, Re4, Po7, Na8, Kh3, Ba9, We11a*]; ultrasonic propagation [*Gr10*]; ESR: Ti [*Da4, Ta4, Ta6*], Mn [*Ik1, Ik2, Ik3, Ve10*], Pt [*Si3*], Eu [*Ta7, Ta8*], Gd [*Bu7, Ta3, Ta5, Ta8, Ri5*]; dielectric properties [*De9, Hu11, St17, Fr17, We11a*]. Transport properties [*Uc1, Ue2, Ta9, Sc15, Ry1, Mu10, Ma32, Ma3, Ko9, Ka21, Ik5, Be28, An4*], electromicroscopic observation [*Mo12*]. Lattice vibration [*Ax1, Ha14, Ka3, Dr3*], shock-wave compression [*Do4*], elastic properties [*Fu5*], grain size influence on Θ_C [*Ri2*], relaxation time [*Wi5, Bo4*]. Properties with additives: Mg [*Is13*], Mn [*Bh1, As2*], Fe [*Sc25*], Co, Ni [*Ku1, Co23a*], Zn [*Si16*], Nb + Ta [*Gu1, Ku1*], Ln [*Go4, As2, Bo4, Jo11*], Sr [*He14, Al1, He6*], Bi [*Bo3, Jo11*], Sb [*He13, Jo11*], Halogens [*Jo10*], $PbNb_2O_6$ [*Sr1*], Ca, Zr, Si, Fe, Mg [*Br22a*]; defect study [*Co24, Mu9, No8*], neutron scattering [*Ya2a*].

**) P&S [*Wo16, Me4, Ma36, St19c, Ra5, Bl14a, Di4*]; effect of additives on occurrence [*Ra5, Ro20a, Di4*], hex. form due to oxygen vacancies or metal substitution for Ti [*Di4*], magnetic properties with Ti, Cr, V, Mn, Re, Fe, Co, Ru, Ir, Pt substitution [*Di4*].

Compound	Sym	a Å	b Å	c Å	angle	Ref.	Remarks	Magnetic Data
$A^{2+}B^{4+}O_3$ (continued)								in 3.3.4, Tab.
$CaTiO_3$	O	5.381	5.443	7.645		*Pe3*	P&S [*Ba18, Ze1, Ze2, Le10, Na13, Na15, Me4, Ku3*], optical properties [*St21, Pe8, Mu13*], detailed structure [*Ka21a*]	
	C					*Gr3a*	Cubic $T > 1260$ °C	
$CdTiO_3$	O	5.348	5.417	7.615		*Ka22*	Structure determined $Pbn2_1$ [*Ka22*], structure questioned [*Ge3a*], P&S [*Me4*], S.S. with $NaNbO_3$ [*Le2*], electrical properties [*Sh24a*], perovskite-ilmenite transformation [*Li0*]	
$PbTiO_3$	T	3.904		4.152		*Sh21*	Complete structure [*Sh21*], P&S [*Me4, Sh19, Co13, Sh15, Sh24b*], optical properties [*Pe8, Fu5*], piezoelectric properties [*Ue3, Fe2, Fe1, Is14a*], slow neutron scattering [*So2*], S.S. with (Ba, Sr, Ca, Pb) (Ti, Zr, Sn)O_3 [*Sh19, Ta14, Ha20, Ba12, No7, Ou1, Ou2, Th2, Ok7, Ta6, Kl7, Ou1a, Pe9, Is1, Uc2, St34, Fe1, Bu10, Fe3, Fe9, Fu5, He14, Iw3, St35, Di1a*], radiation damage [*Ha30*], S.S. with $PbGeO_3$ [*Di5b*]	
	C	3.960				*Sh21*	$T = 535$ °C, cubic $T > 490$ °C	
$(CuA)TiO_3$	C	≈ 7.4				*De18*	A = Ca (25%) $a = 7.393$ Å; Cd (25%) $a = 7.399$ Å; Sr (20%) $a = 7.420$ Å	
$EuTiO_3$	C	7.810				*Ho12*	P&S [*Br20, Mc1b*], Prop. [*Mc2, Mc3, Mc4, Si4*]	6
$La_{0.5}K_{0.5}TiO_3$	C	3.914				*Ro20*	Dielectric properties [*Sm8, Ag1*]	
$La_{0.5}Na_{0.5}TiO_3$	C	3.86				*Ag1*	Dielectric properties [*Sm8*]	
$Ce_{0.5}K_{0.5}TiO_3$	C	3.90				*Ro20*	S.S. with La	
$Nd_{0.5}K_{0.5}TiO_3$	C	3.874				*Ro20*		
$Y_{0.5}Na_{0.5}TiO_3$	O	5.326	5.443	7.614		*Re2*		
$Bi_{0.5}K_{0.5}TiO_3$	T	3.913		3.993		*Iv2*	Dielectric properties [*Ag1, Bu3, Sm8, Sm26*]	
$Bi_{0.5}Na_{0.5}TiO_3$	R	3.891			$\alpha = 89° 36'$	*Iv2*	Dielectric properties [*Ag1, Bu3, Sm8, Sm26*]	
$La_{2/3}TiO_3$	C	3.887				*Ke18*	S.S. with $SrTiO_3$ [*Ti1, Ve9, We16*]	
$SrVO_{2.5}$	C	3.848				*Ke18*		
$SrVO_{3.0}$	C	3.838				*Wo14*	P&S [*Re8*]	6

***) Superconductivity [*Am2, Ap2, Ea2, Fr10, Ko7, Sc19, Sc20, Sc21*]; Raman scattering [*Sc4, Sc3, Ri6, Os1, Ni1a, Fl1b*]; NMR [*We1*]; Mössbauer: Co^{57} [*Bh3*]. Optical properties [*Ba6, Ba15, Ba16, Ca6, Co9, Dv1, Ea1, Gr1, Ka9, Mu11, Mu12, Mu13, Si12, Va6, Zo2, Am3, Fa4a, Fe10a*]; Hall mobility [*Fr6, Fr9, Pa5, Tu1*]; ESR: Cr^{3+} [*Ri7*], Fe^{3+} [*Ki2, Ba8, Ri7, Un2*], Ni^{3+} [*Ho1*], Gd^{3+} [*Ri7, Ri5, Sa2, Si11*]; magnetoresistance [*Fr7, Tu3, Ya3b*], piezoelectric properties [*Tu2*]; Shubnikov-deHaas effect [*Fr8*]; thermal conductivity ($33 < T < 110$ °K) [*Su7*]; diffusion and formation of oxygen defects [*Pa3, Pa4, Wa9, Wa10*]; radiation damage [*Sc6, Ro4*]; band structure [*Ka6*]; dielectric properties: doped with Fe and Cr [*Ma33*] with Nb [*Ti2*]; elastic constants from sound wave attenuation [*Be6, Jo5a*]; electromechanical behavior [*Ru12*]; pressure dependence of dielectric properties [*He6a, Sa3*]; photoconduction [*Ya4, Ya5, Ya3a, Ya3b*]; magnetic properties [*Fr5*]; vibrational modes [*Ja8, Jo14*]; thermal expansion [*De19b*], inelastic neutron scattering [*Sh16a*], electrooptic effect [*So3*].

Ya3b]; magnetic properties [Fr5]; vibrational modes [Ja8, Jo14]; thermal expansion [De19b], inelastic neutron scattering [Sh16a], electrooptic effect [So3].

Compound	Sym	a Å	b Å	c Å	angle	Ref.	Remarks	Magnetic Data
$A^{2+}B^{4+}O_3$ (continued)								in 3.3.4, Tab.
$CaVO_{3.0}$	C	3.767				*Wo14*	P&S [*Ru7, De2, Re8, Re9*]	6
	O	5.326	5.352	7.547		*Ro16*		
	C	3.780				*Wo14*		
$CaVO_{2.85}$	H	5.62		22.95		*Ch1a*	Hex (9L), high pressure phase, semiconducting, $\Delta E = 0.09$ eV	
$BaCrO_3$	H	5.659		9.359		*Ch1a*	Hex (4L), high pressure phase, semiconducting, $\Delta E = 0.11$ eV	
	H	5.627		13.690		*Ch1a*	Hex (6L), high pressure phase	
	H	5.662		27.752		*Ch1a*	Hex (12L), high pressure phase	
	H	5.652		32.515		*Ch1a*	Hex (14L), high pressure phase	
	H	5.649		62.706		*Ch1a*	Hex (27L), high pressure phase	
$SrCrO_3$	C	3.818				*Ch1*		6
$CaCrO_3$	O	5.287	5.316	7.486		*Go17*		6
$PbCrO_3$	C	4.00				*Ro19*	P&S [*De21*]	6
$BaMnO_3$	H	5.672		4.71		*Ha7*	Hex (2L), P&S [*Ha16, Sy1*]	
	H	5.667		20.948		*Sy1*	Hex (9L), high pressure phase	
	H	5.669		9.375		*Ha7*	Hex (4L), high pressure phase, P&S [*Ha16*]	
	H	5.645		9.264		*Sy1*	Hex (4L), high temperature phase	
$SrMnO_3$	H	5.449		9.085		*Sy1*	Hex (4L), S.S. with (Bi, Ba, La)MnO_3 [*Iv1*]	
	H	5.431		13.396		*Sy1*	Hex (6L), high pressure phase	
$CaMnO_3$	O	5.270	5.275	7.464		*Ma6*	96% Mn^{4+}, P&S [*Vo12, To13, Yu1, Yu8*], S. S. with Bi [*Bo6, Bo12, St19*]	6
$Ca_{0.75}Sr_{0.25}MnO_3$	O	5.302	5.304	7.488		*Ma6*		6
$BaFeO_{3-x}$	R	4.099			$\alpha = 88°\,47'$	*Mo10*	$x = 0.36$ P&S [*De15, Er1, Mo11, Ma22, Va8*]	6
	C	3.997				*Mo10*	$x = 0.25$; K_β X-ray spectra [*Ko6a*]	
	T	7.956		8.006		*Mo10*	$x = 0.19$	
	H	5.672		13.90		*Mo10*	Hex (6L); $x = 0.08$	
$BaFeO_{2.5}$	O	5.83	16.98	5.54		*Ga18*	Brownmillerite structure, see Fig. 21	
	C	4.15				*Mo11*	$T = 1000$ °C, $T = 20$ °C (triclinic)	
$SrFeO_{3.0}$	C	3.850				*Ma4*	P&S [*Wa17, Ya1, Ga17, Sh17*], S.S. with La [*Ga16, Wa17, Wa20*], Bi [*Ma8*], Ti [*Cl2, Br18*]	6
$SrFeO_{2.84}$	T	3.851		3.867		*Ma4*		
$SrFeO_{2.50}$	O	5.671	15.59	5.528		*Ma4*	P&S [*Ba23*], S.S. with Al [*Ba24, Ba25*], Brownmillerite structure, see Fig. 21	
$CaFeO_{2.50}$	O	5.64	14.68	5.39		*Be40*	P&S [*Be39, Sm4*], neutron diffraction [*Ta10, Fr16, Co22*], Mössbauer [*Go4, Gr6, Ge7, Ge8, Wi15, Wi16, Ta10, Gr4*]	6
$CaFe_{0.5}Al_{0.5}O_{2.5}$	O	5.58	14.50	5.34		*Ha10*	Prop. [*Gr5, Po1, Wh4, Be40, Sm4*]	6
$PbFeO_{2.5}$	T	7.79		15.85		*Be26*	P&S [*Mo15*]	6

Compound	Sym	a Å	b Å	c Å	angle	Ref.	Remarks	Magnetic Data
$A^{2+}B^{4+}O_3$ (continued)								in 3.3.4, Tab.
$BaCoO_{2.72}$	H	5.59		4.83		*Gu7*	Hex (2L), P&S [*St41*]	
$SrCoO_{3-x}$	C	7.725				*Ya1*	1.4% Co^{4+}, S.S. with La [*Wa17*]	
$BaNiO_{2.8}$	H	5.58		4.832		*La4*	Hex (2L) [*La3, Gu7*]	
$CaGeO_3$	C	3.723				*Ri8a*	High pressure phase; doubled cell [*Sl3a*]	
$CdGeO_3$	C	3.70				*Ri8a*	High pressure phase, pseudocubic	
$BaZrO_3$	C	4.20				*Ha20*	P&S [*Ho2, Me4, Be24*]; S.S. with $BaTiO_3$ [*Ve7*], $PbTiO_3$ [*Ha20*]; optical properties [*Pe7, Du5*]	
	C	4.26				*Fo4*	$T = 2000$ °C	
$SrZrO_3$	O	5.792	5.818	8.189		*Pe3*	P&S [*Ho2, Me4, Sm3, Sc18a*], D.T.A., $T < 1000$ °C [*Ca5*], optical properties [*Pe7, Du5*], S.S. with Hf [*Be24a*]	
	C	4.18				*Fo4*	$T = 2000$ °C, cubic $T > 1300$ °C	
$CaZrO_3$	O	5.587	5.758	8.008		*Ti3*	P&S [*Si15, Me4, Ru9, Ru14*], S. S. with Cr [*Ni2*]	
	C	4.10				*Fo4*	$T = 2000$ °C, cubic $T > 1600$ °C	
$PbZrO_3$	O	5.872	11.744	8.202		*Sa8*	P&S [*Is1, Me4, Sa7*], phase transitions [*Go28, Go29, Go30, Sa8, Te5, Te8, Ue1, Sh15a, Te8d*], radiation damage [*Ha30*], optical properties [*Pe7*], neutron diffraction [*Jo5*], dielectric properties [*Kh4, Kh6, Kh8, Go29*], piezo-electric effect [*Ro1, Th2, Is14a*], S.S. with Ca [*Kh4, Si15*], (BiNa) and (BiK) [*Bu3*], $Pb(Ni_{1/3}Nb_{2/3})O_3$ [*Bu10*], $BiFeO_3$ [*Ge10*], Hf [*Go31*]	
	C	4.149				*Sa8*	$T = 230$ °C, cubic $T > 230$ °C	
$EuZrO_3$	C	4.099				*Ho12*	P&S [*Mc4*]	6
$Bi_{0.5}K_{0.5}ZrO_3$							Prep. + Prop. [*Sm33, Bu3*]	
$Bi_{0.5}Na_{0.5}ZrO_3$							Prep. + Prop. [*Sm33, Bu3*]	
$BaMoO_3$	C	4.04				*Sc17*	P&S [*Bo19, Sc16, Ro2a*], S.S. with Sr [*Br15*]	6
$SrMoO_3$	C	3.98				*Sc17*	P&S [*Bo19, Sc16, Ro2a*], S.S. with Ti [*Ro2a, Br17*], S.S. with Zr [*Br17*]	6
$CaMoO_3$	O	5.45	5.58	7.77		*Mc1*	P&S [*Sc16, Go17, Ro2a*]	6
$BaTcO_3$	H	5.758		14.046		*Mu7*	Hex (6L)	
	C	8.140				*Ke9*		
$SrTcO_3$	C	3.95				*Mu7*	Slight distortion, P&S [*Ke9*]	
$CaTcO_3$	O	3.87	3.96	3.76		*Ke9*		
$PbTcO_3$	C	10.360				*Mu7*	Defect pyrochlore structure	
$BaRuO_3$	H	5.75		21.60		*Ra6*	Hex (9L), structure determination [*Do2*], Prop. [*Ca2*], S.S. with Sr [*Do3, Lo1*], S.S. with Zr, Mn, Ir, Ni [*Do3a*]	
	H	5.73		9.50		*Lo1*	Hex (4L), high pressure phase	

Compound | Sym | a | b | c | angle | Ref. | Remarks | Magnetic | Ref.

Compound	Sym	a Å	b Å	c Å	angle	Ref.	Remarks	Magnetic Data
								in 3.3.4, Tab.
$A^{2+}B^{4+}O_3$ (continued)								
	H					*Lo1*	IT, Ni [*Do3a*]	
	H	5.73		9.50		*Lo1*	Hex (4L), high pressure phase	
$BaRuO_3$	H	5.71		14.00		*Lo1*	Hex (6L), high pressure phase	
$SrRuO_3$	O	5.53	5.57	7.85		*Ra6*	P&S [*Kh1*], Prop. [*Ca2, Lo3*]	6
$CaRuO_3$	O	5.36	5.53	7.67		*Ra6*	Prop. [*Ca2, Lo3*]	6
$SrRu_{0.5}Ir_{0.5}O_3$	O	5.55	5.58	7.84		*Ra6*		
$PbRuO_3$	C	10.25				*Lo4*	P&S [*Ra6*], Defect pyrochlore structure	
	O	5.56	5.61	7.86		*Lo1a*	High pressure phase	
$BaSnO_3$	C	4.117				*Me4*	P&S [*Wa2, Co8, Sm3*], S.S. with Sr [*Sm3*], (Ba, Sr, Pb)TiO_3 [*Na9, Du4, My2*], optical properties [*Du5, Ya3*], Mössbauer in S.S. with Ti [*Be7, Bo9, Kr6*]; S.S. with Ti, tetragonal at 91% Ti [*Do1*]	
$SrSnO_3$	C	8.070				*Sm3*	P&S [*Ho2, Me4, Co8*], optical properties [*Du5*]	
$CaSnO_3$	O	5.519	5.668	7.885		*Sm2*	P&S [*Ro12, Co8, Me4*]; optical properties [*Du5*]; S.S. with $BaTiO_3$ cubic at 13% $CaSnO_3$ [*Do1*]	
$CdSnO_3$	O	5.457	5.577	7.867		*Sm2*	P&S [*Na13, Co8*]	
$PbSnO_3$	M	4.076	4.076	4.043	$\beta = 89° 45'$	*Su9*	High pressure preparation	
	C	4.07				*Su9*	$T = 125$ °C, cubic $T > 125$ °C	
$BaCeO_3$	C	4.397				*Sm3*	P&S [*Ho2*], optical properties [*Du5*], S.S. with Sr [*Sm3*], dielectric properties [*Sm7a*]	
$SrCeO_3$	O	6.011	6.156	8.588		*Sm3*	P&S [*Ho2*], optical properties [*Du5*], dielectric properties [*Sm7a*]	
$CaCeO_3$	C	7.70				*Na14*	Pseudocubic	
$CdCeO_3$	C	7.65				*Na14*	Pseudocubic	
$PbCeO_3$	C	7.62				*Na14*	Pseudocubic	
$BaPrO_3$	C	8.708				*Na15*	P&S [*Ho2*]	
$BaHfO_3$	C	4.172				*Sh16*	S.S. with $CaZrO_3$ [*Be24*], P&S [*Sc18a*]	
$SrHfO_3$	C	4.069				*Ho2*	P&S [*Na15*], S.S. with $SrZrO_3$ [*Be24a*]	
$CaHfO_3$	O	5.568	5.732	7.984		*De7*	Prep. [*Ru14*]	
$CdHfO_3$	M	3.942	3.982	3.942	$\beta = 91° 36'$	*Av1*		
$PbHfO_3$	T	4.136		4.099		*Sh16*	Cubic $T > 215$ °C, S.S. with $PbZrO_3$ [*Go31*]	
	C	4.134				*Sh16*	$T = 250$ °C, cubic $T > 215$ °C	
$PbReO_3$	C	10.425				*Lo4*	Defect pyrochlore type	
$BaIrO_3$	H	5.76		44.4		*Do3*	S.S. with Sr [*Do3*], distorted Hex. (9L); structure [*Ro2b*]	
$SrIrO_3$	M	5.60	9.62	14.17	$\beta = 93° 16'$	*Lo1a*	Prep. [*Ro2a*], distorted Hex (6L)	
	O	5.58	5.60	7.89		*Lo1a*	High pressure phase (Perovskite)	
$PbIrO_3$	C	10.271				*Lo4*	P&S [*Ra6*], defect pyrochlore type	
$CaIrO_3$	O	3.145	9.855	7.293		*Ro2b*	Not perovskite	
$BaPbO_3$	C	4.265				*Wa2*	P&S [*We7, Ni3*], electrical properties [*Ik4*]	
$SrPbO_3$	O	5.864	5.949	8.336		*We7*		

Compound	Sym	a Å	b Å	c Å	angle	Ref.	Remarks	Magnetic Data
$A^{2+}B^{+4}O_3$ (continued)								in 3.3.4, Tab.
$BaThO_3$	C	8.985				*Sm30*	P&S [*Ho2, Na15, Me4, Be24*]	
$SrThO_3$	C	8.84				*Na15*	Pseudocubic, S.S. with Ba [*Be24*]	
$CaThO_3$	C	8.74				*Na15*	Pseudocubic	
$CdThO_3$	C	8.74				*Na15*	Pseudocubic	
$PbThO_3$	C	8.960				*Na15*	Pseudocubic	
$BaUO_3$	C	4.387				*La5*	P&S [*Sc16, Ru1, Tr9*], S.S. with $BaTiO_3$ [*Va9*]	
$BaNpO_3$	C	4.384				*Ke4*		
$BaPuO_3$	C	4.357				*Ke3*	Pseudocubic	
$SrPuO_3$	C	4.28				*Ke3*	Pseudocubic	
$A^{2+}B^{4+}X_3$ or $A^{3+}B^{3+}X_3$; X = S, Se								
$BaTiS_3$	H	6.77		5.74		*Cl1*	Hex (2L), P&S [*No9, As3b*], orthorhombic and tetragonal modifications [*Ha6*]	
$BaTiSe_3$	H	7.054		6.033		*As3a*	Hex (2L), P&S [*No9*]	
$SrTiS_3$	H	6.730		5.829		*Ha6*	Hex (2L), P&S [*No9*], orthorhombic and tetragonal modifications [*Ha6*]	
$PbTiS_3$	T	4.16		11.752		*St27*	"Layer structure" P&S [*No9*]	
$BaZrS_3$	O	7.037	9.983	7.050		*Cl3*	Distorted perovskite, P&S [*Ha6, No9, As3b*]	
$BaZrSe_3$	H	7.188		6.025		*As3a*	Hex (2L), P&S [*No9*]	
$SrZrS_3$	O	13.49	9.79	14.23		*Cl1*	Distorted perovskite, P&S [*No9*]	
$CaZrS_3$	O	13.07	9.58	14.05		*Cl1*	Distorted perovskite	
$BaTaS_3$	H	6.847		5.742		*As3b*	Hex (2L) P&S [*No9*]	
$BaTaSe_3$	H	7.134		5.987		*As3a*	Hex (2L) P&S [*No9*]	
$ATaSe_3$	O	11.0	6.8	11.9		*No9*	A = Sr and Pb—not perovskite	
$LnInS_3$	O	≈ 3.95	≈ 11.78	20.98		*Ka13*	Ln = La, Ce, Pr, Nd and Sm; $T_{melt} \approx 1100$ °C	
$LnGaSe_3$	H	≈ 10.3		≈6.2		*Ka12a*	Ln = La, Ce, Pr, Nd, Sm; $T_{melt} = 1100$ °C	
$A^{3+}B^{3+}O_3$								
$LaAlO_3$	R	5.357			$\alpha = 60° 6'$	*Ge5*	P&S [*Be34, Da1, Re5, De14*], ESR: Gd, Cr [*Ki3, St16a*]. Luminescence: Eu [*Ya3, Bl13, Bl14*], Pr [*Ma30, De8*]. Cr [*Bl15, Bo14*]; twinning + detwinning [*Fa9, Fa10*]; nuclear quadrupole resonance [*De17*]; S.S. with $BaTiO_3$ [*Sm15, Is2b*]; space group, $R\bar{3}c$ [*Ra3, Ge4b*], Review [*Ge4b*]	
	C	3.818				*Ge5*	$T = 650$ °C; cubic $T > 522$ °C [*Wo15a, Ge4b, Ax3*], inelastic neutron scattering [*Ax3*]	
$CeAlO_3$	R	5.327			$\alpha = 60° 15'$	*Ki1*	P&S [*Be34, Ro16, Sc13, Ke2*]	
$PrAlO_3$	R	5.307			$\alpha = 60° 22'$	*Ge5*	P&S [*Be34, Ma27, Yu4, Zo1, Re5, Li2, Ru10, Sc13*]	6

$PrAlO_3$	R	5.307			$\alpha = 60° 22'$	*Ge5*	P&S [*Be34, Ma27, Yu4, Zo1, Re5, Li2, Ru10, Sc13*]	6

Compound	Sym	*a* Å	*b* Å	*c* Å	angle	Ref.	Remarks	Magnetic Data
$A^{3+}B^{3+}O_3$ (continued)								in 3.3.4, Tab.
$PrAlO_3$	T	3.74		3.76		*Ma27*	Discussion of disagreement between [*Ge5*] and [*Ma27*] given in [*Ge4a*] and [*To12a*]	6
$NdAlO_3$	R	5.286			$\alpha = 60° 25'$	*Ge5*	P&S [*Be34, Da2, Zo1, Ke2, Ge5, Re5, Li2, Ru10, Sc13, Da1*]	6
$SmAlO_3$	O	5.285	5.290	7.473		*Ge5*	P&S [*Be34, Ke2, Re5, Li2, Sc13, Zo1*]	6
	O	7.46	7.46	7.43		*Ma27*	Discussion of disagreement between [*Ge5*] and [*Ma27*] given in [*Ge4a*] and [*To12a*]	
	R	5.316			$\alpha = 60° 19'$	*Ge2*	$T = 850$ °C, rhombohedral $T > 800$ °C	
$EuAlO_3$	O	5.271	5.292	7.458		*Ge5*	P&S [*Bo14, Re5, Li2*]	6
	H	3.760		10.52		*Be36*	Prep. $T < 900$ °C, see Fig. 17a	
$GdAlO_3$	O	5.247	5.304	7.447		*Ge5*	P&S [*Be34, Da1, Ga28, Sc13, Li2, Ma39*]; optical properties [*Bl13, Bl14, Bl16, Ca8, Oh1*]; NMR, Al^{27} [*Bo2a*]	6
	H	3.73		10.51		*Be36*	Prep. < 900 °C, see Fig. 17a	
$TbAlO_3$	O	5.229	5.308	7.415		*Bi2*	Neutron diffraction [*Bi2*], P&S [*Ga28, Sc13*], optical properties [*Hu6, Hu6a*]	6
	H	3.730		10.51		*Be36*	Prop. < 900 °C, see Fig. 17a	
$DyAlO_3$	O	5.23	5.31	7.40		*Gi3*	P&S [*Be34,Ga28, Da1, Da2, Sc13*], neutron diffraction [*Bi1, He12*], optical properties [*Hu5, Sc24, Fa5*]	6
	H	3.700		10.50		*Be36*	Prep. < 900 °C, see Fig. 17a	
$HoAlO_3$	O	5.18	5.33	7.36		*Sc13*	P&S [*Ga28*]	6
	H	3.670		10.51		*Be36*	Prep. < 900 °C, see Fig. 17a	
$ErAlO_3$	O	5.16	5.32	7.33		*Sc13*	P&S [*Ga28*]	6
	H	3.660		10.50		*Be36*	Prep. < 900 °C, see Fig. 17a	
$TmAlO_3$	O	5.15	5.33	7.29		*Sc13*	P&S [*Ga28*]	
$YbAlO_3$	O	5.128	5.332	7.317		*Ga28*		
$LuAlO_3$							No perovskite [*Ga28, Sc13*]	
$YAlO_3$	O	5.179	5.329	7.370		*Ge6*	P&S [*Mi8, Be34*], ESR: Fe^{3+} and Gd^{3+} [*Wh3*]; decomposition of YAG [*Ma26*]	
	H	3.68		10.52		*Be36*	Prep. < 900 °C, see Fig. 17a	
$BiAlO_3$	T	7.61		7.94		*Na15*	Not able to be reproduced [*Bu3*]	
$PuAlO_3$	R	3.78			$\alpha = 90° 24'$	*Ru13*		
$AmAlO_3$	R	3.75			$\alpha = 90° 28'$	*Ke8*		
$LaScO_3$	O	5.678	5.787	8.098		*Ge2*	P&S [*Sc13, Ke2*]	
$CeScO_3$	O					*Ke2*	No dimensions	
$PrScO_3$	O	5.615	5.776	8.027		*Ge2*	P&S [*Sc13*]	
$NdScO_3$	O	5.574	5.771	7.998		*Ge2*	P&S [*Sc13, Ke2*]	
$SmScO_3$	O	5.53	5.76	7.95		*Sc13*		

Compound	Sym	a Å	b Å	c Å	angle	Ref.	Remarks	Magnetic Data
$A^{3+}B^{3+}O_3$ (continued)								in 3.3.4, Tab.
$EuScO_3$	O	5.51	5.76	7.94		*Sc13*		
$GdScO_3$	O	5.487	5.756	7.925		*Ge2*	P&S [*Sc13*], Prop. [*Bo36*]	6
$DyScO_3$	O	5.43	5.71	7.89		*Sc13*		
$HoScO_3$	O	5.42	5.71	7.87		*Sc13*		
$YScO_3$	O	5.431	5.712	7.894		*Ge2*	P&S [*Sc13, Ke2*]	
$BiScO_3$	Tr	4.042	4.127	4.042	$\alpha = \gamma = 90° 41'$ $\beta = 91° 52'$	*To11b*	High pressure preparation [*To11a*]	
$LaTiO_{3-x}$	C	3.934				*We16*	P&S [*Si4, Be33, Ho12, Ke15, Ke16, Jo4*]	6
$La_{0.67}TiO_3$	C	3.887				*Ke18*	Ti^{4+}, S.S. with $SrTiO_3$ [*Ti1, Ke18, Ve9, We16*], $BaTiO_3$ [*Jo4*]	6
$CeTiO_3$	T	5.513		7.760		*We16*	P&S [*Be33, Ho12, Si4*]	6
$PrTiO_3$	T	5.508		7.742		*We16*	P&S [*Be33, Ho12, Si4*]	6
$NdTiO_3$	O	5.482	5.521	7.728		*We16*	P&S [*Be33, Ho12, Si4*]	6
$SmTiO_3$	O	5.398	5.568	7.651		*We16*	P&S [*Be33, Si4, Mc1c*]	6
$GdTiO_3$	O	5.353	5.655	7.616		*We16*	P&S [*Bo36, Ho12, Si4, Mc1c*]	6
$EuTiO_3$	C	7.810				*Ho12*	Ti^{4+}, P&S [*Br20, Mc1b*], Prop. [*Mc3, Mc4, Si4*], neutron diffraction [*Mc2*]	6
$TbTiO_3$	O	5.388	5.648	7.676		*Mc1c*		
$DyTiO_3$	O	5.361	5.659	7.647		*Mc1c*		
$HoTiO_3$	O	5.339	5.665	7.626		*Mc1c*		
$ErTiO_3$	O	5.318	5.657	7.613		*Mc1c*		
$TmTiO_3$	O	5.306	5.647	7.607		*Mc1c*		
$YbTiO_3$	O	5.293	5.633	7.598		*Mc1c*		
$LuTiO_3$	O	5.274	5.633	7.580		*Mc1c*		
$YTiO_3$	O	5.340	5.665	7.624		*Mc1c*		
$LaVO_3$	O'	5.540	5.540	7.83		*Wo14*	P&S [*Si5, Be33, Ke16, Re8, Wo4, Ke18, Ke15, Ya1, Ro3*], S.S. with: $SrVO_{2.5}$ [*Ke18, Wo14*], S.S. with $CaVO_{2.5}$ [*Wo14*]	6
$CeVO_3$	O'	5.486	5.486	7.74		*Wo14*	P&S [*Be33, Re8, Wo4*]	6
$PrVO_3$	O'	5.487	5.562	7.751		*Wo14*	P&S [*Be33, Re8, Wo4, Vi2, Ge2*]	6
$NdVO_3$	O	5.451	5.579	7.734		*Wo14*	P&S [*Be33, Re8, Wo4, Vi2, Ge2*]	6
$SmVO_3$	O	5.393	5.588	7.672		*Wo14*	P&S [*Be33, Re8, Wo4*]	6
$GdVO_3$	O	5.343	5.614	7.637		*Wo14*	P&S [*Be33, Bo36, Re8, Ge2*]	6
$DyVO_3$	O	5.302	5.602	7.601		*Wo14*	P&S [*Re8*]	6
$ErVO_3$	O	5.262	5.604	7.578		*Wo14*	P&S [*Re8*]	6
YVO_3	O	5.284	5.605	7.587		*Wo14*	P&S [*Ro3, Re8*]	6
$PuVO_3$	O	5.45	5.58	7.76		*Ru13*		
$AmVO_3$	O	5.48	5.61	7.78		*Ke8*		

Compound	Sym	a Å	b Å	c Å	angle	Ref.	Remarks	Magnetic Data
								in 3.3.4, Tab.
$A^{3+}B^{3+}O_3$ (continued)								
$LaCrO_3$	O	5.479	5.515	7.753		*Qu1*	Semiconducting 0.6 eV [*Ru11*], neutron diffraction [*Ko1*], optical properties [*Ru11*], dielectric properties [*Ra8*], P&S [*Ge2, Ru11, Wo4, Ke2, Na14*], S.S. with Ni, Mn [*Be33, Be21*]; T_{melt} = 2500 °C [*Fo2*], EPR [*We4*]	6
	R	5.47			α = 60° 32'	*Ru11*	T = 280 °C, rhombohedral 280 < T < 1030 °C	
	C	3.92				*Ru11*	T = 1230 °C	
$La_{0.9}Bi_{0.1}CrO_3$	O	5.47	5.50	7.75		*Iw1*		6
$La_{0.5}Sr_{0.5}CrO_{3-x}$	C	7.754				*Ya1*		
$CeCrO_3$	O	5.475	5.475	7.740		*Qu1*	P&S [*Ru10, Be33, Wo4, Ke2*]	6
$PrCrO_3$	O	5.448	5.479	7.718		*Qu1*	P&S [*Ge2, Ru10, Be33, Wo4*], T_{melt} = 2420 °C [*Fo2*], dielectric properties [*Ra8*]	6
$NdCrO_3$	O	5.425	5.478	7.694		*Qu1*	P&S [*Ru10, Ge2, Be33, Wo4, Ke2*], T_{melt} = 2405 °C [*Fo2*]	6
$SmCrO_3$	O	5.367	5.508	7.643		*Qu1*	P&S [*Ru10, Ge2, Be33, Wo4, Ke2*], T_{melt} = 2385 °C [*Fo2*]	6
$EuCrO_3$	O	5.340	5.515	7.622		*Qu1*	P&S [*Ru10*]	6
$GdCrO_3$	O	5.312	5.525	7.606		*Qu1*	P&S [*Ru10, Ge2, Be33*], T_{melt} = 2370 °C [*Fo2*]	6
$TbCrO_3$	O	5.291	5.518	7.576		*Qu1*	Neutron diffraction [*Be42, Ma24*], specific heat [*De1a*]	6
$DyCrO_3$	O	5.265	5.520	7.552		*Qu1*	Neutron diffraction [*Be38*], T_{melt} = 2345 °C [*Fo2*]; dielectric hysteresis disappears at ≈ 540 °C indicating no center of symmetry [*Ra8*]	6
$HoCrO_3$	O	5.243	5.519	7.538		*Qu1*	Neutron diffraction [*Be32, Be47, Be50*], dielectric properties [*Co6*], T_{melt} = 2330 °C [*Fo2*], dielectric hysteresis disappears at ≈ 460 °C indicating no center of symmetry [*Ra8*], S.S. with $HoMnO_3$ [*Ap1b*]	6
$ErCrO_3$	O	5.223	5.516	7.519		*Qu1*	Dielectric properties [*Co6*], T_{melt} = 2325 °C [*Fo2*]	6
$TmCrO_3$	O	5.209	5.508	7.500		*Qu1*		6
$YbCrO_3$	O	5.195	5.510	7.490		*Qu1*	T_{melt} = 2320 °C [*Fo2*], dielectric hysteresis disappears at ≈ 520 °C indicating no center of symmetry [*Ra8*]	6
$LuCrO_3$	O	5.176	5.497	7.475		*Qu1*	Dielectric hysteresis disappears at ≈ 480 °C indicating no center of symmetry [*Ra8*]	6
$YCrO_3$	O	5.241	5.521	7.532		*Qu1*	P&S [*Ge6, Ge2, Lo5, Ka18, Pa14, Yu5*], dielectric properties [*Ra8*], T_{melt} = 2340 °C [*Fo2*]	6
$InCrO_3$	O	5.170	5.355	7.543		*Sh9*	High pressure preparation	

Compound	Sym	a Å	b Å	c Å	angle	Ref.	Remarks	Magnetic Data
$A^{3+}B^{3+}O_3$ (continued)								in 3.3.4, Tab.
$TlCrO_3$	O	5.302	5.405	7.647		*Sh9*	High pressure preparation	
$BiCrO_3$	Tr	3.90	3.87	3.90	$\alpha = \gamma = 90°35'$ $\beta = 89°10'$	*Su10*	High pressure preparation; S.S. with $BiMnO_3$ [*To11a*]	6
$PuCrO_3$	O	5.46	5.51	7.76		*Ru13*		
$LaMnO_3$	O'	5.533	5.722	7.694		*Wo2*	P&S [*Na14*], neutron diffraction [*Ko1, Wo12*], S.S. with Ba, Sr, Ca [*Wo12, Ja4, Ja5, Jo8, Jo12, Ha22, Jo7, Jo9, Ya1, Ro11*], S.S. with Cr, Fe, Co, Ni [*Be33, Be21, Gi4, Jo7, Jo8, Jo9, Wo2, Wo6, Fu2, Bl7*], S.S. with (Ba, Sr, Ca, Pb)TiO_3 [*Ha31, Ha32, To3, To6, To12*], S.S. with $GdCoO_3$ [*De23*]	6
	R	3.892			$\alpha = 90°\ 36'$	*Wo2*	24% Mn^{4+}	
$CeMnO_3$	O'	5.537	5.557	7.818		*Ve12*		
$PrMnO_3$	O'	5.445	5.787	7.575		*Ve12*	P&S [*Be33, Vi1*], complete structure [*Qu2*]	
$NdMnO_3$	O'	5.380	5.854	7.557		*Ve12*	P&S [*Be33, Vi1, Sz1*], complete structure [*Qu2*]	6
$SmMnO_3$	O'	5.359	5.843	7.482		*Ve12*	P&S [*Be33*]	6
$EuMnO_3$	O'	5.338	5.842	7.453		*Ve12*	P&S [*Sz1*]	6
$GdMnO_3$	O'	5.313	5.853	7.432		*Ve12*	P&S [*Be33, Sz1*], S.S. with $LaCoO_3$ [*De23*]	6
$TbMnO_3$	O'	5.297	5.831	7.403		*Ve12*	Complete structure determination [*Qu2*]	6
$DyMnO_3$	O'	5.275	5.828	7.375		*Ve12*	P&S [*Sz1*]	6
	H	6.177		11.43		*Sz1*	Preparation temperature 1600 °C, see Fig. 17a	
$HoMnO_3$	H	6.136		11.42		*Ya2*	Magnetic properties [*Ve12, Be32*], dielectric properties [*Be35, Co7*], P&S [*Sz1*], see Fig. 17a	
	O'	5.26	5.84	7.35		*Wa4*	High pressure phase, P&S [*Wa5, Vi1, Sz1*]	
$ErMnO_3$	H	6.115		11.41		*Ya2*	Magnetic properties [*Ve12, Be32*], dielectric properties [*Be35, Co7*], see Fig. 17a	
	O'	5.24	5.82	7.335		*Wa4*	High pressure phase	
$TmMnO_3$	H	6.062		11.40		*Ya2*	Magnetic properties [*Ve12, Be32*], dielectric properties [*Be35, Co7*], see Fig. 17a	
	O'	5.23	5.81	7.32		*Wa4*	High pressure phase	
$YbMnO_3$	H	6.062		11.40		*Ya2*	Magnetic properties [*Ve12, Be32, Ro8, Bo11*], dielectric properties [*Be35, Ro8, Bo11, Co7, Is11*], P&S [*Sz1*], see Fig. 17a	
	O'	5.22	5.80	7.30		*Wa4*	High pressure phase	
$LuMnO_3$	H	6.042		11.37		*Ya2*	Magnetic properties [*Ve12, Be32*], dielectric properties [*Be35, Co7*], see Fig. 17a	
	O'	5.205	5.79	7.31		*Wa4*	High pressure phase	
$YMnO_3$	H	6.125		11.41		*Ya2*	Dielectric or magnetic properties [*Ta13, Ro8, Be35, Co5, Co7, Co3, Bo11, Is11, Pe17, Pe16, Be32, Be39, Be43, Be44, Be49, Ko3, Ki8*], see Fig. 17a	

Berichtigungen zu Band III/4a

S. 177, letzte Zeile: statt Ba_2TdPaO_6 **lies** Ba_2TbPaO_6

S. 219, Zeile 16 von unten: statt $KMg_{1-x}Ni_xFe_3$ **lies** $KMg_{1-x}Ni_xF_3$

S. 252, Zeile 26 von oben (Überschrift): statt $Sr_3Fe_3UO_9$ **lies** $Sr_3Fe_2UO_9$

Errata in Vol. III/4a

p. 177, bottom line: instead of Ba_2TdPaO_6 **read** Ba_2TbPaO_6

p. 219, line 16 from the bottom: instead of $KMg_{1-x}Ni_xFe_3$ **read** $KMg_{1-x}Ni_xF_3$

p. 252, line 26 from above (headline): instead of $Sr_3Fe_3UO_9$ **read** $Sr_3Fe_2UO_9$

Compound	Sym	a Å	b Å	c Å	angle	Ref.	Remarks	Magnetic Data
								in 3.3.4, Tab.
$A^{3+}B^{3+}O_3$ (continued)								
$YMnO_3$	O'	5.26	5.84	7.35		*Wa3*	High pressure phase; S.S. with: Fe, perovskite at 15% Fe [*Ch6*]	
$BiMnO_3$	M	10.93	11.31	7.98	$\beta = 92° 24'$	*Bo12*	P&S [*Su10*]; S.S. with Ca [*Bo6, Bo12, St19*], $PbTiO_3$ [*Bo6, Bo7*], Sr [*Iv1*], La [*Iv1*], $BiCrO_3$ [*To11a*]; crystallographic transformation $T = 210$ °C [*To11a*]	6
						Ru13	Pseudocubic	
$PuMnO_3$	C	3.86				*Ge6*	P&S [*Be33, Fo5, Re5, Wo3, Ke2, Da2, Na14, Ya1*], S.S. with Ni, Mn [*Be33*], S.S. with Al, Co, Cr, Sc [*Ka17, Wo3*], rhombohedral $T > 980$°C [*Da1*], S.S. with: $PbNb_2O_6$ [*Fr11*], Pb [*Re5a*], Bi [*Ri5b*]	6
$LaFeO_3$	O	5.556	5.565	7.862				
$CeFeO_3$	O	5.541	5.577	7.809		*Ro1a*	P&S [*Ke2, Be33*]	6
$PrFeO_3$	O	5.495	5.578	7.810		*Ge6*	P&S [*Be33, Fo5, Re5*], S.S. with Al, Co, Cr, Sc [*Ka17*]	6
$NdFeO_3$	O	5.441	5.573	7.753		*Ge6*	P&S [*Be33, Fo5, Re5, Wo3*], S.S. with Pb [*Re5a*], Bi [*Re5b*]	6
$SmFeO_3$	O	5.394	5.592	7.711		*Ge6*	P&S [*Be33, Fo5, Re5, Wo3*], S.S. with Pb [*Re5a*], Bi [*Re5b*]	6
$EuFeO_3$	O	5.371	5.611	7.686		*Ge6*	P&S [*Re5*], S.S. with Pb [*Re5a*], Bi [*Re5b*]	6
$GdFeO_3$	O	5.346	5.616	7.668		*Ge6*	P&S [*Be33, Re5*], crystal structure [*Co21*], S.S. with Pb [*Re5a*], Bi [*Re5b*]	6
$TbFeO_3$	O	5.326	5.602	7.635		*Ei1*	P&S [*Ko6*], S.S. with: Pb [*Re5a*], Bi [*Re5b*]	6
$DyFeO_3$	O	5.302	5.598	7.623		*Ei1*	P&S [*Da2*], S.S. with: Pb [*Re5a*], Bi [*Re5b*]	6
$HoFeO_3$	O	5.278	5.591	7.602		*Ei1*	P&S [*Ko6*], S.S. with: Pb [*Re5a*], Bi [*Re5b*], $HoMnO_3$ [*Ap1a*]	6
$ErFeO_3$	O	5.263	5.582	7.591		*Ei1*	P&S [*Fo5*], crystal structure [*Wi7*], S.S. with: Pb [*Re5a*], Bi [*Re5b*]	6
$TmFeO_3$	O	5.251	5.576	7.584		*Ei1*	Crystal structure [*Wi8*], S.S. with: Pb [*Re5a*], Bi [*Re5b*]	6
$YbFeO_3$	O	5.233	5.557	7.570		*Ei1*	P&S [*Ko6, Be1, Ha21*], S.S. with: Pb [*Re5a*], Bi [*Re5b*]	6
$LuFeO_3$	O	5.213	5.547	7.565		*Ei1*	P&S [*Sa6*], S.S. with: Pb [*Re5a*], Bi [*Re5b*]	6
$YFeO_3$	O	5.283	5.592	7.603		*Ei1*	P&S [*Fo5, Ru11, Ko6, Wo3, Ge4, Ma26, Va7, Sh12a*], crystal structure [*Co21*], S.S. with: Pb [*Re5a*], Bi [*Re5b*]	6
$TlFeO_3$	O	5.319	5.448	7.796		*Sh9*		

Compound	Sym	a Å	b Å	c Å	angle	Ref.	Remarks	Magnetic Data
$A^{3+}B^{3+}O_3$ (continued)								in 3.3.4, Tab.
$BiFeO_3$	R	5.62			$\alpha = 59° 41'$	*Mi0*	P&S [*Fi12, Is10, Ko5, Kr4, To7, To9, To12, Yu3, Yu1, Za2, Sm34, To10, Ge10a, Ro22*], neutron diffraction [*Pl1, Ki4, Ki5, Ki6, Bh2*], S.S. with: $LaAlO_3$ [*Fe5*], $LnFeO_3$ [*Kr5, Kh5, Ro7, Ro9, Is10b, Ro10, Ki6*], Pb(Ti, Zr)O_3 [*La6, Fe8, Ge10, Fe2, Sm7*], $BaTiO_3$ [*Ve5, Ka15*], $SrTiO_3$ [*Fe6*], $LaCrO_3$ [*Ro5*], $SrSnO_3$ [*Hi1*], $Bi_4Ti_3O_{12}$ [*Is12*], $SrFeO_3$ [*Ma8*], Pb_2FeNbO_6 [*Ro10, Yu1, Yu2, Sm12, Sm13, Is10a, Zh1, Is8, Kr3, Kr5*], $Sr(Sn_{1/3}Mn_{2/3})O_3$ [*Mi6, Vi4*], $Sr_{0.7}La_{0.3}MnO_3$ [*Ro10*], $PbNb_2O_6$ [*Fr11*]; $BiMnO_3$ [*Ma31*], $Pb(Fe_{2/3}W_{1/3})O_3$ [*Sm26*], $PrFeO_3$ [*Vi4a*], complete structure S.G. R3c [*Mi0*]	6
$LaCoO_3$	R	5.436			$\alpha = 60° 48'$	*Wo9*	R$\bar{3}$c, $T < 375$ °C; R$\bar{3}$, $T > 375$° [*Ra3*]; P&S [*As3, Wo4, He7, Sc23*], Prop. [*Me17, Ko1, Ra3, Ge12, Ra3, Jo9, Go16, Na1, Bl6, He7, Mu4, Me18*], S.S. with Sr [*Me18, Ra4, Jo13*], S.S. with Sr and Th [*Sc23*]	6
	R	5.52			$\alpha = 60° 0'$	*Ra3*	$T = 937$ °C: atomic positions demand R$\bar{3}$ symmetry	
$PrCoO_3$	O	5.331	5.373	7.587		*Be33*	P&S [*Wo4*]	
$NdCoO_3$	O	5.336	5.336	7.547		*Be33*	P&S [*Wo4*], thermal conductivity [*Ge12*]	6
$SmCoO_3$	O	5.289	5.354	7.541		*Be33*	P&S [*Wo4*]	
$GdCoO_3$	O	5.228	5.404	7.436		*Be33*	P&S [*As5*]	6
$TbCoO_3$							Studied in review of $TbBO_3$ compounds [*Ma24*]. No cell dimension	6
$BiCoO_3$	C	4.228				*To11b*	High pressure preparation [*To11a*]	6
$LaNiO_3$	R	5.461			$\alpha = 60° 49'$	*Wo8*	P&S [*Wo6*], neutron diffraction [*Ko1*]	6
$BiNiO_3$	C	4.173				*To11b*	High pressure preparation [*To11a*]	6
$LaGaO_3$	O	5.496	5.524	7.787		*Ge2*	P&S [*Ke2, Da2, Be34, Br25, Da1, Ma25a*]	
	R	5.544			$\alpha = 60° 25'$	*Ge2*	$T = 900$ °C, rhombohedral $T > 875$ °C (by DTA)	
$CeGaO_3$	C	3.87				*Ke2*	Distorted	
$PrGaO_3$	O	5.465	5.495	7.729		*Ge2*	P&S [*Be34, Br25, Ma25a*]	
$NdGaO_3$	O	5.426	5.502	7.706		*Ge2*	P&S [*Da1, Be34, Br25, Ke2, Ma25a*], complete structure [*Br26*], S.S. with $LaGaO_3$ [*Br25*]	6
$SmGaO_3$	O	5.369	5.520	7.650		*Ma25a*	High pressure preparation	
$EuGaO_3$	O	5.351	5.528	7.628		*Ma25a*	High pressure preparation	
$GdGaO_3$	O	5.322	5.537	7.606		*Ma25a*	High pressure preparation [*Ma25*]	
$TbGaO_3$	O	5.307	5.531	7.578		*Ma25a*	High pressure preparation	

Compound	Sym	a Å	b Å	c Å	angle	Ref.	Remarks	Magnetic Data in 3.3.4, Tab.
$A^{3+}B^{3+}O_3$ (continued)								
$DyGaO_3$	O	5.282	5.534	7.556		*Ma25a*	High pressure preparation	
$HoGaO_3$	O	5.251	5.531	7.536		*Ma25a*	High pressure preparation	
$ErGaO_3$	O	5.239	5.527	7.522		*Ma25a*	High pressure preparation	
$TmGaO_3$	O	5.224	5.515	7.505		*Ma25a*	High pressure preparation [*Ma25*]	
$YbGaO_3$	O	5.208	5.510	7.490		*Ma25a*	High pressure preparation	
$LuGaO_3$	O	5.188	5.505	7.484		*Ma25*	High pressure preparation [*Ma26*]	
$YGaO_3$	O	5.257	5.536	7.533		*Ge3*	P & S [*Pa2, Mo6*], optical properties (Eu^{3+}) [*Bl13*]	
$LaYO_3$	O	5.868	6.071	8.438		*To11b*	High pressure preparation [*To11a*]	
$BiYO_3$	C	4.2				*Si5*	Pseudocubic	
$LaNbO_3$	C	4.02				*Wo5*	P & S [*Ch11, Wo9, Kh1*]	
$LaRhO_3$	O	5.524	5.679	7.900		*Sh8a*	P & S [*Ch11*]	
$PrRhO_3$	O	5.4143	5.7473	7.8026		*Sh8a*	P & S [*Wo5*]	
$NdRhO_3$	O	5.3778	5.7551	7.7745		*Sh8a*	P & S [*Ch11*]	
$SmRhO_3$	O	5.3211	5.7613	7.7083		*Sh8a*		
$EuRhO_3$	O	5.2985	5.7607	7.6802		*Sh8a*	P & S [*Ch11*]	
$GdRhO_3$	O	5.2774	5.7605	7.6584		*Sh8a*		
$TbRhO_3$	O	5.2541	5.7492	7.6226		*Sh8a*		
$DyRhO_3$	O	5.2449	5.7314	7.6002		*Sh8a*	P & S [*Ch11*]	
$HoRhO_3$	O	5.2299	5.7257	7.5823		*Sh8a*	P & S [*Ch11*]	
$ErRhO_3$	O	5.2160	5.7117	7.5610		*Sh8a*		
$TmRhO_3$	O	5.2028	5.6974	7.5428		*Sh8a*		
$LuRhO_3$	O	5.1861	5.6700	7.5125		*Sh9*		
$InRhO_3$	O	5.301	5.435	7.586		*Ro16*	P & S [*Ge3, Pa2*]	
$LaInO_3$	O	5.723	5.914	8.207		*Ro16*		
$NdInO_3$	O	5.627	5.891	8.121		*Ro16*		
$SmInO_3$	O	5.589	5.886	8.082		*Sh9*	High pressure preparation	
$EuInO_3$	O	5.567	5.835	8.078		*Sh9*	High pressure preparation	
$GdInO_3$	O	5.548	5.842	8.071		*Sh9*	High pressure preparation	
$DyInO_3$	O	5.519	5.751	8.041		*Sh9*	High pressure preparation	
$YInO_3$	O	5.500	5.787	8.053		*Mo6*		6
$LaHoO_3$	O	5.888	6.092	8.480		*Sc12*	P & S [*Sc13, Mo6*]	6
$LaErO_3$	O	5.85	6.07	8.43		*Sc12*	P & S [*Sc13, Mo6*]	6
$LaTmO_3$	O	5.85	6.06	8.42		*Sc12*	P & S [*Sc13, Mo6*], complete structure determined, S.G. $Pbn2_1$, [*Mu8*], T_{melt} = 2120 °C [*Tr0*]	6
$LaYbO_3$	O	5.85	6.02	8.41		*Tr0*	T = 2080 °C	
	C	4.325				*Sc12*	P & S [*Sc13, Mo6*]	
$LaLuO_3$	O	5.82	6.02	8.37		*Mo6*		
$PrLuO_3$	O	5.751	5.977	8.320				

Tab. 2b. $A_2B'BX_6$ compounds

Compound	Sym	*a* Å	*b* Å	*c* Å	angle	Ref.	Remarks	Magnetic Data
$A_2^+B^+B^{3+}X_6$; X = F^{-1}, Cl^{-1}								in 3.3.4, Tab.
Cs_2NaAlF_6	H	6.168		29.76		*Ba5a*	Hex (12 L)	
Rb_2NaAlF_6	C	8.29				*Ba5a*		
Rb_2LiAlF_6	H	5.802		28.02		*Ba5a*	Hex (12L)	
K_2LiAlF_6	H	5.574		13.648		*Wi11b*	R perovskite	
	H	5.614		13.754		*Wi11b*	Hex (6L), Prep. $T > 470$ °C	
K_2NaAlF_6	C	8.105				*Me21*		
K_2KAlF_6	C	8.65				*St33*		
Na_2NaAlF_6	M	5.46	5.61	7.80	$\beta = 90° 11'$	*Na17*	P&S [*St33, Me19, Cr5a*], S.S. with Fe [*Cr5a*]	
$(NH_4)_2(NH_4)AlF_6$	C	8.90				*Pa9*	P&S [*Pa10, Me20*]	
Cs_2CsScF_6							Prep. [*Ba0*]	
Cs_2KScF_6	C	9.32				*Ho16a*		
Rb_2RbScF_6	C						Prep. [*Ba0*]	
K_2KScF_6	C	17.46				*Bo2*	Prep. [*Ba0*]	
Na_2NaScF_6	M	5.60	5.81	8.12	$\beta = 90° 45'$	*Th1*	$T < 680$ °C	
$(NH_4)_2(NH_4)ScF_6$	T	6.49		9.45		*Bo2*		
	C	9.26				*Bo2*	High temperature form	
K_2KTiF_6	T	8.56		8.75		*Br7*	P&S [*Ba5*], magnetic properties, $n_{eff} = 1.70$, $\Theta_p = 0$ °K [*Eh1*]	
K_2NaTiF_6	C	8.367				*Br7*	Structure determined [*Bu4a*]	
Na_2NaTiF_6	M	5.53	5.83	7.99	$\beta \cong 90°$	*Br7*	P&S [*Ba5*]	
Cs_2KVF_6	C	9.04				*Ba5a*		
Cs_2NaVF_6	H	6.267		30.40		*Ba5a*	Hex (12L)	
Rb_2KVF_6	C	8.88				*Ba5a*		
Rb_2NaVF_6	C	8.47				*Ba5a*		
Rb_2LiVF_6	H	5.891		28.77		*Ba5a*	Hex (12L)	
K_2KVF_6							Magnetic properties, $80 < T < 300$ °K, $n_{eff} = 2.79$, $\Theta_p = -14$ °K [*Fi4*]	
K_2NaVF_6	C	8.315				*Ba5*		
$(NH_4)_2(NH_4)VF_6$	C	9.04				*Pa6a*		
Cs_2RbCrF_6	C	9.15				*Ba5a*		
Cs_2KCrF_6	C	8.99				*Ba5a*		
Cs_2NaCrF_6	H	6.231		30.24		*Ba5a*	Hex (12L)	
Rb_2KCrF_6	C	8.81				*Ba5a*		
Rb_2NaCrF_6	C	8.42				*Ba5a*		
Rb_2LiCrF_6	H	5.865		28.61		*Ba5a*	Hex (12L)	
K_2KCrF_6	T	8.56		8.62		*Kl6*	P&S [*Pe2*]	
K_2KCrF_6	C	8.54				*Bo2*	High temperature form	

K_2NaCrF_6	C	8.54				*Bo2*	High temperature form	

Compound	Sym	*a* Å	*b* Å	*c* Å	angle	Ref.	Remarks	Magnetic Data
$A_2^+B^+B^{3+}X_6$; X = F^{-1}, Cl^{-1} (continued)								in 3.3.4, Tab.
K_2NaCrF_6	C	8.266				*Kn5*	Prop. [*Sh28*]	
Na_2NaCrF_6	M	5.468	5.679	7.878	$\beta \approx 90°$	*Vo1*		
$(NH_4)_2(NH_4)CrF_6$	C	9.01				*Pa6a*		
K_2KMnF_6	T	17.50		16.60		*Pe2*	Magnetic properties, $p^* = 4.95\,\mu_B$ [*Pe2*]	
K_2NaMnF_6	T	8.171		8.577		*Kn4*		
Cs_2CsFeF_6	C	10.46				*Mi2*		
Cs_2KFeF_6	C	9.05				*Ba5a*	P&S [*Ho16a*]	
Cs_2NaFeF_6	H	6.260		30.40		*Ba5a*	Hex (12L)	
Rb_2RbFeF_6	C	8.88				*Bo2*		
Rb_2KFeF_6	C	8.87				*Ba5a*		
Rb_2NaFeF_6	C	8.47				*Ba5a*		
Rb_2LiFeF_6	H	5.891		28.77		*Ba5a*	Hex (12L)	
K_2KFeF_6	C	8.58				*Bo2*		
K_2NaFeF_6	C	8.323				*Kn5*		
Na_2NaFeF_6	M	5.506	5.719	7.925	$\beta = 90° 28'$	*Cr5a*	P&S [*Mi5*], magnetic properties, $92 < T < 296$ °K, $n_{eff} = 5.85$, $\Theta_p = -2$ °K [*Fi1*]	
Li_2LiFeF_6	C	8.88				*Mi2*	Magnetic properties, $93 < T < 293$ °K, $n_{eff} = 6.00$, $\Theta_p = 0$ °K [*Fi1*]	
$(NH_4)_2(NH_4)FeF_6$	T	6.39		9.30		*St33*	Low temperature form	
	C	9.10				*Pa9*	P&S [*St33*, *Kl6*]; magnetic properties, $92 < T < 294$ °K, $n_{eff} = 5.86$, $\Theta_p = -2$ °K [*Fi1*]	
Cs_2CsCoF_6	C	9.23				*Kl6*	Magnetic properties, $90 < T < 290$ °K, $n_{eff} = 5.28$, $\Theta_p = +2$ °K [*Kl6*]	
Rb_2RbCoF_6	C	8.90				*Kl6*	P&S [*Ho13*], magnetic properties, $90 < T < 290$ °K, $n_{eff} = 5.48$, $\Theta_p = -2°$ K [*Kl6*]	
K_2KCoF_6	C	8.57				*Kl6*	P&S [*Me27*, *Ho13*], magnetic properties, $73 < T < 300$ °K, $n_{eff} = 5.53$, $\Theta_p = -10°$ K [*Co23*, *Kl6*]	
K_2NaCoF_6	C	8.22				*Me27*		
Na_2NaCoF_6	C	7.91				*Kl6*	Pseudocubic, P&S [*Ho13*], magnetic properties, $90 < T < 290$ °K, $n_{eff} = 5.39$, $\Theta_p = -5$ °K [*Kl6*]	
K_2KNiF_6	C	8.44				*Bo2*	P&S [*Kl6*], magnetic properties, $90 < T < 295$ °K, does not obey Curie-Weiss law [*Kl2*, *Kl3*, *We20*]	
K_2KCuF_6	C	8.50				*Kl6*	Magnetic properties, $n_{eff} = 2.8$ [*Kl2*]	
Cs_2KGaF_6	C	8.975				*Ho16a*		
K_2NaGaF_6	C	8.246				*Kn5*		
$(NH_4)_2(NH_4)GaF_6$	C	9.041				*Sc26*		
Cs_2KAgF_6	C	9.175				*Ho16*		

Compound	Sym	a Å	b Å	c Å	angle	Ref.	Remarks	Magnetic Data
$A_2^+B^+B^{3+}X_6$; X = F^{-1}, Cl^{-1} (continued)								in 3.3.4, Tab.
Cs_2CsInF_6	C	9.50				*Bo2*		
Cs_2KInF_6	C	9.219				*Ho16a*		
Rb_2RbInF_6	C	9.20				*Bo2*		
K_2KInF_6	C	17.71				*Bo2*		
$(NH_4)_2(NH_4)MoO_3F_3$	C	9.10				*Pa9*		
Cs_2NaCeF_6	C	9.26				*Be52a*		
Cs_2KCeF_6	C	9.61				*Be52a*		
Cs_2RbCeF_6	C	9.75				*Be52a*		
Cs_2CsCeF_6	C	9.84				*Be52a*		
$CsKKCeF_6$	C	9.36				*Be52a*		
$CsRbRbCeF_6$	C	9.60				*Be52a*		
Rb_2KCeF_6	C	9.40				*Be52a*		
Rb_2RbCeF_6	C	9.49				*Be52a*	P&S [*Bo2*]	
$RbKKCeF_6$	C	9.20				*Be52a*		
K_2KCeF_6	C	9.07				*Be52a*		
Rb_2RbPrF_6	C	9.48				*Bo2*		
Cs_2NaSmF_6	C	9.163				*Al4*		
Rb_2NaSmF_6	C	8.988				*Al4*		
Cs_2NaTbF_6	C	9.107				*Al4*		
Rb_2NaTbF_6	C	9.9208				*Al4*		
Rb_2NaHoF_6	C	8.881				*Al4*		
Cs_2NaErF_6	C	9.061				*Al4*	Structure refined	
Rb_2NaErF_6	C	8.867				*Al4*	Structure refined	
Cs_2NaYbF_6	C	9.022				*Al4*		
Rb_2NaYbF_6	C	8.824				*Al4*		
Cs_2NaYF_6	C	9.056				*Al4*		
Rb_2NaYF_6	C	8.8693				*Al4*		
$Cs_2AgAuCl_6$	T	7.38		11.01		*El3*	Magnetic properties [*El1*], P&S [*Fe19*]	
$Cs_2AgAuCl_6$	C	5.28				*El3*		
$Cs_2AuAuCl_6$	T	7.49		10.87		*El3*	Magnetic properties [*El1*]	
Cs_2KTlF_6	C	9.36				*Ho16a*		
K_2KTlF_6	C	11.86				*Bo2*		
$(A^{2+}A^{3+})(B^{3+}B^{4+})O_6$								
$BaLaMnTiO_6$	C	3.960				*Ha32*	S.S. with Sr, rhombohedral > 30% Sr	
$SrLaMnTiO_6$	R	3.912			α = 90° 12'	*Ha32*	Cubic > 700 °C	
$CaLaMnTiO_6$	R	3.872			α = 90° 6'	*Ha32*		
$CaYMnTiO_6$	O	5.32	5.53	7.54		*Ha32*	S.S. with La	
$PbLaMnTiO_6$	R	3.933			α = 90° 12'	*Ha32*	S.S. with $x = Pb_2NbMnO_6$; cubic ≥ 50%	

$PbLaMnTiO_6$	R	3.933			$\alpha = 90°\ 12'$	*Ha32*	S.S. with $x = Pb_2NbMnO_6$; cubic $\geq 50\%$	

Compound	Sym	*a* Å	*b* Å	*c* Å	angle	Ref.	Remarks	Magnetic Data
$(A^{2+}A^{3+})\ (B^{3+}B^{4+})O_6$ (continued)								in 3.3.4, Tab.
$SrLaFeTiO_6$	C	3.92				*Bl8*		
$SrLaMnIrO_6$	C	3.93				*Bl8*		
$SrLaFeIrO_6$	C	3.94				*Bl8*		
$A_2^{3+}BB'O_6$								
La_2MgTiO_6	C	3.96				*Ag1*	P & S [*Ro20*], Eu^{3+} fluorescence [*Bl14*], S.S. with: Ni and optical properties [*Re4a*]	
Nd_2MgTiO_6	C	3.90				*Ro20*	Slight distortion	
$LaCeMgTiO_6$	C	3.929				*Ro20*	Slight distortion	
Bi_2MgTiO_6	C	3.98				*Su5*	Some question on atom positions	
$Y_2Ni_{0.4}Mg_{0.6}TiO_6$	C	3.83				*Re4a*	Optical properties	
La_2MgMnO_6						*Bl7*		
La_2CoMnO_6						*Bl7*	See $LaMnO_3$ systems for magnetic properties	
La_2NiMnO_6						*Bl7*	See $LaMnO_3$ systems for magnetic properties, P & S [*Fu2*]	
La_2CuMnO_6						*Bl7*	See $LaMnO_3$ systems for magnetic properties	
La_2MgGeO_6	C	3.90				*Ro20*		
Y_2MgGeO_6	C	3.88				*Re4a*		
La_2MgZrO_6	C	4.06				*Ra1*	S.S. with Ni and optical properties [*Re4a*]	
La_2CaZrO_6	C	4.174				*Ra1*		
La_2LiNbO_6	O	5.59	5.76	7.92		*Bl1a*	Eu^{3+} fluorescence [*Bl14*]	
La_2MgRuO_6	C	7.91				*Ga5*	Semiconducting, $\Delta E = 0.046$ eV	
La_2MnRuO_6	C	7.84				*Ga5*		
La_2NiRuO_6	C	7.90				*Ga5*	Semiconducting, $\Delta E = 0.12$ eV	
La_2ZnRuO_6	C	7.97				*Ga5*		
$La_2Ni_{0.4}Mg_{0.6}SnO_6$	C	4.02				*Re4a*	Optical properties	
La_2MgReO_6	C	7.926				*Ba25a*		
La_2NiReO_6	C	7.908				*Ba25a*		
La_2CoReO_6	T	5.611		7.968		*Ba25a*		
La_2FeReO_6							Disproportionates [*Ba25a*]	
La_2MgIrO_6	C	7.92				*Ga5*	"Complex magnetic properties" [*Bl7*], P & S [*Bl8*]	
La_2MnIrO_6	C	7.86				*Ga5*		
La_2CoIrO_6	O	5.60	5.60	7.92		*Bl8*	"Complex magnetic properties" [*Bl7*]	
La_2NiIrO_6	C	7.90				*Ga5*	"Complex magnetic properties" [*Bl7*], P & S [*Bl8*]	
La_2CuIrO_6	M	5.80	5.60	7.72	$\gamma = 86°\ 56'$	*Bl8*	"Complex magnetic properties" [*Bl7*]	
$A_2^{2+}BV^{5+}O_6$								
Ba_2BiVO_6	O	6.123	6.180	8.622		*Ve2*	P & S [*Vi3, Ve3*], dielectric properties [*Vi2b*]	
	C	4.372				*Ve2*	Cubic > 320 °C	

Compound	Sym	a Å	b Å	c Å	angle	Ref.	Remarks	Magnetic Data
$A_2^{2+}BNb^{5+}O_6$								in 3.3.4, Tab.
Ba_2ScNbO_6	C	8.220				*Fi10*	P&S [*Ag1, Br16*]	
Ba_2VNbO_6	C	4.051				*Ch10*		
Ba_2MnNbO_6	C	4.090				*Ha32*	P&S [*Ag1*]	6
Ba_2FeNbO_6	C	4.057				*Ga1*	P&S [*Ga13, Fi10, Ag1*]	
Ba_2CoNbO_6	C	4.06				*Bl8*		
Ba_2NiNbO_6	C	4.1				*Bl8*		
$Ba_2SrNbO_{5.5}$	C	8.54				*Ga1*		
Ba_2YNbO_6	C	4.180				*Br16*	P&S [*Fi10*]	
Ba_2RhNbO_6	C	8.17				*Bl8*		
Ba_2InNbO_6	C	8.279				*Br16*	P&S [*Ga1*]	
$Ba_2BaNbO_{5.5}$	C	8.68				*Ga1*		
Ba_2LaNbO_6	T	8.607		8.690		*Ga1*	P&S [*Br16*], cubic $T > 300$ °C [*Fi10*]	
Ba_2CeNbO_6	C	4.293				*Br16*	Probably ordered	
Ba_2PrNbO_6	C	4.285				*Br16*	Probably ordered, cubic $T > 300$ °C [*Fi10*]	
Ba_2NdNbO_6	C	8.540				*Ga1*	P&S [*Br16*], cubic $T > 300$ °C [*Fi10*]	
Ba_2SmNbO_6	C	8.518				*Ga1*	P&S [*Br16*], cubic $T > 300$ °C [*Fi10*]	
Ba_2EuNbO_6	C	8.507				*Ga1*	P&S [*Br16*]	
Ba_2GdNbO_6	C	8.496				*Ga1*	P&S [*Br16*], fluorescences [*Bl11, Ni1, Bl14*]	6
Ba_2TbNbO_6	C	4.229				*Br16*	Probably ordered	
Ba_2DyNbO_6	C	8.437				*Ga1*	P&S [*Br16*]	
Ba_2HoNbO_6	C	8.434				*Ga1*	P&S [*Br16*]	
Ba_2ErNbO_6	C	8.427				*Ga1*	P&S [*Br16*]	
Ba_2TmNbO_6	C	8.408				*Ga1*	P&S [*Br16*]	
Ba_2YbNbO_6	C	8.374				*Ga1*	P&S [*Br16*], dielectric properties [*Ag1*]	
Ba_2LuNbO_6	C	8.364				*Ga1*	P&S [*Br16*]	
Ba_2TlNbO_6	C	8.42				*Sl6*		
Ba_2BiNbO_6	R	6.086			$\alpha = 60° 21'$	*Ve2*	P&S [*Vi3, Ve3*], dielectric properties [*Vi2b*]	
Sr_2AlNbO_6	C	7.784				*Fi10*	P&S [*Sl1*]	
$Sr_2CaNbO_{5.5}$	C	8.20				*Ga13*		
Sr_2VNbO_6	C	3.965				*Ch10*		
Sr_2CrNbO_6	C	7.87				*Bl8*	P&S [*Br14*]	
Sr_2MnNbO_6	R	3.97			$\alpha \approx 90°$	*Ha32*	P&S [*Ku12*], cubic $T > 200$ °C [*Ku12*]	6
Sr_2FeNbO_6	T	3.960		3.980		*Ku6*	P&S [*Ga13, Ku12*]	
	C	3.968				*Ku6*	$T = 250$ °C, cubic $T \geq 250$ °C	
Sr_2CoNbO_6	C	3.93				*Bl8*		
Sr_2GaNbO_6	C	3.9477				*Br14*		
$Sr_2SrNbO_{5.5}$	C	8.34				*Ga13*		
Sr_2YNbO_6	R	5.184			$\alpha = 59° 51'$	*Ku12*	Cubic $T > 630$ °C	
Sr_2InNbO_6	C	8.106				*Fi10*	P&S [*Br14*]	

Compound	Sym	a Å	b Å	c Å	angle	Ref.	Remarks	Magnetic Data
$A_2^{2+}BNb^{5+}O_6$ (continued)								in 3.3.4, Tab.
Sr_2PrNbO_6	T	5.822		8.431		*Ku12*		
Sr_2NdNbO_6	T	5.780		8.367		*Ku12*		
Sr_2SmNbO_6	M	5.85	5.94	8.30	$\beta = 90°\ 12'$	*Fi10*	P&S [*Ku12*]	
Sr_2EuNbO_6	M	5.84	5.91	8.30	$\beta = 90°\ 12'$	*Fi10*		
Sr_2GdNbO_6	M	5.83	5.90	8.28	$\beta = 90°\ 15'$	*Fi10*		
Sr_2TbNbO_6	M	5.82	5.88	8.27	$\beta = 90°\ 8'$	*Fi10*		
Sr_2DyNbO_6	M	5.81	5.87	8.26	$\beta = 90°\ 9'$	*Fi10*		
Sr_2HoNbO_6	M	5.81	5.86	8.23	$\beta = 90°\ 6'$	*Fi10*		
Sr_2ErNbO_6	M	5.80	5.84	8.23	$\beta = 90°\ 4'$	*Fi10*		
Sr_2TmNbO_6	C	8.20				*Fi10*	Slight distortion	
Sr_2YbNbO_6	C	8.196				*Ku12*	Cubic $T > 540$ °C	
Sr_2LuNbO_6	C	8.19				*Ku12*	Cubic $T > 540$ °C	
$SrLaCoNbO_6$	C	7.99				*Bl8*		6
$SrLaNiNbO_6$	C	7.95				*Bl8*		6
$SrLaCuNbO_6$	T	7.80		8.28		*Bl8*		
La_2LiNbO_6							Ordered perovskite (Eu^{3+} fluorescence) [*Bl14*]	
Ca_2AlNbO_6	O	5.382	5.408	7.614		*Fi8*		
Ca_2VNbO_6	O	5.44	5.51	7.77		*Ch9*		
Ca_2CrNbO_6	O	5.418	5.494	3.858		*Fi8*		
Ca_2MnNbO_6	O	5.44	5.55	7.74		*Ha32*		6
Ca_2FeNbO_6	O	5.451	5.551	3.881		*Fi8*		
Ca_2YNbO_6	O	5.580	5.819	8.046		*Fi8*		
Ca_2InNbO_6	O	5.532	5.715	7.913		*Fi8*		
Ca_2LaNbO_6	O	5.652	5.866	8.140		*Fi8*		
Ca_2PrNbO_6	O	5.623	5.866	8.116		*Fi8*	Possibly lower symmetry	
Ca_2NdNbO_6	O	5.612	5.858	8.104		*Fi8*	Possibly lower symmetry	
Ca_2SmNbO_6	M	5.590	5.860	8.090	$\beta = 90°\ 10'$	*Fi8*		
Ca_2GdNbO_6	M	5.572	5.841	8.080	$\beta = 90°\ 12'$	*Fi8*		
Ca_2TbNbO_6	O	5.571	5.830	8.072		*Fi8*		
Ca_2DyNbO_6	O	5.580	5.819	8.062		*Fi8*		
Ca_2HoNbO_6	O	5.580	5.812	8.050		*Fi8*		
Ca_2ErNbO_6	O	5.575	5.794	8.020		*Fi8*		
Ca_2YbNbO_6	O	5.571	5.769	8.000		*Fi8*		
Pb_2AlNbO_6	C	10.53				*Fi11*	Defect pyrochlore type P&S [*Ag1, Ve4*]	
Pb_2ScNbO_6	T	4.074		4.083		*Is2*	Dielectric properties [*Jo3, Sm18, Te8e*], S.S. with $Pb(Ti, Zr, Hf)O_3$ [*Jo3*], crystal growth [*Ga5*]	
$Pb_2Sc_{0.5}Cr_{0.5}NbO_6$	C	4.060				*To1*	Possible rhombohedral distortion	
Pb_2CrNbO_6	C	10.54				*Fi11*	Defect pyrochlore type	
Pb_2MnNbO_6	C	4.023				*Fi11*	P&S [*Ha32*], S.S. with Fe and $PbTiO_3$ [*Ha31*]	6

Compound	Sym	a Å	b Å	c Å	angle	Ref.	Remarks	Magnetic Data
$A_2^{2+}BNb^{5+}O_6$ (continued)								in 3.3.4, Tab.
Pb_2FeNbO_6	R	4.014			$\alpha = 89° 55'$	*Ku10*	P&S [*Ro8*], S.S. with $BiFeO_3$ [*Sm12, Is8, Yu2*], complete structure [*Pl3*], crystal growth [*Ga5*], dielectric properties [*Kh8, Sm25, Sm16, Bo8, Sh32, Sk1, Sh33*], optical spectra [*Pi5*], B site ordering [*Yu9*], S.S. with Ta [*Sh33*]	6
Pb_2CoNbO_6	C	8.084				*Ro8*	Dielectric properties [*Ku10, Ag1, Ve4*]	6
Pb_2NiNbO_6	C	4.030				*Ku10*	Dielectric properties [*Ku10*] with 5% Ba [*Sh32*]	6
Pb_2GaNbO_6							High pressure preparation, no dimension [*To11a*]	
Pb_2YNbO_6	C	10.65				*Fi11*	Pyrochlore type	
Pb_2InNbO_6	C	4.110				*Ku9*	Dielectric properties [*Ku10*]	
Pb_2HoNbO_6	O	5.86	5.91	8.21		*Ku9*	Dielectric properties [*Ku10*]	
Pb_2TmNbO_6	O	5.858	5.936	8.178		*Ku10*		
Pb_2YbNbO_6	O	5.848	5.918	8.186		*Fi11*	Cubic $T > 280$ °C, dielectric properties [*Sm25, Ku9, Ku10, Ag1, Is17*], S.S. with $PbFe_{2/3}W_{1/3}O_3$ [*To5, To11, Ro11*]	
Pb_2LuNbO_6	O	5.850	5.902	8.176		*Ku9*	Cubic $T > 280$ °C, dielectric properties [*Ku9, Ku10, Is17*]	
Pb_2BiNbO_6	M	10.777	10.643	10.777	$\beta = 90° 29'$	*Vi3*	Defect pyrochlore type	
$Pb_2Mg_{0.5}Mn_{0.5}NbO_6$	C	4.018				*Vi5*	Dielectric properties [*Ve4, Vi5*]	
$Pb_2Co_{0.5}Mn_{0.5}NbO_6$	C	4.020				*Vi5*	Dielectric properties [*Ve4, Vi5*]	6
$Pb_2Ni_{0.5}Mn_{0.5}NbO_6$	C	4.018				*Vi5*	Dielectric properties [*Ve4, Vi5*]	6
$Pb_2Zn_{0.5}Mn_{0.5}NbO_6$	C	4.028				*Vi5*	Dielectric properties [*Ve4, Vi5*]	
$Pb_2Cd_{0.5}Mn_{0.5}NbO_6$	C	4.060				*Ro8*	Dielectric properties [*Ve4, Vi5, Ro8, Ve3*]	6
$A_2^{2+}BSb^{5+}O_6$								
Ba_2ScSbO_6	C	8.197				*Sl6*		
Ba_2CrSbO_6							Not perovskite [*Bl8*]	
Ba_2MnSbO_6							Not perovskite [*Bl8*]	
Ba_2FeSbO_6	H	5.79		14.22		*Bl8*	Hex (6L), P&S [*Sl6, Bl3*]	6
Ba_2CoSbO_6	H	5.72		14.00		*Bl8*	Hex (6L)	
Ba_2NiSbO_6							Not perovskite [*Bl8*]	
Ba_2RhSbO_6	H	5.78		14.20		*Bl8*	Hex (6L)	
Ba_2InSbO_6	C	8.269				*Sl6*	P&S [*Bl3, Bl8*]	
Ba_2GdSbO_6	C	8.44				*Bl8*		
Sr_2CrSbO_6	C	7.87				*Bl8*	P&S [*Sl6, Bl3*]	6
Sr_2MnSbO_6	T	7.86		8.08		*Bl8*		6
Sr_2FeSbO_6	C	7.90				*Bl8*	P&S [*Sl6, Bl3*]	6
Sr_2CoSbO_6	C	7.88				*Bl8*		6
Sr_2NiSbO_6	T					*Bl8*	Not single phase (no dimensions)	

Compound	Sym	a Å	b Å	c Å	angle	Ref.	Remarks	Magnetic Data
Sr_2NiSbO_6	T					*Bl8*	Not single phase (no dimensions)	

Compound	Sym	a Å	b Å	c Å	angle	Ref.	Remarks	Magnetic Data
$A_2^{2+}BSb^{5+}O_6$ (continued)								in 3.3.4, Tab.
Sr_2GaSbO_6	T	7.84		7.91		*Sl6*		
Sr_2RhSbO_6	O	5.55	5.77	7.99		*Bl8*		6
Ca_2FeSbO_6	O	5.47	5.54	7.74		*Bl8*		
$SrLaMgSbO_6$						*Bl14*	Eu^{3+} fluorescence, no dimensions	6
$SrLaCoSbO_6$	C	7.99				*Bl8*		6
$SrLaNiSbO_6$	C	7.93				*Bl8*		
$SrLaCuSbO_6$	T	7.80		8.35		*Bl8*		
$A_2^{2+}BTa^{5+}O_6$								
Ba_2AlTaO_6							No compound [*Ag1*, *Sm8*]	
Ba_2ScTaO_6	C	8.220				*Fi10*	Dielectric properties [*Ag1*, *Br13*, *Br14*], P&S [*Ga15*]	
Ba_2VTaO_6	C	8.104				*Sl1*	P&S [*Ch10*]	
Ba_2CrTaO_6	H					*Sl1*	Hex (6L) no dimensions	
Ba_2MnTaO_6	C	4.076				*Fi5*	P&S [*Sl1*]	
Ba_2FeTaO_6	C	4.048				*Fi5*	P&S [*Ga13*], dielectric properties [*Ag1*], S.S. with $BaTiO_3$ [*Na9*]	
Ba_2NiTaO_6	C	8.152				*Sl1*		
Ba_2YTaO_6	C	8.424				*Fi10*	P&S [*Ag1*, *Br13*, *Br14*, *Fi5*, *La9*], doped with Nd, Sm, Yb [*Ga15*]	
Ba_2InTaO_6	C	8.282				*Fi10*	P&S [*Ag1*, *Ga15*] doped with Nd, Sm, Yb [*Ga15*]	
$Ba_2BaTaO_{5.5}$	C	8.70				*Ga13*	P&S [*Br13*]	
Ba_2LaTaO_6	R	6.07			$\alpha = 60° 25'$	*Ga15*	P&S [*Br13*], doped with Nd [*Ga15*], cubic > 300 °C [*Fi5*]	
Ba_2PrTaO_6	R	6.05			$\alpha = 60° 10'$	*Fi10*	P&S [*Br13*, *Fi5*] cubic T > 300 °C [*Fi5*]	
Ba_2NdTaO_6	R	6.04			$\alpha = 60° 4'$	*Fi10*	P&S [*Br13*, *Fi5*] cubic T > 300 °C [*Fi5*]	
Ba_2SmTaO_6	R	6.01			$\alpha = 60° 4'$	*Fi10*	P&S [*Br13*, *Fi5*] cubic T > 300 °C [*Fi5*]	
Ba_2EuTaO_6	C	8.486				*Fi10*	P&S [*Ga15*]	
Ba_2GdTaO_6	C	8.470				*Fi10*	Doped with Nd [*Ga15*]	
Ba_2TbTaO_6	C	8.440				*Fi10*		
Ba_2DyTaO_6	C	8.420				*Fi10*	P&S [*Ga15*]	
Ba_2HoTaO_6	C	8.416				*Fi10*	P&S [*Ga15*]	
Ba_2ErTaO_6	C	8.398				*Fi10*	P&S [*Ga15*]	
Ba_2TmTaO_6	C	8.388				*Fi10*	P&S [*Ga15*]	
Ba_2YbTaO_6	C	8.378				*Fi10*	P&S [*Ga15*], dielectric properties [*Ag1*]	
Ba_2LuTaO_6	C	8.354				*Fi10*	P&S [*Ga15*], doped with Nd [*Ga15*]	
Ba_2TlTaO_6	C	8.42				*Sl1*		
Ba_2BiTaO_6	R	6.047			$\alpha = 60° 15'$	*Ve2*	Dielectric properties [*Vi3*, *Ve3*]	
Sr_2AlTaO_6	C	7.786				*Fi10*	P&S [*Sl1*], B-B' ordering [*Sl1*]	

Compound	Sym	a Å	b Å	c Å	angle	Ref.	Remarks	Magnetic Data
$A_2^{2+}BTa^{5+}O_6$ (continued)								in 3.3.4, Tab.
Sr_2VTaO_6	C	3.967				*Ch10*		
Sr_2CrTaO_6	C	3.94				*Na7*	P & S [*Ro20*], S.S. with Fe [*Na7*]	
Sr_2MnTaO_6	C	3.994				*Ku12*		
Sr_2FeTaO_6	T	3.960		3.981		*Ku7*	P & S [*Ku12*, *Sl1*, *Na5*, *Na6*, *Na7*], B-B' ordering [*Sl1*, *Be5*], S.S. with $SrTiO_3$ and Ba_2FeTaO_6 [*Na5*, *Be5*], S.S. with $BaTiO_3$ [*Na6*]	6
							Cubic at 250 °C [*Ku7*, *Na5*, *Na6*]	
	C	3.973				*Ku7*		
Sr_2GaTaO_6	C	7.892				*Sl1*		
$Sr_2SrTaO_{6.5}$	C	8.34				*Ga13*	P & S [*Br13*]	
	R	5.837			$\alpha = 59° 46'$	*Ku12*		
Sr_2YTaO_6	C	7.936				*Sl1*		
Sr_2RhTaO_6	C	8.110				*Fi10*	P & S [*Sl1*]	
Sr_2InTaO_6	T	5.853		8.387		*Ku12*	P & S [*Br13*]	
Sr_2LaTaO_6	M	5.87	5.98	8.35	$\beta = 90° 9'$	*Fi10*	P & S [*Ku12*]	
Sr_2PrTaO_6	M	5.86	5.96	8.34	$\beta = 90° 9'$	*Fi10*	P & S [*Ku12*]	
Sr_2NdTaO_6	M	5.85	5.93	8.31	$\beta = 90° 11'$	*Fi10*	P & S [*Ku12*]	
Sr_2SmTaO_6	M	5.84	5.91	8.30	$\beta = 90° 12'$	*Fi10*		
Sr_2EuTaO_6	M	5.83	5.90	8.29	$\beta = 90° 13'$	*Fi10*		
Sr_2GdTaO_6	M	5.82	5.88	8.28	$\beta = 90° 9'$	*Fi10*		
Sr_2TbTaO_6	M	5.82	5.87	8.26	$\beta = 90° 8'$	*Fi10*		
Sr_2DyTaO_6	M	5.81	5.85	8.23	$\beta = 90° 8'$	*Fi10*		
Sr_2HoTaO_6	M	5.80	5.84	8.23	$\beta = 90° 4'$	*Fi10*		
Sr_2ErTaO_6	C	8.20				*Ku12*	Slight distortion	
Sr_2TmTaO_6	C	8.196				*Fi10*		
Sr_2YbTaO_6	C	8.18				*Bl8*	Slight distortion	6
Sr_2LuTaO_6	C	7.99				*Bl8*		6
$SrLaCoTaO_6$	C	7.95				*Bl8*		
$SrLaNiTaO_6$	T	7.80		8.28		*Fi8*		
$SrLaCuTaO_6$	O	5.381	5.407	7.612		*Ch9*		
Ca_2AlTaO_6	O	5.45	5.49	7.76		*Fi8*		
Ca_2VTaO_6	O	5.418	5.491	3.857		*Fi8*	P & S [*Sl1*]	
Ca_2CrTaO_6	O	5.462	5.571	3.873		*Fi8*		
Ca_2MnTaO_6	O	5.451	5.560	3.880		*Fi8*		
Ca_2FeTaO_6	O	5.580	5.819	8.044		*Fi8*		
Ca_2YTaO_6	O	5.531	5.714	7.924		*Fi8*		
Ca_2InTaO_6	O	5.654	5.890	8.146		*Fi8*		
Ca_2LaTaO_6	O	5.629	5.867	8.116		*Fi8*	Possibly lower symmetry	
Ca_2PrTaO_6	O	5.616	5.857	8.106		*Fi8*	Possibly lower symmetry	
Ca_2NdTaO_6	O	5.606	5.853	8.096		*Fi8*		
Ca_2SmTaO_6	O							

Ca_2SmTaO_6	O	5.606	5.853	8.096			*Fi8*	Possibly lower symmetry Possibly lower symmetry

Compound	Sym	*a* Å	*b* Å	*c* Å	angle	Ref.	Remarks	Magnetic Data
$A_2^{2+}BTa^{5+}O_6$ (continued)								in 3.3.4, Tab.
Ca_2GdTaO_6	M	5.572	5.841	8.080	$\beta = 90° 12'$	*Fi8*		
Ca_2TbTaO_6	M	5.574	5.833	8.076	$\beta = 90° 12'$	*Fi8*		
Ca_2DyTaO_6	O	5.582	5.820	8.064		*Fi8*		
Ca_2HoTaO_6	O	5.586	5.811	8.054		*Fi8*		
Ca_2ErTaO_6	O	5.582	5.796	8.033		*Fi8*		
Ca_2YbTaO_6	O	5.570	5.772	8.002		*Fi8*		
Pb_2AlTaO_6	C	10.51				*Fi11*	Defect pyrochlore type, P & S [*Ag1*]	
Pb_2ScTaO_6	C	4.080				*Ga5*	P & S [*Is2, Ag1*], crystal growth [*Ga5*], dielectric properties [*Sm18*]	
Pb_2MnTaO_6	C	10.73				*Fi11*	Defect pyrochlore type, 5% Sr for Pb gives perovskite [*Sh32*]	6
Pb_2FeTaO_6	C	4.011				*Ga5*	P & S [*Ag1*], crystal growth [*Ga5*], Prop. [*Sh32*]	6
$Pb_2CoTaO_{5.5}$	C	4.038				*Ku11*	Dielectric properties [*Ku11, Sh32*]	6
Pb_2YTaO_6	C	10.70				*Fi11*	Defect pyrochlore type	6
Pb_2PrTaO_6	C	10.75				*Fi11*	Defect pyrochlore type	
Pb_2NdTaO_6	C	10.68				*Fi11*	Defect pyrochlore type	
Pb_2SmTaO_6	C	10.70				*Fi11*	Defect pyrochlore type	
Pb_2YbTaO_6	O	5.85	5.90	8.22		*Ku9*	Dielectric properties [*Ag1, Is17, Fi11*]	
Pb_2LuTaO_6	O	5.848	5.899	8.214		*Ku9*	Cubic $T > 280$ °C; dielectric properties [*Is17*]	
Pb_2BiTaO_6	T	10.686		10.816		*Vi3*	Distorted defect pyrochlore type	
$Pb_2Mg_{0.5}Mn_{0.5}TaO_6$	C	4.015				*Vi5*	Dielectric properties [*Vi5, Ve4*]	6
$Pb_2Ni_{0.5}Mn_{0.5}TaO_6$	C	4.009				*Vi5*	Dielectric properties [*Vi5, Ve4*]	6
$A_2^{2+}BB'O_6$; B' = Bi^{5+}, Pa^{5+}, Pu^{5+}								
Ba_2LaBiO_6	C	8.759				*Sc18b*		
Ba_2BiBiO_6	C					*Sc18b*	No dimensions, Bi^{3+}-Bi^{5+}	
Ba_2ScPaO_6	C	8.549				*Ke5*		
$Ba_2SrPaO_{5.5}$	C	8.860				*Ke5*		
Ba_2YPaO_6	C	8.718				*Ke5*		
Ba_2InPaO_6	C	8.596				*Ke5*		
$Ba_2BaPaO_{5.5}$	C	8.932				*Ke5*		
Ba_2LaPaO_6	C	8.885				*Ke5*		
Ba_2CePaO_6	C	8.800				*Ke5*	Ce^{4+} (?)	
Ba_2PrPaO_6	C	8.862				*Ke5*		
Ba_2NdPaO_6	C	8.840				*Ke5*		
Ba_2SmPaO_6	C	8.792				*Ke5*		
Ba_2EuPaO_6	C	8.783				*Ke5*		
Ba_2GdPaO_6	C	8.770				*Ke5*		
Ba_2TdPaO_6	C	8.753				*Ke5*		

Compound	Sym	*a* Å	*b* Å	*c* Å	angle	Ref.	Remarks	Magnetic Data
$A_2^{2+}BB'O_6$; B' = Bi^{5+}, Pa^{5+}, Pu^{5+} (continued)								in 3.3.4, Tab.
Ba_2DyPaO_6	C	8.740				*Ke5*		
Ba_2HoPaO_6	C	8.730				*Ke5*		
Ba_2ErPaO_6	C	8.716				*Ke5*		
Ba_2TmPaO_6	C	8.692				*Ke5*		
Ba_2YbPaO_6	C	8.678				*Ke5*		
Ba_2LuPaO_6	C	8.666				*Ke5*		
Ba_2PuPaO_6	C	8.748				*Ke5*		
Ba_2AmPaO_6	C	8.793				*Ke5*		
Sr_2LuPaO_6	C	8.462				*Ke5*		
$BaSrSrPaO_{5.5}$	C	8.784				*Ke5*		
Ba_2MnPuO_6	C	8.32				*Aw2*		
Ba_2InPuO_6	C	8.50				*Aw2*		
Ba_2LaPuO_6	C	8.63				*Aw2*	Pseudocubic	
Ba_2CePuO_6	C	8.72				*Aw2*		
Ba_2NdPuO_6	C	8.66				*Aw2*		
Ba_2TiPuO_6	C	8.06				*Aw2*	Pu^{4+}	
Ba_2ZnPuO_6	C	8.38				*Aw2*	Pseudocubic	
Ba_2PbPuO_6	C	8.58				*Aw2*		
$A_2^{2+}BMo^{6+}O_6$								
Ba_2CaMoO_6	C	8.355				*St32*		
Ba_2CrMoO_6							No compound [*Pa7*]	
Ba_2FeMoO_6	C	8.08				*Pa7*	S.S. with Sr [*Ga12*]	6
Ba_2CoMoO_6	C	4.043				*Br14*	Probably ordered	
Ba_2NiMoO_6	C	4.022				*Br14*	Probably ordered	
Sr_2CrMoO_6	C	3.91				*Br14*		6
Sr_2MnMoO_6	C	7.98				*Br14*		6
Sr_2FeMoO_6	T	7.888		7.909		*Ga12*	P & S [*Pa7*], Prop. [*Ga12, Na4*], S.S. with Ba and Ca [*Ga12*], neutron diffraction [*Na11*]	6
Sr_2CoMoO_6	T	5.581		7.940		*Ku8*	P & S [*Br14*]	6
	C	7.918				*Ku8*	Cubic at 320 °C; no dielectric anomaly	
Sr_2NiMoO_6	T	5.560		7.886		*Ku8*	P & S [*Br14*], semiconducting, $\Delta E = 0.78$ eV $\leq$ 181 °C $\leq$ 1.30 eV [*No1*], S.S. with Ba, cubic at 22% Ba [*No1, No3*]	6
	C	7.878				*Ku8*	Cubic at 230 °C [*Ku8, No3*], no dielectric anomaly [*Ku8*]	
Sr_2ZnMoO_6	T	5.561		7.966		*Ku8*		
	C	7.954				*Ku8*	Cubic at 420 °C; no dielectric anomaly	

Compound	Sym	a Å	b Å	c Å	angle	Ref.	Remarks	Magnetic Data
$A_2^{2+}BMo^{6+}O_6$ (continued)								in 3.3.4, Tab.
Ca_2CrMoO_6	O	5.36	5.49	7.70		*Pa7*		6
Ca_2FeMoO_6	O	5.42	5.53	7.73		*Pa7*		6
$A_2^{2+}BTe^{6+}O_6$								
Ba_2MgTeO_6	C	8.13				*Sl6*	P&S [*Ba26*, *Re4a*]	
Ba_2CaTeO_6	C	8.393				*Sl6*	P&S [*Ba26*], S.S. with Ni [*Re4a*]	
$BaPbMgTeO_6$	C	8.08				*Ba26*		
Sr_2MgTeO_6	C	7.94				*Ba26*		
$SrPbMgTeO_6$	C	7.955				*Ba26*		
Sr_2NiTeO_6	C	3.95				*Re4a*	Optical properties and S. S. with Ba	
Sr_2CuTeO_6	T	7.680		8.465		*Re4b*	Optical properties	
Ca_2CaTeO_6	O	5.55	5.77	7.98		*Bl1a*		
Pb_2MgTeO_6	C	7.99				*Ba26*		
$A_2^{2+}BW^{6+}O_6$								
Ba_2MgWO_6	C	8.099				*St32*	P&S [*Be18*], dielectric properties [*Ag1*]	
Ba_2CaWO_6	C	8.390				*Be18*	P&S [*St32*], S.S. with Ni [*Re4a*]	
Ba_2CrWO_6						*Pa7*	No perovskite	
Ba_2FeWO_6	C	8.133				*Fr14*		
Ba_2CoWO_6	C	8.098				*Fr14*	P&S [*Br14*], Prop., semiconducting, $\Delta E = 0.81$ eV [*Bo1*], neutron diffraction [*Co31*]	6
Ba_2NiWO_6	C	8.066				*Fr14*	P&S [*Br14*, *Ag1*], S.S. with Sr [*No2*], neutron diffraction [*Co31*], optical properties [*Re4a*]	6
Ba_2CuWO_6	T	7.88		8.61		*Bl8*	P&S [*Ka12*, *Ve2*, *Ve3*], complete structure [*Pl3*]	6
Ba_2ZnWO_6	C	8.116				*Fr14*	P&S [*Be18*]	
Ba_2SrWO_6	C	8.53				*Be18*	P&S [*Fi10*, *St32*], S.S. with Sr_3WO_6 [*Be18*]	
Ba_2CdWO_6	C	8.383				*Be18*		
Ba_2BaWO_6	C	8.62				*St32*	Slightly distorted; cubic $T > 805$ °C [*Ch4*]	
$BaSrMgWO_6$	C	8.02				*Be18*	P&S [*St32*]	
$Ba_{1.5}Ca_{0.5}CaWO_6$	C	8.387				*St32*	P&S [*Be18*]	
$BaSrCaWO_6$	C	8.29				*St32*	Distorted	
$BaCaCaWO_6$	C	8.363				*Be18*	Composition questionable	
$BaSrZnWO_6$	C	8.07				*Be18*	Distorted	
$BaCaZnWO_6$	C	8.38				*Be18*	Composition questionable	
Sr_2MgWO_6	C	7.8				*Be18*	P&S [*St32*], distorted	
Sr_2CaWO_6	C	8.2				*Be18*	Distorted	
Sr_2CrWO_6	C	7.82				*Pa7*		6
Sr_2MnWO_6	C	8.01				*Bl8*	Prop. [*Bl4*]	6
Sr_2FeWO_6	C	7.96				*Bl8*	Prop. [*Bl4*]	6

Compound	Sym	a Å	b Å	c Å	angle	Ref.	Remarks	Magnetic Data
$A_2^{2+}BW^{6+}O_6$ (continued)								in 3.3.4, Tab.
Sr_2CoWO_6	T	7.89		7.98		*Fr14*	P&S [*Br14*], Prop. [*No1, Ku8, Bl2, Bl4*]	6
	C	7.904				*Ku8*	$T \approx 400$ °C, cubic $T > 400$ °C; no dielectric anomaly	
Sr_2NiWO_6	T	7.86		7.91		*Fr14*	P&S [*Br14*], Prop. [*No1, Bl2, Bl4, No2, Ve1, No2, Re4a*], S.S. with $LaFeO_3$ [*Sm23*], S.S. with Ba [*No2*], ESR [*No4*], S.S. with Ca [*Re4a*]	6
	C	7.908				*Ku8*	$T \approx 300$ °C, cubic $T > 300$ °C [*Ku8, No4*]	
Sr_2CuWO_6	T	7.66		8.40		*Bl8*	P&S [*Ka12*], dielectric properties [*Ve2*]	6
Sr_2ZnWO_6	T	7.92		8.01		*Fr14*	P&S [*Ku8, Be18*], S.S. with Ba, cubic > 40% Ba [*Fr14*]	
	C	7.956				*Ku8*	$T \approx 430$ °C, cubic $T > 430$ °C [*Ku8, Fr14*], no dielectric anomaly [*Ku8*]	
Sr_2SrWO_6	C	8.3				*Be18*	Distorted, P&S [*St32*]; cubic $T > 1100$ °C, S.S. with Ca [*Ch3*]	
$SrCaMgWO_6$	C	7.87				*Be18*	Distorted, P&S [*St32*]	
$SrCaCaWO_6$	C	8.1				*Be18*	Distorted, P&S [*St32*]	
Ca_2MgWO_6	C	7.75				*St32*	Distorted, P&S [*Be18*]	
Ca_2CaWO_6	C	8.02				*St32*	Distorted, P&S [*Be18*]; not cubic $T < 1500$ °K, S.S. with Sr [*Ch3, Ch4*]	
Ca_2CrWO_6	O	5.35	5.47	7.70		*Pa7*		6
Ca_2CoWO_6	O	5.43	5.60	7.73		*Bl8*	Prop. [*Bl2, Ki7*]	6
Ca_2NiWO_6	O	5.40	5.55	7.70		*Bl8*	Optical properties [*Re4a*]	
Ca_2CuWO_6							Not perovskite [*Bl8*]	
Pb_2MgWO_6	C	8.0				*Be8*	Dielectric properties [*Sm8, Ag1, Sm13, Kh5, Mi1a, Kh6, St42*], piezoelectric properties, S.S. with Ti, Zr [*St34*], S.S. with Cd [*Is15*], S.S. with $PbFe_{2/3}W_{1/3}O_3$ [*Sm10*], S.S. with $PbTiO_3$, Ca_2MgWO_6, $Pb_3MgNb_2O_9$ [*Sm20, St35*]	
Pb_2CaWO_6	C	4.2				*Be8*	Distorted, dielectric properties [*Ag1*]	
Pb_2MnWO_6	O	5.736	5.756	8.066		*Ve3*	Prop. [*Ve2, Ve4, Ro8*]	6
Pb_2FeWO_6							Prop., no cell dimensions [*Ve4*]	6
Pb_2CoWO_6	O	5.661	5.676	9.976		*Bo10*	P&S [*Fi11, Be18*], Prop. [*Te13, Bo10, Ki7, Fi6*], B site ordering [*Yu9*], S.S. with $BaTiO_3$ [*To2*]	6
	C	8.017				*Fi6*	$T \approx 20$ °C, cubic $T > 20$ °C	
Pb_2NiWO_6	C	7.997				*No6*	Dielectric properties, P&S [*To11a, To11b*]	6
Pb_2NiWO_6	T	8.006		7.920		*No6*	$T = 173$ °K—tetragonal below 290 °K	
Pb_2CdWO_6	C	4.1				*Be18*	Distorted, dielectric properties [*Ro6*], S.S. with Mg [*Is15*]	
Pb_2CdWO_6	C	4.15				*Fi7*	Cubic at 400 °C, transformations [*Po8*], S.S. with Pb $(Li_{1/3}Nb_{1/3}W_{1/3})O_3$ [*Di5*]	

Compound	Sym	*a* Å	*b* Å	*c* Å	angle	Ref.	Remarks	Magnetic Data
$A_2^{2+}BW^{6+}O_6$ (continued)								in 3.3.4, Tab.
$Pb_2Na_{0.5}Sc_{0.5}WO_6$						*Ve4*	Dielectric properties, no cell dimensions	
$Pb_2Na_{0.5}Fe_{0.5}WO_6$						*Ve4*	Dielectric properties, no cell dimensions	
$Pb_2Na_{0.5}Yb_{0.5}WO_6$						*Ve4*	Dielectric properties, no cell dimensions	
$Pb_2Mg_{0.5}Mn_{0.5}WO_6$	T	8.202		8.104		*Vi5*	Dielectric properties [*Vi5, Ve4*]	6
$Pb_2Co_{0.5}Mn_{0.5}WO_6$	T	8.082		8.018		*Vi5*	Dielectric properties [*Vi5, Ve4*]	6
$Pb_2Ni_{0.5}Mn_{0.5}WO_6$							No cell dimensions, Prop. [*Vi5*]	6
$Pb_2Li_{0.5}Fe_{0.5}WO_6$	C	8.008				*Ve3*	Dielectric properties [*Vi5, Ve2, Ve3, Ve4*]	
$Pb_2Li_{0.5}Co_{0.5}WO_6$	C	4.013				*Ve3*	Dielectric properties [*Ve3*]	
$Pb_2Li_{0.5}La_{0.5}WO_6$	C	8.04				*Vi5*	Dielectric properties [*Vi5*]	
$Pb_2Li_{0.5}Yb_{0.5}WO_6$	C	4.100				*Ve3*	Dielectric properties [*Ve2, Ve3, Ve4*]	
$Pb_2Li_{0.33}Mn_{0.67}WO_6$						*Ve4*	Dielectric properties, no cell dimensions	
$Pb_2Li_{0.33}Zr_{0.67}WO_6$						*Ve4*	Dielectric properties, no cell dimensions	
$Pb_2Li_{0.33}Hf_{0.67}WO_6$						*Ve4*	Dielectric properties, no cell dimensions	
$Pb_2YbTi_{0.5}W_{0.5}O_6$	C	4.124				*Ve3*	Dielectric properties [*Ve2, Ve3, Ve4*]	
$Pb_2FeMn_{0.5}W_{0.5}O_6$	C	4.037				*Ro8*	Dielectric properties [*Ve4*]	6
$A_2^{2+}BReO_6$, Re^{5+} and Re^{6+}								
Ba_2MgReO_6	C	8.082				*Sl8*	P&S [*Lo2, Sc18*], single crystal [*Sl7*]	
Ba_2CaReO_6	C	8.356				*Sl8*	P&S [*Lo2, Sc18*]	
Ba_2ScReO_6	C	8.163				*Sl8*	P&S [*Sc18*]	
Ba_2MnReO_6	C	8.18				*Sl8*	P&S [*Lo2, Wa15*], single crystal + Prop. [*Sl7*]	6
Ba_2FeReO_6	C	8.05				*Sl8*	P&S [*Lo2, Wa15*], single crystal + Prop. [*Sl7*], [*Ba25a*] suggests $Ba_2Fe_{1+x}Re_{1-x}O_6$	6
Ba_2CoReO_6	C	8.086				*Sl8*	P&S [*Lo2, Wa15*], single crystal + Prop. [*Sl7*]	6
Ba_2NiReO_6	C	8.04				*Sl8*	P&S [*Lo2*], single crystal + Prop. [*Sl7*]	6
Ba_2ZnReO_6	C	8.106				*Sl8*	P&S [*Lo2*]	
Ba_2SrReO_6	T	8.60		8.43		*Sl8*	P&S [*Sc18*]	
Ba_2YReO_6	C	8.372				*Sl8*		
Ba_2CdReO_6	C	8.322				*Sl8*	P&S [*Lo2*]	
Ba_2InReO_6	C	8.258				*Sl8*	P&S [*Sc18*]	
Ba_2BaReO_6	T	8.65		8.33		*Sl8*	P&S [*Sc18*]	
Ba_2LaReO_6	C	8.547				*Ba25a*	Prep. 900 °C, a_0 increases with prep. temperature suggesting $Ba_2Re^{5+}_{1-x}Re^{6+}_{x}La_{1-x}Ba_xO_6$; P&S [*Sl8*]	
Ba_2NdReO_6	C	8.51				*Sl8*		
Ba_2SmReO_6	C	8.458				*Ba25a*		
Ba_2EuReO_6	C	8.438				*Ba25a*		
Ba_2GdReO_6	C	8.431				*Sl8*	Prop. [*Lo2*], P&S [*Sc18*]	
Ba_2TbReO_6	C	8.399				*Ba25a*		

Compound	Sym	a Å	b Å	c Å	angle	Ref.	Remarks	Magnetic Data
$A_2^{2+}BReO_6$, Re^{5+} and Re^{6+} (continued)								in 3.3.4, Tab.
Ba_2DyReO_6	C	8.391				*Ba25a*		
Ba_2HoReO_6	C	8.375				*Ba25a*		
Ba_2ErReO_6	C	8.354				*Sl8*	Prop. [*Lo2*], P&S [*Sc18*]	
Ba_2TmReO_6	C	8.342				*Ba25a*		
Ba_2YbReO_6	C	8.329				*Ba25a*		
$Ba_{2-x}Sr_xYbReO_6$	C	8.230				*Ba25a*	$x = 1.2$, small positive deviation from Vegard's law	
$BaSrFeReO_6$							Prop. [*Sl8, Lo2*]	
Ba_2YReO_6							Single crystal [*Sl7*], Prep. [*Sc18*]	
Sr_2MgReO_6	T	7.88		7.94		*Sl8*	P&S [*Sc18*]	
Sr_2CaReO_6	O	5.76	5.85	8.21		*Sl8*		
Sr_2ScReO_6	C	8.02				*Sl8*	distorted	6
Sr_2CrReO_6	C	7.82				*Sl8*		
Sr_2MnReO_6	C	8.01				*Sl8*	distorted	6
Sr_2FeReO_6	T	7.86		7.89		*Sl8*	P&S [*Lo2, Wa15*]	
Sr_2CoReO_6	T	7.88		7.98		*Sl8*		
Sr_2NiReO_6	T	7.85		7.92		*Sl8*		
Sr_2ZnReO_6	T	7.89		8.01		*Sl8*		
Sr_2GaReO_6	C	7.843				*Sl8*		
Sr_2SrReO_6	T	8.41		8.13		*Sl8*	P&S [*Sc18*]	
Sr_2YReO_6	C	8.197				*Ba25b*		
Sr_2CdReO_6	O	5.73	5.81	8.16		*Sl8*		
Sr_2InReO_6	C	8.071				*Sl8*		
Sr_2GdReO_6	C	8.239				*Ba25b*		
Sr_2TbReO_6	C	8.223				*Ba25b*		6
Sr_2DyReO_6	C	8.210				*Ba25b*		6
Sr_2HoReO_6	C	8.200				*Ba25b*		
Sr_2ErReO_6	C	8.181				*Ba25b*		6
Sr_2TmReO_6	C	8.167				*Ba25b*		
Sr_2YbReO_6	C	8.155				*Ba25b*		6
Ca_2MgReO_6	O	5.48	5.56	7.77		*Sl8*	P&S [*Sc18*]	
Ca_2CaReO_6	O	5.67	5.78	8.05		*Sl8*	P&S [*Sc18*]	
Ca_2ScReO_6	O	5.49	5.63	7.86		*Sl8*		
Ca_2CrReO_6	O	5.38	5.47	7.67		*Sl8*		6
Ca_2MnReO_6	O	5.52	5.55	7.82		*Sl8*		
Ca_2FeReO_6	O	5.41	5.53	7.69		*Sl8*	P&S [*Lo2*]	6
Ca_2CoReO_6	O	5.46	5.58	7.71		*Sl8*		

Compound	Sym	*a* Å	*b* Å	*c* Å	angle	Ref.	Remarks	Magnetic Data
$A_2^{2+}BReO_6$, Re^{5+} and Re^{6+} (continued)								in 3.3.4, Tab.
Ca_2NiReO_6	O	5.45	5.55	7.67		*Sl8*		
Ca_2CdReO_6	O	5.64	5.77	7.99		*Sl8*		
Pb_2MnReO_6	O	5.69	5.74	8.024		*Ro8*	Claim Mn^{2+}—Re^{6+}, Prop. [*Ro8*, *Ro11*]	6
Pb_2MnReO_6	O	5.67	5.75	8.008		*Ro8*	Claim Mn^{3+}—Re^{5+}, Prop. [*Ro8*, *Ve4*]	6
$A_2^{2+}BOsO_6$								
Ba_2MgOsO_6	C	8.08				*Sl8*		
Ba_2CaOsO_6	C	8.362				*Sl8*		6
Ba_2ScOsO_6	C	8.152				*Sl8*		
Ba_2MnOsO_6	H	5.82		14.2		*Sl8*	Hex (6L)	
Ba_2FeOsO_6	H	5.76		14.1		*Sl8*	Hex (6L)	
Ba_2ZnOsO_6	C	8.095				*Sl8*		
Ba_2SrOsO_6	T	8.43		8.72		*Sl8*		
Ba_2CdOsO_6	C	8.325				*Sl8*		
Ba_2InOsO_6	C	8.224				*Sl8*		
Ba_2BaOsO_6	T	8.66		8.34		*Sl8*		
Sr_2MgOsO_6	T	7.86		7.92		*Sl8*		
Sr_2CaOsO_6	C	8.21				*Sl8*	Distorted	
Sr_2ScOsO_6	C	8.02				*Sl8*	Distorted	
Sr_2CrOsO_6	C	7.84				*Sl8*		
Sr_2FeOsO_6	C	7.85				*Sl8*	Distorted	
Sr_2CoOsO_6	T	7.86		7.92		*Sl8*		
Sr_2GaOsO_6	C	7.82				*Sl8*		
Sr_2SrOsO_6	T	8.32		8.12		*Sl8*		
Sr_2InOsO_6	C	8.06				*Sl8*		
Ca_2CaOsO_6	O	5.73	5.80	7.87		*Sl8*		
Ca_2CrOsO_6	O	5.38	5.47	7.66		*Sl8*		
Ca_2CoOsO_6	O	5.47	5.59	7.70		*Sl8*		
$A_2^{2+}BUO_6$								
Ba_2BeUO_6	C	8.82				*Aw1*	Doubtful	
Ba_2MgUO_6	C	8.381				*Sl5*		
Ba_2CaUO_6	C	8.67				*Sl5*	Distorted, P&S [*Ru4*]	
Ba_2ScUO_6	C	8.49				*Sl5*		
Ba_2TiUO_6	C	8.05				*Aw1*	Ti^{4+}	
Ba_2CrUO_6	C	8.297				*Sl5*	Also prepared as Hex (6L)	
Ba_2MnUO_6	C	8.52				*Sl5*	P&S [*Aw1*]	
Ba_2FeUO_6	C	8.312				*Sl5*	Prop. [*Di5*]	6
Ba_2CoUO_6	C	8.372				*Sl5*		

Compound	Sym	a Å	b Å	c Å	angle	Ref.	Remarks	Magnetic Data
$A_2^{2+}BUO_6$ (continued)								in 3.3.4, Tab.
Ba_2NiUO_6	C	8.336				*Sl5*	Optical properties [*Re4a*]	
Ba_2CuUO_6	T	8.18		8.84		*Sl5*		
Ba_2ZnUO_6	C	8.397				*Sl5*		
Ba_2GeUO_6	C	8.56				*Aw1*	Doubtful	
Ba_2SrUO_6	C	8.84				*Sl5*	Distorted, P & S [*Ru4*]	
Ba_2YUO_6	C	8.69				*Sl5*	Distorted	
Ba_2ZrUO_6	C	8.35				*Aw1*		
Ba_2RhUO_6	H	5.84		14.9		*Sl5*	Hex (6L)	
Ba_2CdUO_6	O	6.07	6.13	8.64		*Sl5*		
Ba_2InUO_6	C	8.521				*Sl5*		
$Ba_2InUO_{5.5}$	C	8.551				*Sl5*		
Ba_2BaUO_6	T	6.285		8.943		*Ri4*	Complete structure determined, P & S [*Sl5*, *Ru4*]	
Ba_2LaUO_6	C	8.73				*Aw1*	Distorted	
Ba_2CeUO_6	C	8.87				*Aw1*	Ce^{4+}	
Ba_2NdUO_6	C	8.76				*Aw1*		
Ba_2SmUO_6	C	8.76				*Aw1*		
Ba_2EuUO_6	C	8.68				*Aw1*		
Ba_2GdUO_6	C	8.66				*Aw1*		
Ba_2DyUO_6	C	8.65				*Aw1*		
Ba_2HoUO_6	C	8.65				*Aw1*		
Ba_2ErUO_6	C	8.67				*Aw1*	Distorted	
Ba_2YbUO_6	C	8.60				*Aw1*		
Ba_2LuUO_6	C	8.57				*Aw1*		
Ba_2HfUO_6	C	8.31				*Aw1*		
Ba_2HgUO_6	C	8.83				*Aw1*	Doubtful	
Ba_2PbUO_6	C	8.85				*Aw1*	Doubtful	
$BaSrSrUO_6$	C	8.66				*Ru4*		
Sr_2MgUO_6	C	8.19				*Sl5*	Distorted	
Sr_2CaUO_6	O	5.93	6.06	8.46		*Sl5*		
Sr_2CrUO_6	C	8.09				*Sl5*	Distorted	
Sr_2MnUO_6	C	8.28				*Sl5*	Distorted	
Sr_2FeUO_6	C	8.11				*Sl5*	Distorted	6
Sr_2CoUO_6	C	8.19				*Sl5*	Distorted	
Sr_2NiUO_6	C	8.15				*Sl5*	Distorted, optical properties [*Re4a*]	
Sr_2SrUO_6	M	5.959	6.179	8.553	$\beta = 90° 11'$	*Ri4*	Complete structure; P & S [*Sl5*, *Ru4*, *Be25*, *Ip1*]	
Sr_2CdUO_6	O	5.91	6.03	8.42		*Sl5*		
Sr_2InUO_6	C	8.33				*Sl5*	Distorted; Prop. [*Ke13*]	6
$SrCaCaUO_6$	O	5.83	6.01	8.36		*Sl5*		

Compound	Sym	a	b	c	angle	Ref.	Remarks	Magnetic Data	Ref.

Compound	Sym	*a* Å	*b* Å	*c* Å	angle	Ref.	Remarks	Magnetic Data
$A_2^{2+}BUO_6$ (continued)								in 3.3.4, Tab.
Ca_2CaUO_6	M	5.728	5.958	8.301	$\beta = 90° 33'$	*Ri4*	Complete structure determined, P&S [*Sl5*, *Ru4*, *Be25*, *Ip1*]	
Pb_2PbUO_6	O	13.71	12.36	8.21		*St26*	Not perovskite	
$A_2^{2+}BB'O_6$; B' = Np^{6+}, Pu^{6+}								
Ba_2SrNpO_6	C	8.799				*Ke4*		
Ba_2BaNpO_6	C	8.860				*Ke4*		
$BaSrSrNpO_6$	C	8.735				*Ke4*		
Ba_2SrPuO_6	C	8.780				*Ke3*		
Ba_2BaPuO_6	C	8.840				*Ke3*		
$BaSrSrPuO_6$	C	8.717				*Ke3*		
Sr_2SrPuO_6						*Ke3*	Not perovskite	
$A_2^{2+}B^+B'O_6$; B' = Tc^{7+}, Re^{7+}, Os^{7+}, I^{7+}								
Ba_2LiTcO_6	C	8.092				*Wa16*	P&S [*Ke9*]	
Ba_2NaTcO_6	C	8.292				*Wa16*	P&S [*Ke9*]	
Sr_2LiTcO_6	C	7.84				*Wa16*	Distorted, P&S [*Ke9*]	
Sr_2NaTcO_6	T	8.09		8.14		*Wa16*	P&S [*Ke9*]	
Ca_2LiTcO_6							Not able to be made [*Wa16*]	
Ba_2LiReO_6	C	8.118				*Sl4*	S.S. with Na [*Sl4*]	
Ba_2NaReO_6	C	8.296				*Sl4*		
Sr_2LiReO_6	C	7.87				*Sl8*		
Sr_2NaReO_6	C	8.13				*Sl8*		
Ca_2LiReO_6	C	7.83				*Sl8*	Distorted	
Ba_2LiOsO_6	C	8.100				*Sl8*	S.S. with Re [*Sl8*]	6
Ba_2NaOsO_6		8.282				*Sl8*		
Sr_2LiOsO_6	C	7.86				*Sl8*		
Sr_2NaOsO_6	C	8.13				*Sl8*		
Ca_2LiOsO_6	C	7.83				*Sl8*	Distorted	
Ba_2NaIO_6	C	8.33				*Sl6*		
Ba_2AgIO_6	C	8.46				*Sl6*		

Tab. 2c. $A_3BB'_2O_9$ (for H symmetry see Fig. 1c)

Compound	Sym	*a* Å	*b* Å	*c* Å	angle	Ref.	Remarks	Magnetic Data
$A_3BB'^{5+}_2O_9$								in 3.3.4, Tab.
$Ba_3MgNb_2O_9$	H	5.77		7.08		*Ga9*	P&S [*Ga13*, *Bl8*], see Fig. 1 (c)	
$Ba_3CaNb_2O_9$	H	5.92		7.25		*Ga9*	See Fig. 1 (c)	
$Ba_3FeNb_2O_9$	C	4.085				*Ga9*		
$Ba_3CoNb_2O_9$	C	4.09				*Ga13*		
$Ba_3NiNb_2O_9$	C	4.074				*Ga9*	P&S [*Ro20*, *Ag1*], dielectric properties [*Sm8*], optical properties [*Re4a*]	
$Ba_3CuNb_2O_9$	T	8.04		8.40		*Bl8*	Dielectric properties [*Ka12*, *Ve3*]	
	C	8.166				*Ve2*	Cubic > 653 °K	
$Ba_3ZnNb_2O_9$	C	4.094				*Ga9*	P&S [*Ga13*, *Ag1*]	
$Ba_3CdNb_2O_9$	C	4.168				*Ga9*		
$Ba_3BaNb_2O_9$	H	6.01		8.0		*Ga9*	P&S [*Bl8*], see Fig. 1 (c)	
$Ba_3PbNb_2O_9$	C	4.26				*Ga9*		
$Sr_3MgNb_2O_9$	H	5.66		6.98		*Ga9*	See Fig. 1 (c)	
$Sr_3CaNb_2O_9$	H	5.76		7.16		*Ga9*	See Fig. 1 (c)	
$Sr_3FeNb_2O_9$	T	3.997		4.018		*Ga9*		
$Sr_3CoNb_2O_9$	C	8.01				*Bl8*		
$Sr_3NiNb_2O_9$	H	5.64		6.90		*Ga9*	P&S [*Ag1*], optical properties of S.S. with Ba and Ca [*Re4a*], see Fig. 1 (c)	
$Sr_3CuNb_2O_9$	T	7.888		8.148		*Ka12*	Prop. [*Ve2*]	
$Sr_3ZnNb_2O_9$	H	5.66		6.95		*Ga9*	P&S [*Ga13*], see Fig. 1 (c)	
$Sr_3CdNb_2O_9$	C	4.089				*Ga9*		
$Ca_3CaNb_2O_9$						*Bl8*	Distorted perovskite	
$Ca_3NiNb_2O_9$	C	3.88				*Ag1*		
$Pb_3MgNb_2O_9$	C	4.04				*Ag1*	Dielectric properties [*Sm27*, *Ag1*, *Ou1*, *Ou1a*, *Ou2*, *Bo5*, *Is4*, *Bo16*, *Be23*, *Kh5*, *Kh4*, *Kh8*, *Sm14*, *Sm20*, *Sm29*, *Sm8*, *Cr6b*], crystal growth [*Ba5*, *My3*], electrooptic effect [*Sm29*]	
$Pb_3MnNb_2O_9$						*Ag1*	No cell dimensions	
$Pb_3CoNb_2O_9$	C	4.05				*Bo5*	Dielectric properties [*Bo5*, *Ag1*]	
$Pb_3NiNb_2O_9$	C	4.02				*Ag1*	Dielectric properties [*Ag1*, *Sm8*, *Bo5*, *Is4*], crystal growth [*Bo5*, *My3*], S.S. with Mg [*Sm20*, *Sm27*, *Sm14*, *Is4*, *Cr6b*], S.S. with Pb(Ti, Zr)O_3 [*Bu10*], electrooptic effect [*Sm29a*]	
$Pb_3ZnNb_2O_9$	C	4.05				*Bo5*	Dielectric properties [*Bo5*, *Kh7*, *Be23a*]	
$Pb_3Sc_{5/3}W_{1/3}NbO_9$	C	4.074				*To1*	Dielectric properties [*Ve4*]	
$Pb_3CdNb_2O_9$	C	8.246				*To1*	Dielectric properties [*Ve2*, *Ve3*, *Ve4*]	

Compound	Sym	a Å	b Å	c Å	angle	Ref.	Remarks	Magnetic Data
$A_3BB_2^{5+}O_9$ (continued)								in 3.3.4, Tab.
$Ba_3MgRu_2O_9$	H					*Ca2*	Hex (6L), magnetic properties $84 < T < 948$ °K, $\Theta_N = 390$ °K [*Ca2*]	
$Ba_3MgSb_2O_9$	H	5.83		14.26		*Bl8*	Hex (6L)	
$Ba_3CaSb_2O_9$	H	5.99		14.84		*Bl8*	Hex (6L)	
$Ba_3CoSb_2O_9$	H	5.84		14.35		*Bl8*	Hex (6L)	
$Ba_3NiSb_2O_9$	H	5.82		14.25		*Bl8*	Hex (6L), optical properties of S.S. with Sr and Nb [*Re4a*]	
$Ba_3CuSb_2O_9$	H	5.82		14.22		*Bl8*	Hex (6L)	
$Ba_3SrSb_2O_9$	H	6.15		15.6		*Bl8*	Hex (6L)	
$Ba_3BaSb_2O_9$	H	6.09		15.9		*Bl8*	Hex (6L)	
$Sr_3MgSb_2O_9$	C	7.96				*Bl8*		
$Sr_3CaSb_2O_9$	C	8.17				*Bl8*		
$Sr_3CoSb_2O_9$	C	7.99				*Bl8*		
$Sr_3NiSb_2O_9$	C	3.98				*Re4a*	Cell probably doubled, optical properties [*Re4a*]	
$Sr_3CuSb_2O_9$	T	7.84		8.19		*Bl8*	Optical properties [*Re4b*]	
$Sr_3SrSb_2O_9$	O	5.78	5.80	8.34		*Bl8*		
$Sr_3La_{0.5}Li_{0.5}Sb_2O_9$	O	5.62	5.68	8.00		*Bl8*		
$Ba_3MgTa_2O_9$	H	5.782		7.067		*Ga10*	Crystal growth [*Ga7*], see Fig. 1 (c)	
$Ba_3CaTa_2O_9$	H	5.895		7.284		*Ga10*	P & S [*Ga8*], crystal growth [*Ga7*], see Fig. 1 (c)	
$Ba_3MnTa_2O_9$	H	5.819		7.127		*Ga10*	See Fig. 1 (c)	
$Ba_3FeTa_2O_9$	C	4.10				*Ga13*		
$Ba_3CoTa_2O_9$	H	5.776		7.082		*Ga10*	P & S [*Ro20*], see Fig. 1 (c)	
$Ba_3NiTa_2O_9$	H	5.758		7.052		*Ga10*	P & S [*Ro20*], crystal growth [*Ga7*], optical properties [*Re4a*], see Fig. 1 (c)	
$Ba_3CuTa_2O_9$	T	8.132		8.432		*Ka12*	P, S + Prop. [*Ve2, Ve3*]	
$Ba_3ZnTa_2O_9$	H	5.782		7.097		*Ga10*	P & S [*Ga13*], crystal growth [*Ga7*], see Fig. 1 (c)	
$Ba_3SrTa_2O_9$	H	5.95		7.47		*Ga11*	P & S [*Ga13*], see Fig. 1 (c)	
$Ba_3CdTa_2O_9$	C	4.167				*Ga10*		
$Ba_3BaTa_2O_9$	H	6.10		8.05		*Bl8*	See Fig. 1 (c)	
$Ba_3PbTa_2O_9$	C	4.250				*Ga10*		
$Ba_3Zn_{0.5}Ni_{0.5}Ta_2O_9$	C	4.08				*Ga13*		
$Sr_3MgTa_2O_9$	H	5.652		6.951		*Ga10*	P & S [*Ro20*], see Fig. 1 (c)	
$Sr_3CaTa_2O_9$	H	5.764		7.096		*Ga10*	See Fig. 1 (c)	
$Sr_3CoTa_2O_9$	H	5.630		6.937		*Ga10*	P & S [*Ga13*], see Fig. 1 (c)	
$Sr_3NiTa_2O_9$	H	5.607		6.923		*Ga10*	P & S [*Ga13*], see Fig. 1 (c)	
$Sr_3CuTa_2O_9$	T	7.860		8.248		*Ka12*	P, S + Prop. [*Ve2, Ve3*]	
$Sr_3ZnTa_2O_9$	H	5.664		6.951		*Ga10*	P & S [*Ga13*], see Fig. 1 (c)	
$Pb_3MgTa_2O_9$	C	4.03				*Bo5*	Prep. [*Ag1*], electrooptic effect [*Sm29a*]	
$Pb_3CoTa_2O_9$	C	4.02				*Bo5*		
$Pb_3NiTa_2O_9$	C	4.02				*Bo5*	Prep. [*Ag1*]	

Compound	Sym	a Å	b Å	c Å	angle	Ref.	Remarks	Magnetic Data
$La_3Co_2B^{5+}O_9$								in 3.3.4, Tab.
$La_3Co_2NbO_9$	O	5.58	5.58	7.89		*Bl8*		
$La_3Co_2SbO_9$	O	5.57	5.57	7.87		*Bl8*		
$A_3B_2B^{6+}O_9$								
$Ba_3Cr_2MoO_9$	H	5.72		14.02		*Pa7*	Hex (6L)	
$Ba_3Fe_2MoO_9$	H	5.74		14.08		*Bl8*	Hex (6L)	
$Ba_3In_2MoO_9$	C	4.168				*Ka12*		
$Ba_3Bi_2MoO_9$	O	6.148	6.184	8.642		*Ve2*	P&S [*Vi3*, *Ve3*], dielectric properties [*Vi2b*]	
	C	4.37				*Vi2b*	$T > 500$ °C	
$Ba_3LiNbMoO_9$	R	4.091			$\alpha = 89° 50'$	*Ka12*		
$Ba_3LiTaMoO_9$	C	4.090				*Ka12*		
$Pb_3Bi_2MoO_9$	T	11.262		11.452		*Vi3*	Defect pyrochlore type	
$Ba_3Sc_2WO_9$	C	8.24				*Fr14*	P&S [*Ga15*], dielectric properties [*Ka12*]	
$Ba_3Cr_2WO_9$	H	5.75		14.35		*Pa7*	Hex (6L)	
$Ba_3Fe_2WO_9$	H	5.74		14.08		*Bl8*	Hex (6L)	
$Ba_3Co_2WO_9$	H	5.74		14.10		*Bl8*	Hex (6L)	
$Ba_3Y_2WO_9$	C	8.374				*Ga15*		
$Ba_3Rh_2WO_9$	H	5.74		14.15		*Bl8*	Hex (6L)	
$Ba_3In_2WO_9$	C	8.321				*Ga15*	Structure + Prop. [*Ka12*]	
$Ba_3La_2WO_9$	C	8.58				*Bl8*		
$Ba_3Nd_2WO_9$	C	8.513				*Ga15*		
$Ba_3Eu_2WO_9$	C	8.605				*Ga15*		
$Ba_3Gd_2WO_9$	C	8.411				*Ga15*	P&S [*Bl8*]	
$Ba_3Dy_2WO_9$	C	8.386				*Ga15*	Structure + Prop. [*Ka12*]	
$Ba_3Ho_2WO_9$	C	4.252				*Ka12*	Probably ordered	
$Ba_3Er_2WO_9$	C	8.386				*Ga15*		
$Ba_3Yb_2WO_9$						*Ga15*	No cell dimensions	
$Ba_3Lu_2WO_9$						*Ga15*	No cell dimensions	
$Ba_3Bi_2WO_9$	R	6.131			$\alpha = 60° 23'$	*Ve2*	Dielectric properties [*Vi3*, *Ve3*, *Vi2b*]	
$Ba_3LiNbWO_9$	R	4.098			$\alpha = 89° 52'$	*Ka12*		
$Ba_3LiTaWO_9$	R	4.095			$\alpha = 89° 53'$	*Ka12*		
$Sr_3Fe_2WO_9$	T	3.945		3.951		*Ga15*	P&S [*Bl8*], S.S. with $Sr_3Fe_2UO_9$ [*Se6a*]	
$SrLa_2Mg_2WO_9$	C	7.91				*Bl8*		
$SrLa_2Co_2WO_9$	C	7.90				*Bl8*		
$Pb_3Sc_2WO_9$	C	8.134				*Ve3*	Dielectric properties [*Ve4*, *Ve2*, *Ve3*, *To1*]	
$Pb_3Mn_2WO_9$						*Ro8*	No cell dimensions, Prop. [*Ve4*, *Ro8*], S.S. with $PbTiO_3$ [*Di5a*]	6
$Pb_3Fe_2WO_9$	C	4.02				*Ro8*	Prop. [*Ag1*, *Ro8*, *Sm10*, *Sm16*, *Sm28*, *To5*, *To11*, *Te13*, *Pl1*, *Ki6*], *B* site ordering [*Yu9*]	6
$Pb_3Bi_2WO_9$	T	10.637		10.799		*Vi3*	Defect pyrochlore type	

$Pb_3Bi_2WO_9$	I	10.057		10.799		P43	Defect pyrochlore type	

Compound	Sym	a Å	b Å	c Å	angle	Ref.	Remarks	Magnetic Data
$A_3B_2B^{6+}O_9$ (continued)								in 3.3.4, Tab.
$Pb_3ScMnWO_9$						*Ve4*	No cell dimensions	
$Pb_3CrMnWO_9$						*Ve4*	No cell dimensions	6
$Pb_3FeMnWO_9$						*Ve4*	No cell dimensions	6
$Pb_3CdMnWO_9$	O	5.80	5.90	8.138		*Ro8*	Prop. [*Ve4, Ro8*]	6
$Pb_3CoFeWO_9$						*Ve4*	No cell dimensions	6
$Pb_3LiNbWO_9$	C	8.090				*Vi5*	Dielectric properties [*Ve2, Ve4, Vi5*]	
$Pb_3Cd_{4/3}Nb_{2/3}WO_9$	O	5.813	5.877	8.178		*To1*	Dielectric properties [*Ve2, Ve4*]	
$Ba_3Cr_2ReO_9$	H	5.70		13.8		*Sl8*	Hex (6L)	
$Ba_3Fe_2ReO_9$	H	5.81		14.10		*Sl8*	Hex (6L)	
$Sr_3Cr_2ReO_9$	C	8.015				*Sl8*		
$Sr_3Fe_2ReO_9$	C	7.890				*Sl8*		
$Sr_3In_2ReO_9$	C	8.297				*Sl8*		
$Ba_3Sc_2UO_9$	C	8.49				*Sl5*		
$Ba_3Cr_2UO_9$	H	5.82		14.6		*Sl5*	Hex (6L)	
$Ba_3Fe_2UO_9$	C	8.232				*Sl5*	P&S [*Ro14*]	
$Ba_3Y_2UO_9$	C	8.70				*Sl5*	Slight distortion	
$Ba_3In_2UO_9$	C	8.512				*Sl5*		
$Sr_3Cr_2UO_9$	C	8.00				*Sl5*		
$Sr_3Fe_2UO_9$	C	8.066				*Ro14*	Prop. [*Be51*], S.S. with $Sr_3Fe_2WO_9$ [*Se6a*]	6

Tab. 2d. $A^{2+}(B_xB'_yB''_z)O_3$

Compound	Sym	a Å	b Å	c Å	angle	Ref.	Remarks	Magnetic Data
$Ba[Zn_{0.2}Fe_{0.2}Nb_{0.6}]O_3$	C	4.08				*Ga13*		
$Ba[Zn_{0.2}Fe_{0.2}Ta_{0.6}]O_3$	C	4.08				*Ga13*		
$Sr[Zn_{0.2}Fe_{0.2}Ta_{0.6}]O_3$	C	4.01				*Ga13*		
$Ba[Li_{0.25}Nb_{0.75}]O_3$	C	4.095				*Ka12*		
$Ba[Na_{0.25}Nb_{0.75}]O_3$	C	4.107				*Ka12*		
$Ba[Na_{0.25}Ta_{0.75}]O_3$	C	4.137				*Ga6*		
$Sr[Na_{0.25}Ta_{0.75}]O_3$	C	4.055				*Ga6*		
$Ba[Fe_{0.75}Nb_{0.25}]O_{2.75}$	C	4.07				*Ga13*		
$Ba[Fe_{0.75}Ta_{0.25}]O_{2.75}$	C	4.07				*Ga13*		
$Sr[Fe_{0.7}Nb_{0.3}]O_{2.8}$	C	3.96				*Ga13*		
$Ba[Fe_{1/7}Fe_{2/7}Ta_{4/7}]O_3$	C	4.08				*Ga13*		
$Ba[Co_{1/7}Co_{2/7}Ta_{4/7}]O_3$	C	4.09				*Ga13*		
$Sr[Co_{1/7}Co_{2/7}Ta_{4/7}]O_3$	C	4.00				*Ga13*		
$Ba[Na_{0.4}W_{0.6}]O_3$	C	4.158				*Ka12*		

3.2 Descriptions of perovskite-related structures

3.2.1 A-cation vacancies

3.2.1.1 No A cations

Because a skeleton of shared-corner octahedra is stable, it is possible to remove all the A cations from the perovskite structure without collapsing the BX_3 subarray. In the case of □ **ReO_3** for example, the structure remains cubic. However, a partial or a complete collapse of the skeleton is found in many □ BX_3 compounds. The completely collapsed structure has hexagonal-close-packed X layers with one-third of the octahedral sites occupied by B atoms, as indicated in Fig. 19. This results in a simple-cubic array of B cations with corner-shared octahedra having a B-X-B angle of 132°. For comparison, Fig. 19 also shows the corner-shared octahedra across a close-packed □ X_3 plane of the cubic □ **ReO_3** structure, where the B-X-B angle is 180°. It is possible to go from one structure to the other by a simple increase of the B-X-B angle, the B cations forming a simple-cubic array in all structures. In the partially collapsed structure, represented by **CrF_3**, and B-X-B angle is intermediate, ≈ 150°. Trifluorides of the first-row transition metals have the partially collapsed structure, those of the second- and third-row transition metals have the **ReO_3** structure where the number of outer d electrons per cation is $\leqq 3$, but the completely collapsed structure where it is $\geqq 6$. The B cations of the latter group either have no atomic moment (Rh^{III} and Ir^{III} have $t_{2g}^6 e_g^0$) or disproportionate into magnetic and nonmagnetic ions (Pd^{2+}, $t_{2g}^6 e_g^2$ and Pd^{IV}, $t_{2g}^6 e_g^0$), so that there are no magnetic interactions between neighboring cations. The other trifluorides, on the other hand, are all antiferromagnetic, and coupling between like atoms of the second and third long periods is stronger than that between like atoms of the first long period. Since the B-X-B superexchange interaction is enhanced by a larger B-X-B angle, it is reasonable to assume that the interactions between neighboring B cations stabilizes the **ReO_3** structure. These interactions may be either weaker interactions between localized electrons, as in the magnetic fluorides, or stronger interactions, as in metallic **ReO_3**. In this connection, stabilization of the cubic structure in the tungsten bronzes $A_x^{+m}WO_3$ for $mx > 0.3$ is significant. The conduction electrons introduce cation-anion-cation interactions while simultaneously reducing the energy gained by a ferroelectric distortion.

Electron-ordering distortions may be superposed on the array of corner-shared octahedra. **MnF_3**, for example, exhibits the Jahn-Teller distortions shown in Fig. 10(a) superposed on the partially collapsed structure. **WO_3**, on the other hand, exhibits several low-temperature phases characteristic of an interplay of antiferroelectric distortions and different degrees of the collapse of the B-X-B angle.

3.2.1.2 The bronze structures

Although □ BX_3 compounds with the **ReO_3** structure and cubic ABX_3 compounds have the same BX_3 array, complete solid solutions $□_xA_{1-x}BX_3$, $0 \leqq x \leqq 1$, are not possible. Although there is no ordering of the vacancies for larger x, except for **$Na_{0.75}WO_3$** [*Atl*], for smaller x there is ordering accompanied by a collapse of the BX_3 array within basal planes perpendicular to a unique axis. Such a collapse creates the tetragonal and hexagonal tunnel structures of Fig. 20. The tetragonal structure contains three types of tunnels, one containing cubic, twelve-coordinated A' sites, one containing pentagonal-prism, fifteen-coordinated A'' sites, and one small tunnel containing nine-coordinated A''' sites, which are only occupied by Li^+ ions. Without Li^+ ions, all these sites are filled at $A'_{0.2}A''_{0.4}BX_3$. This phase, which may occur for a

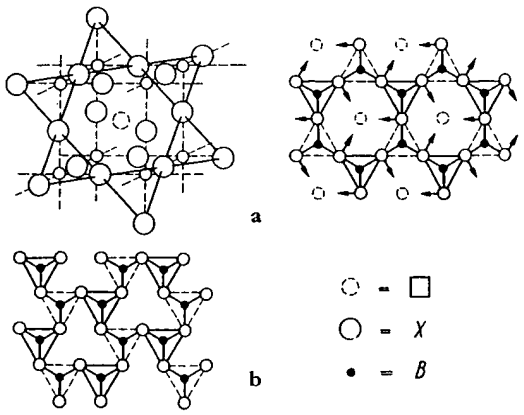

Fig. 19. Projections on B-cation planes of two □BX_3 structures. Triangles in full and dotted lines represent faces of octahedra below or above the B-cation plane. a) Cubic □ReO_3 structure DO_9. Arrows indicate cooperative atomic motions that collapse the structure. b) Completely collapsed □RhF_3 structure.

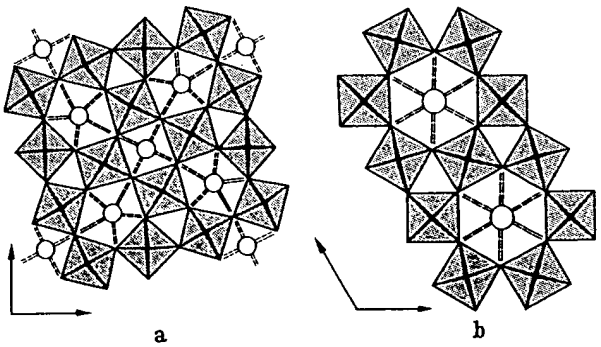

Fig. 20. Bronze structures found in $A_x□_{1-x}BX_3$ systems. a) Tetragonal (II) structure occurring for $x \leqq 0.6$. b) Hexagonal structure occurring for $x \leqq 0.33$ [*Wal*].

range of $x \leq 0.6$, is labelled tetragonal (II) in Tab. 3 to distinguish it from the antiferroelectric tetragonal (I) phase of WO_3. The hexagonal structure contains hexagonal-prism, eighteen-coordinated A sites and is restricted to the range of composition $x \leq 0.33$. An orthorhombic tunnel structure has also been identified for AB_2O_6 compounds [*Ga15a*].

Tab. 3. Color vs. x for Na_xWO_3 and compositional ranges for the bronze structures in the $A_x^{1+}WO_3$ perovskites. Adapted from [*Di3*]

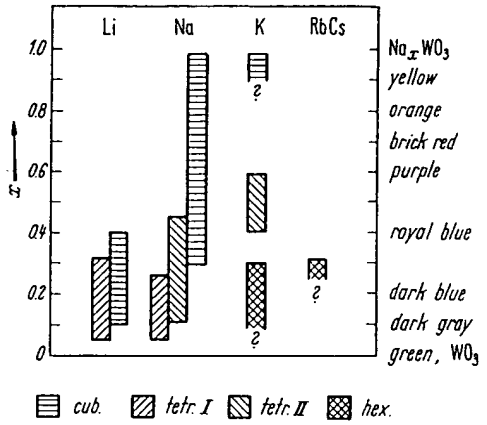

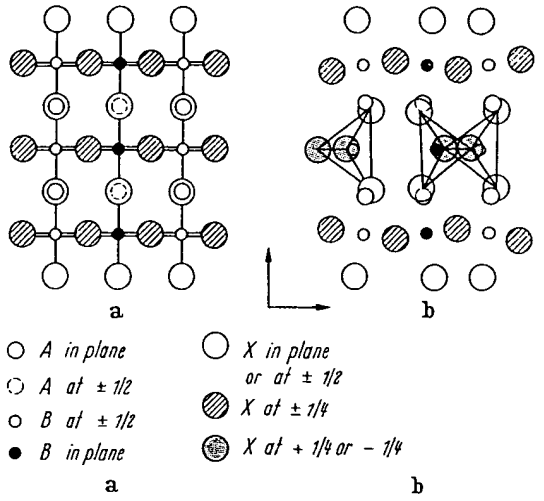

Fig. 21. Projections onto (110) planes of a) cubic perovskite and b) brownmillerite structures. Brownmillerite structure is formed by removing alternate [110] strings of oxygen from central row of a) and regrouping remaining oxygen into the tetrahedra shown in b) [*Wa1*].

3.2.2 Anion-deficient compounds

3.2.2.1 Compounds ABX_{3-x}

Several systems ABX_{3-x}, where $0 \leq x \leq 0.5$, have been reported as anion-deficient perovskites. $SrTiO_{2.5}$ and $SrVO_{2.5}$, for example, both give simple x-ray powder patterns in qualitative agreement with the assumption of a perovskite structure having one-sixth of the anions missing at random. Further, the homogeneity range of $SrTiO_{3-x}$ is reported [*Wa1*] to extend over $0 \leq x \leq 0.5$ without any change of lattice parameter. However, if an anion is removed from a close packed structure, the metal atoms to which it was formerly bonded will have highly unsymmetrical coordination, and some local rearrangement of the anion can be expected. The nature of this local rearrangement depends upon the character of the B cation. In order to learn what rearrangements may occur locally, it is necessary to examine those special cases where long-range order occurs, since local changes of cation coordination are difficult to detect by x-ray diffraction and have not been investigated by other methods.

In the system $SrFe^{3+}_{2x}Fe^{4+}_{1-2x}O_{3-x}$, $0 \leq x \leq 0.5$, it is known that the Fe^{3+} ions are stable in either tetrahedral or octahedral coordination. Therefore, it is reasonable to anticipate the creation of fourfould coordination about half of the Fe^{3+} ions in the system. This is possible because the d electrons of Fe^{3+} ions are localized, so that Fe^{3+} and Fe^{4+} ions are distinguishable, even though the d electrons of the end member $SrFe^{4+}O_3$ appear to be collective. Support for the creation of tetrahedral sites, as well as a suggestion of how the tetrahedra might be arranged, is given by $Ca_2Fe_2O_5$, which has the brownmillerite structure [*Be41*] of Fig. 21. Within every other (001) BX_2 plane of the cubic perovskite, alternate [110] rows of anions are removed. The remaining anions in these planes are displaced alternately along $[1\bar{1}0]$ and $[\bar{1}10]$ directions toward the anion vacancies, the B cations shifting slightly also to maintain equal B-X distances with all four near-neighbor anions. The result is fourfold coordination for all B cations in these (001) BX planes, sixfold coordination for all B cations in the alternate (001) BX_2 planes.

The x-ray pattern of $K_2Ti_2O_5$ has a strong resemblance to that of perovskite. However, $KTiO_{2.5}$ is not an anion-deficient perovskite, but is completely ordered, each Ti^{4+} ion having five oxygen near neighbors forming a trigonal bipyramid [*An3*]. It has little similarity to perovskite.

The oxygen-deficient, tetragonal compounds $(Ba_{2x}Bi_{1-2x})BiO_{3-x}$, $0.22 < x < 0.5$, retain an octahedral grouping for Bi in the B sites, but the A positions have only six oxygen near neighbors, two each at 2.7, 3.1 and 3.6 Å [*Au1*].

These examples indicate that a variety of orderings must occur in anion-deficient perovskites. Further structural work needs to be done.

3.2.2.2 Alloys $M^cX_{1-x}M^f_3$

Since the alloys $M^cXM^f_3$ are generally considered to represent interstitial X atoms in an ordered, face-centered-cubic $M^cM^f_3$ alloy, it is not surprising that the phase is stable over a considerable range of anion deficiency. Since these alloys are metallic, it is probable that the X-atom vacancies are randomly distributed.

3.2.2.3 Shear structures $\square BO_{3-x}$

Ranges of composition have been reported for BO_{3-x}, where B = Mo or W. MAGNÉLI [*Ma14*] has shown that these compositional ranges consist of a series of discrete phases having an x-ray diffraction pattern dominated by a cubic $\square$ **ReO_3**-type (DO_9) subcell, but exhibiting superlattice lines. The superlattice of any discrete phase is not due to an ordering of anion vacancies within this basic structure, but to a regular interruption of the DO_9 structure by planes of discontinuity across which octahedra share edges rather than corners. In these structures the oxygen vacancies condense into regularly spaced planes and are then eliminated by a shear displacement of the type shown schematically in Fig. 22. These "shear" planes may be constituted in different ways: For the series of phases B_nO_{3n-2}, six octahedra in a group share edges, and for the phases B_nO_{3n-1} groups of four octahedra share edges. In both cases the discontinuities continue in two dimensions throughout the structure where they separate DO_9 blocks n octahedra thick. The β-**WO_{3-x}** phases, $0.10 \leq x \leq 0.17$, belong to the series B_nO_{3n-2} with $12 < n \leq 20$. The observed compositional range **(W, Mo)O_{3-x}**, $0.07 \leq x \leq 0.12$, contains six discrete B_nO_{3n-1} phases corresponding to $n = 8, 9, 10, 11, 12$, and 14 [*Ma17a*]. The origin of the shear planes appears to be an interplay between electrostatic and elastic forces: Electrostatic repulsive energies between B cations sharing common octahedral-site edges is minimized by cationic displacements (of ferroelectric type) away from the center of symmetry of the interstice and the shared octahedral edge. These displacements can be cooperative, costing a minimum of elastic energy, if the shared edges are coplanar. The origin of the regular spacing between planes is not established. Presumably it is primarily due to elastic energy, although collective-electron effects [*Go11*] probably play a contributing role.

3.2.3 Structures deficient in B cations

3.2.3.1 Bismuth compounds

Bismuth compounds with chemical formula $(Bi_2A_{m-2})B_{m-1}O_{3m}$ have the structural formula $(Bi_2O_2)^{2+}(A_{n-1}B_nO_{3n+1})^{2-}$, $n = m - 1$. These compounds consist of a regular intergrowth of the perovskite structure with **Bi_2O_2** sheets consisting of **BiO_4** square pyramids sharing edges [*Au2*], as indicated in Fig. 23. Between the **Bi_2O_2** sheets are n layers of corner-shared octahedra and $(n - 1)$ layers of perovskite-type A cations in the twelve-coordinated interstices. Where $n = 1$, the pyramidal sheets alternate with

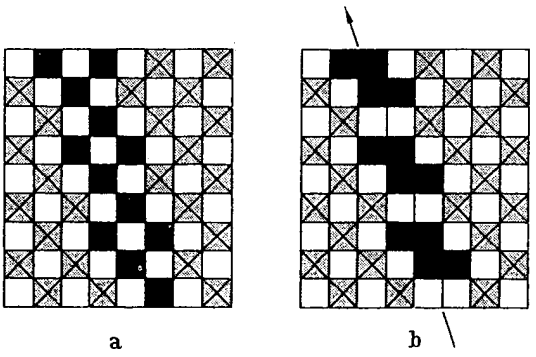

Fig. 22. Projection onto (001) planes of a) cubic $\square ReO_3$ structure and b) B_nO_{3n-1} shear plane. Anions are removed from black octahedra, which then move to adjacent positions to form configuration b) [*Wa1*].

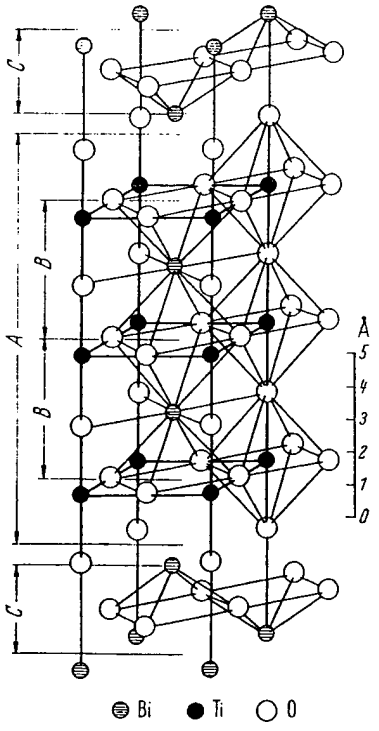

Fig. 23. One half of the pseudo-tetragonal unit cell of $Bi_4Ti_3O_{12}$ (from $z \approx 0.25$ to $z \approx 0.75$). A denotes the perovskite layer $(Bi_2Ti_3O_{10})^{2-}$, C the $(Bi_2O_2)^{2+}$ layers, and B the unit cells of the hypothetical perovskite structure $BiTiO_3$ [*Au3*].

single octahedral layers, and no sites are available for A cations. This particular phase has been prepared in a large number of oxides and oxyfluorides, where B = Ti, Nb, Ta and the O/F ratio depends upon the valencies of the A and B cations (see Tab. 4).

Many of these compounds are reported to exhibit ferroelectric distortions within the perovskite layers, and they will certainly be important for technical applications in the future.

3.2.3.2 Hexagonal $A_nB_{n-1}X_{3n}$ structures

As shown in Fig. 1(c), the cubic perovskite may be indexed on an hexagonal basis. It consists of cubic stacking of close-packed AX_3 layers with B cations in the all-anion octahedral interstices. Within a (110) plane, B-cation octahedra share common corners as shown schematically in Fig. 3(a). In the $Ba_5Ta_4O_{15}$ structure [*Ga5a*], the stacking sequence of the AX_3 layers is *a-b-c-b-c-a*, as shown in Fig. 24, and the B-cation vacancies are where the stacking is hexagonal. Thus the structure consists of perovskite blocks n AX_3 layers and $(n-1)$ B layers thick, separated by a stacking fault at a layer of B-cation vacancies. These hexagonal structures appear to be stabilized where the tolerance factor is $t > 1$.

3.2.3.3 $AX \cdot (ABX_3)_n$ structures

Materials having compositions intermediate between ABX_3 and A_2BX_4 may have similar diffraction patterns. However, this compositional region contains several phases having the structural formula $AX \cdot (ABX_3)_n$. Each phase contains perovskite sheets n units thick separated by AX (NaCl-type) sheets. The limiting composition A_2BX_4, corresponding to $n = 1$, is shown in Fig. 25. It is important for the theory of magnetism because, if A is nonmagnetic, then by symmetry there is no net molecular field within an antiferromagnetic layer from cations in adjacent antiferromagnetic layers. This permits the study of two-dimensional antiferromagnetism. The A_2BX_4 structure also permits the study of B^{2+} cations in oxides with a smaller B-X-B separation (hence stronger interaction) than is found in the BO compounds with rocksalt structure. The possible significance of this is illustrated by La_2NiO_4. The Ni^{2+} electrons of e_g symmetry appear to be collective in La_2NiO_4, localized in NiO.

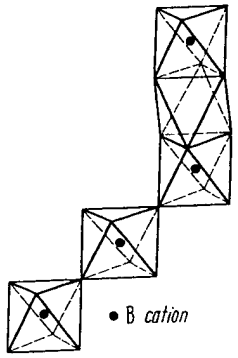

Fig. 24. Schematic (110) projection of the $Ba_5Ta_4O_{15}$ structure. Horizontal lines refer to BaO_3 close-packed layers with stacking *a*, *b*, or *c*.

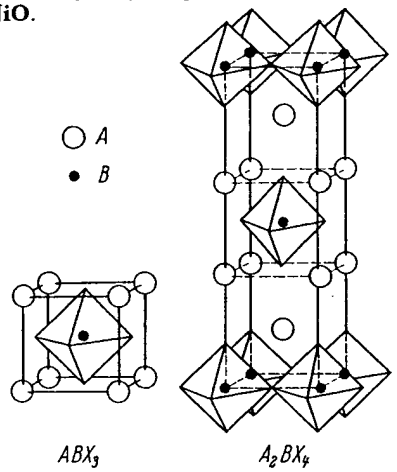

Fig. 25. Comparison of ABX_3 and A_2BX_4 structures [*Trf*].

3.2.4 Data: Crystallographic properties of non-ABX_3 compounds of composition A_xBX_3, $\square BX_3$, $(AX)_n(ABX)_m$ and $Bi_2O_2(A_{n-1}B_nO_{3n+1})$ with perovskite-related structure (Tab. 4)

Tab. 4.

See Fig. 20(a) for the tetragonal II bronze structure with $a \approx 12.5$ Å, $c \approx 4$ Å and Fig. 20(b) for the hexagonal bronze structure with $a \approx 7.4$ Å, $c \approx 7.5$ Å.

Within any section, the compounds are ordered by B-cation atomic number, and the order of the sections is as follows:

Tab. 4a — A_xBX_3
A_xBO_3; B = Nb, Mo, Ta, W, Re
A_xFeF_3
Tab. 4b — $\square$ BX_3
Tab. 4c — $\square$ $BB'X_6$
Tab. 4d — $(AX)_n(ABX_3)_m$
X = F^{-1}, Cl^{-1}; B^{2+} = Mg, Cr, Mn, Fe, Co, Ni, Cu, Zn, Cd
X = O^{-2}; B = Al, Ti, Cr, Mn, Fe, Co, Ni, Cu, Ga, Ge, Zr, Nb, Mo, Tc, Ru, Rh, Sn, Hf, Ir, Pb, U
Tab. 4e — $Bi_2O_2(A_{n-1}B_nO_{3n+1})$
$n = 1$; B = Mo, W $n = 2$; B = Nb, Ta $n = 3$; B = Nb, Ti $n = 4$, 5 and 8; B = Ti

For abbreviations, see p. 131.

Tab. 4a. A_xBX_3 compounds

Compound	Sym	a Å	b Å	c Å	angle	Ref.	Remarks	Magnetic Data
A_xNbO_3								in 3.3.4, Tab.
$Ba_{0.5}NbO_3$	O	12.17	20.5	7.87		*Fr1b*	Structure and review [*Ga15a*], S.S. with (Pb, Ca, Sr)$_{0.5}$NbO$_3$ [*Su4c*, *Fr1b*, *Is3a*], dielectric properties [*Gl0*]	
$Ba_{0.5}NbO_{2.5}$	T	12.60		3.95		*Ga14*		
$Sr_{0.95}NbO_3$	C	4.016				*Ri3*	Studied $x = 0.5 \cdots 1.0$	
$Sr_{0.7}NbO_3$	C	3.981				*Ri3*		
$Sr_{0.5}NbO_3$	O	11.021	7.33	5.604		*He12a*		
$Ca_{0.5}NbO_3$	O	5.764	15.09	5.232		*He12a*		
$Pb_{0.5}NbO_3$	O	17.51	17.81	7.72		*Fr2a*	Dielectric properties [*Go20*, *Su4b*], S.S. with (Ba, Sr)Nb_2O_6 [*Ba25c*, *Fr1b*, *Is2a*, *Kr7*, *Sm16a*, *Su4c*], P&S [*Ro16a*], S.S. with Ti, Zr, Sn [*Su1a*, *Su4b*, *Su4c*], S.S. with Li, Na, K, Rb, Cs, Y, La, Sm [*Su4b*, *Su4c*]	
	R	8.664			$\alpha = 88°\ 30'$	*Fr1a*	Prep. $T < 1250$ °C	
	T	12.46		3.907		*Fr2a*	$T = 570$ °C	
$La_{0.33}NbO_3$	O	3.911	3.917	7.908		*Iy1*	P&S [*Ke8*, *Ro13*, *Sa6a*]; dielectric properties, S.S. with $KSr_2Nb_5O_{15}$ [*Bu5*]	
$Ce_{0.33}NbO_3$	O	3.901	3.917	7.886		*Iy1*	P&S [*Ke8*, *Ro13*]	
$Ce_{0.25}NbO_3$	O	3.881	3.897	7.843		*Ko10*		
$Pr_{0.33}NbO_3$	O	3.891	3.915	7.862		*Iy1*	P&S [*Ke8*, *Ro13*]	
$Nd_{0.33}NbO_3$	O	3.878	3.907	7.840		*Iy1*	P&S [*Ke8*, *Ro13*]	
$Ln_{0.33}NbO_3$						*Ro13*	(Ln = Sm ··· Lu) not able to be prepared	
$Th_{0.25}NbO_3$	T	7.783		7.837		*Ke6*	P&S [*Ko10*], detailed structure [*Tr7*]	
$Pa_{0.25}NbO_3$	T	7.75		7.81		*Ke6*		
$U_{0.25}NbO_3$	T	7.727		7.792		*Ke6*	P&S [*Ko10*]	
$Np_{0.25}NbO_3$	T	7.69		7.76		*Ke6*		
$Pu_{0.25}NbO_3$	T	7.67		7.74		*Ke6*		
$Am_{0.33}NbO_3$	T	3.819		7.835		*Ke8*		
$Ba_2KNb_5O_{15}$	T	12.55		4.019		*Bu5a*	$T_{melt} = 1395$ °C	
$Ba_2NaNb_5O_{15}$	O	17.626	17.592	3.995		*Va13*	Dielectric and optical properties [*Va13*, *Ge14*, *Sm6a*, *Bu5a*, *Va11a*], Raman effect [*Bu4b*]; S.S. with K [*Bu5a*], Sr [*Va11a*]; elastic properties [*Sp0*], piezoelectric properties [*Wa15a*]	
$Sr_2KNb_5O_{15}$	T	13.47		3.942		*Gi1a*	Dielectric + optical properties [*Gi1a*, *Bu5*]	

Compound	Sym	a Å	b Å	c Å	angle	Ref.	Remarks	Magnetic Data
A_xNbO_3 (continued)								in 3.3.4, Tab.
$Sr_2NaNb_5O_{15}$	O	17.4	17.4	3.90		*Va13*	Dielectric + optical properties [*Va11a, Va13*]	
$Na_2LaNb_5O_{15}$	C	3.918				*Is5b*		
$Na_2BiNb_5O_{15}$	C	3.925				*Is5b*		
$K_3Li_2Nb_5O_{15}$	T	12.47		4.01		*Fu2a*	Tetr. W bronze type—dielectric + optical properties [*Va12, Va13, Va11a*]	
$K_2LaNb_5O_{15}$	T	12.580		3.930		*Sc27*	P & S [*Is5b*]	
$K_2CeNb_5O_{15}$	T	12.545		3.913		*Sc27*		
$K_2PrNb_5O_{15}$	T	12.530		3.918		*Sc27*		
$K_2NdNb_5O_{15}$	T	12.497		3.924		*Sc27*		
$K_2SmNb_5O_{15}$	T	12.474		3.917		*Sc27*		
$K_2EuNb_5O_{15}$	T	12.457		3.914		*Sc27*		
$K_2GdNb_5O_{15}$	T	12.450		3.912		*Sc27*		
$K_2TbNb_5O_{15}$	T	12.440		3.910		*Sc27*		
$K_2DyNb_5O_{15}$	T	12.431		3.903		*Sc27*		
$K_2HoNb_5O_{15}$	T	12.426		3.899		*Sc27*		
$K_2YNb_5O_{15}$	T	12.424		3.901		*Sc27*		
$K_2BiNb_5O_{15}$	O	17.75	17.90	7.84		*Is5b*	P & S [*Kr2, Kr8*]	
$Rb_2LaNb_5O_{15}$	T	12.633		3.945		*Sc27*		
$Ba_6(Ti_2Nb_8)O_{30}$	T	12.54		4.01		*St23*	Tetr. W bronze type, structure determined [*Ja9*]	
$Ba_6(Zr_2Nb_8)O_{30}$	T					*Fa1*	Tetr. W bronze	
$Ba_6(FeNb_9)O_{30}$	O	17.95	17.95	7.98		*Is5b*	Prop. [*Fa2, Fa1*] S.S. with Nd, Sm, Eu, Gd [*Fa1, Fa2*]	
$Sr_6(FeNb_9)O_{30}$	O	17.50	17.50	7.72		*Is5b*		
$A_6(B_xNb_{10-x})O_{30}$	T	≈ 12.5		≈ 3.9		*Kr2*	Tetr. W bronze type, A = Ba, Sr, Pb, Bi, La, Ce, Nd, Sm, Gd, K; B = Fe, Ni, Mg; dielectric properties [*Kr2*] gives review of the tetr. W bronze structure type	
$Ba_9MgNb_{14}O_{45}$	O	18.00	18.00	8.02		*Is5b*		
$Sr_9MgNb_{14}O_{45}$	O	17.55	17.55	7.82		*Is5b*		
$Ba_{0.27}Sr_{0.75}Nb_2O_{5.78}$	T	12.4032		3.9134		*Ja8a*	T = 25 °C, complete structure determination	
$K_{0.5}NbO_{2.5}F_{0.5}$	T	12.632		3.950		*Ma19a*	Tetragonal tungsten bronze	
A_xMoO_3								
$Rb_{0.27}MoO_3$	H	7.321		7.683		*Bi6*	High pressure preparation, metallic conductivity, P & S [*Ch1b*]	
$K_{0.93}MoO_3$	C	3.917				*Bi6*	High pressure preparation, metallic conductivity, P & S [*Ch1b*]	
$K_{0.89}MoO_3$	C	3.920				*Bi6*	High pressure preparation, metallic conductivity	
$K_{0.5}MoO_3$	T	12.32		3.859		*Bi6*	High pressure preparation, metallic conductivity, Θ_{cs} = 4.2 °K [*Sl7a*]	

Compound	Sym	a Å	b Å	c Å	angle	Ref.	Remarks	Magnetic Data
A_xMoO_3 (continued)								in 3.3.4, Tab.
$K_{0.28}MoO_3$	M	18.249	7.560	9.855	$\beta = 117° 32'$	*Gr2*	"Blue Mo bronze"; Prep. [*Wo10*], metallic conductivity [*Bo20*], structural discussion [*St22*], optical properties [*Di2a*]	
$K_{0.26}MoO_3$	M	14.278	7.723	6.387	$\beta = 92° 34'$	*St24*	"Red Mo bronze"; Prep. [*Wo10*]. Semiconducting [*Bo20*], structural discussion [*St22*]	
$Na_{0.97}MoO_3$	C	3.853				*Bi6*	High pressure preparation, $\Theta_{cs} < 1.3$ °K [*Sl7a*]	
$Na_{0.90}MoO_3$	C	3.847				*Bi6*	High pressure preparation	
$Na_{0.15}MoO_{2.83}$	M	9.57	5.50	12.95		*St25*	Complete structure, random vacancies [*St25*]; optical properties [*Di2a*]	
A_xTaO_3								
$Ba_{0.5}TaO_{3-x}$	T	12.60		3.95		*Ga14*	($x = 0 \cdots 0.5$), P&S [*Is2a*]	
$Ba_{0.5}TaO_3$	H	21.14		3.917		*La8*	Dielectric properties, P&S [*Is2a, Ga14*], review [*Ga15a*]	
$Sr_{0.5}TaO_{3-x}$	T	12.41		3.90		*Ga14*	($x = 0 \cdots 0.5$), review [*Ga15a*]	
$Ca_{0.5}TaO_3$	C	3.886				*Ja7*	Review [*Ga15a*]	
$Pb_{0.5}TaO_3$	O	17.635	17.695	7.757		*Is9*	Review of literature, P&S [*Is2a*]	
$Pb_{0.5}TaO_3$	T	17.71		7.788		*Is9*	$T = 300$ °C, tetr. $T > 270$ °C	
$Cu_{0.5}TaO_3$	C	7.522				*Ka16*	P&S [*Sh12*], optical properties [*Ka16*]	
$La_{0.33}TaO_3$	T	3.918		7.913		*Iy1*	P&S [*Ke8, Ro13, Tr8*], Prep. [*Sa6a*]	
$Ce_{0.33}TaO_3$	T	3.915		7.878		*Iy1*	P&S [*Ke8, Ro13*], Prep. [*Sa6a*]	
$Pr_{0.33}TaO_3$	O	3.895	3.910	7.836		*Iy1*	P&S [*Ke8, Ro13*], Prep. [*Sa6a*]	
$Nd_{0.33}TaO_3$	O	3.876	3.916	7.829		*Iy1*	P&S [*Ke8, Ro13*], Prep. [*Sa6a*]	
$Sm_{0.33}TaO_3$	O	3.882	3.896	7.785		*Iy1*	P&S [*Ke8, Ro13*]	
$Eu_{0.33}TaO_3$	O	3.871	3.885	7.792		*Ke8*		
$Gd_{0.33}TaO_3$	T	3.874		7.795		*Iy1*	P&S [*Ke8, Ro13*]	
$Tb_{0.33}TaO_3$	T	3.851		7.780		*Ke8*		
$Dy_{0.33}TaO_3$	T	3.847		7.769		*Iy1*	P&S [*Ke8, Ro13*]	
$Ho_{0.33}TaO_3$	T	3.841		7.756		*Iy1*	P&S [*Ke8*]	
$Er_{0.33}TaO_3$	T	3.825		7.754		*Iy1*	P&S [*Ke8*]	
$Yb_{0.33}TaO_3$	M	3.828	7.749	3.839	$\beta = 90° 54'$	*Ro13*		
$Y_{0.33}TaO_3$	T	3.824		7.758		*Iy1*	P&S [*Ke8, Tr8, Ro13, Ly1*]	
$Th_{0.25}TaO_3$	C	7.810				*Ke6*	P&S [*Ko10*]	
$Pa_{0.25}TaO_3$	T	7.77		7.78		*Ke6*		
$U_{0.25}TaO_3$	T	7.739		7.773		*Ke6*	P&S [*Ko10*]	
$Np_{0.25}TaO_3$	T	7.70		7.75		*Ke6*		
$Pu_{0.25}TaO_3$	T	7.654		7.731		*Ke6*		
$Am_{0.33}TaO_3$	T	3.889		7.820		*Ke8*		
$K_{0.5}TaO_{2.5}F_{0.5}$	T	12.569		3.961		*Ma19a*	Tetragonal tungsten bronze	

Compound	Sym	a Å	b Å	c Å	angle	Ref.	Remarks	Magnetic Data
A_xWO_3								in 3.3.4, Tab.
$Cs_{0.32}WO_3$	H	7.42		7.63		*Ma17*	Superconducting, $\Theta_{cs} = 1.12$ °K [*Sw3*]	
$Cs_{0.30}WO_3$	H	7.38		7.59		*Ma17*	Thermal expansion to 720 °C [*We15*]	
$Rb_{0.32}WO_3$	H	7.386		7.54		*Si7*	P&S [*Ma17*], metallic conduction and magnetic susceptibility [*Si7, Si9*], optical properties [*Do6*]	
$Rb_{0.27}WO_3$	H	7.394		7.516		*We15*	Superconductivity, $\Theta_{cs} = 1.98$ °K [*Sw3*], thermal expansion to 970 °C [*We15*]	
$(NH_4)_{0.33}WO_3$	H	7.395		7.525		*Gi1*	Superconductivity 2.2 °K $\geq \Theta_{cs}$ [*Gi1*]	
$(NH_4)_{0.06}WO_3$	T	7.60		6.36		*Ne8a*		
$K_{0.9}WO_3$	C	3.926				*Bi6*	High pressure preparation (metallic conductivity), P&S [*Ch1b*]	
$K_{0.55}WO_3$	T	12.326		3.845		*We15*	Magnetic susceptibility ($x = 0.53$) [*Ku5*], electric properties ($x = 0.57$ and 0.63) [*St43*], thermal expansion to 750 °C ($x = 0.3 \cdots 0.55$) [*We15*]	
$K_{0.3}WO_3$	H	7.385		7.513		*We15*	Electric + magnetic properties [*Sh8, Si9, Si7*], S.S. with Li [*Ba11*], S.S. with Na [*Br8*], P&S [*Ma12, Ma17, De19*], review [*Di3, Ma15, Ma18, Si9*]	
$K_{0.13}WO_3$	H	7.370		7.515		*Ba11*	Superconductivity, Θ_{cs} (Hex) = 0.5 °K, Θ_{cs} (Tetr.) = 1.5 °K [*Sw3*], magnetic properties [*Ku5, Fu1, Gr8, St43*]	
Na_xWO_3	C	3.8				*Br22*	$a = (0.0819\ x + 3.7846)$ Å [*Br22, We2*]; cubic, $0.26 < x < 1.0$; early preparation [*Bo17, Wr1, Ph1, Wo1, Sp1, Sp2, Ka5*], P&S [*St37, St38, St39, Va5, De6, Ha5, Br8, Ha4, Bi6, Ch1b*]; neutron diffraction ($0.56 < x < 0.86$) [*At1*]; electrical properties [*Hu8, Hu9, Hu10, Mu3, Mu4, Br21, Fu1, Ga21*], reviews [*Di3, Ma15, Ma18, Ri1, Si7*], optical properties [*Di3a*]	
	T	12.094		3.748		*Ma13*	$x = 0.28$, tetragonal II [*Ri1*]. Superconductivity, $\Theta_{cs} < 1$ °K [*Sw3, Ra12*], optical properties [*Br22, Da3*], NMR [*Fr18, Fr19, Na12*]	
	T	5.248		3.895		*Ma16*	$x = 0.10$, tetragonal I [*Ri1*]; thermal properties [*Sh7, Fu1, Ge11, Ta2, Ve11*], Na diffusion [*Sm6*], electrostatic energy calculated [*Sm5*]	
$Li_{0.30}WO_3$	H	7.405		7.554		*Gi1*	Metallic conductivity, superconducting $\Theta_{cs} < 1.3$ °K [*Gi1*]	
$Li_{0.394}WO_3$	C	3.715				*Si10*	Magnetic properties, Pauli paramagnetic or diamagnetic [*Si10, Co17*], metallic conductivity [*Co17, Si10, Si7, Sh8*], P&S [*Ma19, Ma16, St40*]	
$Li_{0.36}WO_3$	C	3.718				*Co17*	Review [*Di3*]	

Compound	Sym	a Å	b Å	c Å	angle	Ref.	Remarks	Magnetic Data
A_xWO_3 (continued)								in 3.3.4, Tab.
$Li_{0.05}WO_3$	C	3.723				*Co17*		
$H_{0.5}WO_3$	C	3.755				*Gl1*	I. R. spectra [*Si7a*]	
$H_{0.23}WO_3$	T	5.22		3.88		*Di2*	Structure determination by x-ray and neutron diffraction, I. R. spectra [*Si7a*]	
$H_{0.1}WO_3$	O	7.247	7.502	3.84		*Gl1*	I. R. spectra [*Si7a*]	
$Ba_{0.12}WO_3$	T	12.16		3.843		*Co19*	$x = 0 \cdots 0.13$; $\chi_m = 20 \cdot 10^{-6}$ emu/mole, Novel preparation [*Co16*]; superconductivity, $x = 0.13$, $\Theta_{cs} = 1.9$ °K [*Sw4*]	
$Ba_{0.10}Na_{0.33}WO_3$	T	12.12		3.834		*Co19*	Metallic conductivity	
Ca_xWO_3	O	7.340	7.420	3.840		*Va2*	$x = 0.02$, $0 < x < 0.01$ (monoclinic); $0.01 < x < 0.03$ (orthorhombic), studied as function of T [*Va2, Va4*]	
	T	5.240		3.854		*Va2*	$x = 0.035$, $0.03 \leq x < 0.40$ (tetragonal); $0.04 < x < 0.095$ (two phase)	
	T	5.292		3.832		*Va2*	$x = 0.10$, $0.095 \leq x < 0.105$ (tetragonal); $0.105 \leq x < 0.125$ (cubic $a = 3.790$ Å); $x > 0.125$ (two phase)	
$Sn_{0.24}WO_3$	H	7.430		7.581		*Gi1*	Metallic conductivity, superconducting $\Theta_{cs} < 1.3$ °K [*Gi1*]	
$Sn_{0.19}WO_3$	T	12.241		3.774		*Gi1*	Superconducting $\Theta_{cs} < 1.3$ °K [*Gi1*]	
$Pb_{0.17}WO_3$	T	12.163		3.767		*Be30*	$x = 0.057 \cdots 0.16$ monoclinic, $x = 0.16 \cdots 0.35$ tetr.	
$Pb_{0.35}WO_3$	T	12.207		3.782		*Be30*	Novel preparation [*Co16*]	
$La_{0.08}WO_3$	C	3.829				*Br23*	Cubic, ($x = 0.08 \cdots 0.19$), metallic conductivity [*Sh6*]	
$La_{0.02}WO_3$	T	7.52		3.89		*Br23*		
$Ce_{0.1}WO_3$	C	3.828				*Os2*	$n_{eff} = 2.5$, all rare-earth bronzes blue-violet	
$Pr_{0.1}WO_3$	C	3.827				*Os2*	$n_{eff} = 3.6$	
$Nd_{0.1}WO_3$	C	3.822				*Os2*	$n_{eff} = 3.8$	
$Sm_{0.1}WO_3$	C	3.817				*Os2*	$n_{eff} = 1.6$ (temperature dependent), crystal growth [*Co14*]	
$Eu_{0.15}WO_3$	C	3.828				*Os2*		
$Eu_{0.10}WO_3$	C	3.815				*Os2*	$n_{eff} = 3.4$ (temperature dependent), P&S [*Sh6*]	
$Eu_{0.085}WO_3$	C	3.808				*Os2*		
$Gd_{0.1}WO_3$	C	3.810				*Os2*	$n_{eff} = 7.9$, crystal growth [*Co14*], P&S [*Sh6*], relation of a vs. x [*We2*]	
$Tb_{0.1}WO_3$	C	3.808				*Os2*	$n_{eff} = 9.6$	
$Dy_{0.1}WO_3$	C	3.805				*Os2*	$n_{eff} = 10.6$	
$Ho_{0.1}WO_3$	C	3.801				*Os2*	$n_{eff} = 10.6$, P&S [*Sh6*]	
$Er_{0.1}WO_3$	C	3.797				*Os2*	$n_{eff} = 9.5$	
$Tm_{0.1}WO_3$	C	3.794				*Os2*	$n_{eff} = 7.5$, crystal growth [*Co14*]	

[illegible]	[illegible]	[illegible]				Os2	n_{eff} = 7.5, crystal growth [Co14]	

Compound	Sym	a Å	b Å	c Å	angle	Ref.	Remarks	Magnetic Data
A_xWO_3 (continued)								in 3.3.4, Tab.
$Yb_{0.1}WO_3$	C	3.791				Os2	n_{eff} = 4.5	
$Lu_{0.1}WO_3$	C	3.788				Os2	n_{eff} = 0	
$Y_{0.09}WO_3$	C	3.800				Br23	Tetr. $x < 0.09$, metallic conductivity [Sh6]	
Al_xWO_3	O	7.368	7.476	3.850		Po10	$x = 0.015$, $0.010 < x < 0.030$ orthorhombic; $0.030 < x < 0.105$, two phase; studied as function of T [Va4]	
	O	5.387	5.440	3.784		Po10	$0.105 < x \leq 0.135$; $x > 0.135$, two phase	
$Cu_{0.77}WO_3$	O	3.73	3.88	7.74		Co18	Semiconducting ≈ 0.15 eV	
$Cu_{0.26}WO_3$	Tr	5.85	6.65	4.88	$\alpha = 134° 45'$ $\beta = 91° 40'$ $\gamma = 93° 37'$	Co18	Magnetic susceptibility $\chi_m = 34 \cdot 10^{-6}$ emu/mole	
$Ag_{0.01}WO_3$	O	3.73	3.85	7.35		Si8	Metallic conductivity, P&S [Po2]	
Cd_xWO_3	O	7.316	7.532	3.848		Va3	$x = 0.005$, $0.005 \leq x < 0.02$ orthorhombic	
	T	5.244		3.867		Va3	$x = 0.020$, $0.02 \leq x < 0.04$ tetragonal	
$In_{0.05}WO_3$	T	5.233		3.863		Bo21	$x = 0.01 \cdots 0.05$, P&S ($x = 0.11$) [Bi3]	
$In_{0.30}WO_3$	H	7.384		7.508		Bo21	$x = 0.2 \cdots 0.3$, metallic conductivity, weak diamagnetism	
$In_{0.33}WO_3$	H	7.50		7.56		Sw1	$x = 0.26 \cdots 0.33$; metallic conductivity	
$Tl_{0.36}WO_3$	T	7.31		12.80		Si6	Metallic conductivity, $x = 0.19 \cdots 0.36$; novel preparation [Co16]	
$U_{0.083}WO_3$	C	3.812				Ko10	relationship of a vs. x [We2]	
$U_{0.125}WO_3$	C	3.821				Ko10	P&S [Sh9]	
$Cs_{0.3}(Ta_{0.3}W_{0.7})O_3$	H	7.450		7.821		Ga4	Thermal expansion and resistivity (10^8 Ωcm)	
$Rb_{0.3}(Ta_{0.3}W_{0.7})O_3$	H	7.342		7.715		Ga4	Thermal expansion and resistivity (10^9 Ωcm)	
$K_{0.3}(Ta_{0.3}W_{0.7})O_3$	H	7.333		7.685		Ga4	Thermal expansion and resistivity (10^7 Ωcm)	
$K_{0.5}(Ta_{0.5}W_{0.5})O_3$	T	12.36		3.90		Ga14	Entire range of S.S. with Ta and Nb [De19a]	
A_xReO_3								
$K_{\approx 0.6}ReO_3$	C	3.895				Sl2	Metallic conductivity	
$K_{\approx 0.3}ReO_3$	H	7.318		7.485		Ch1b	High pressure preparation, $\Theta_{cs} = 3.6$ °K [Sl7a]	
$Na_{\approx 0.6}ReO_3$	T	3.825		3.841		Sl7a	Metallic, $\Theta_{cs} < 1.3$ °K, P&S [Sl2]	
A_xFeF_3								
$Rb_{0.29}FeF_3$	H	7.36		7.53		Tr1	Hex ($x = 0.18 \cdots 0.30$); P&S [De13a]	
$K_{0.95}FeF_3$	C	4.113				De11	($x = 0.95 \cdots 1.0$) cubic	
$K_{0.50}FeF_3$	T	12.60		3.936		De11	($x = 0.40 \cdots 0.60$) tetr	
$K_{0.25}FeF_3$	H	7.385		7.510		De11	($x = 0.18 \cdots 0.25$) hex	
$Na_{0.11}FeF_3$	R	5.37			$\alpha = 59°$	Tr1	$x = 0.0 \cdots 0.16$; P&S [De13a]	
$Tl_{0.30}FeF_3$	H	7.35		7.52		Tr1	Hex ($x = 0.20 \cdots 0.31$); P&S [De13a]	

Tab. 4b. □ BX_3 compounds

Compound	Sym	*a* Å	*b* Å	*c* Å	angle	Ref.	Remarks	Magnetic Data
								in 3.3.4, Tab.
AlF_3	R	5.029			$\alpha = 58° 31'$	*Ke20*		
ScF_3	R	5.708			$\alpha = 59° 32'$	*No10*		
TiF_3	R	5.519			$\alpha = 58° 53'$	*Si2*	P&S [*Eh2*]	6
$TiOF_2$	C	3.798				*Vo3*		
VF_3	R	5.373			$\alpha = 57° 31'$	*Ja2a*	Neutron diffraction [*Wo13*]	6
CrF_3	R	5.2643			$\alpha = 56° 37'$	*Kn2*	Prop. [*Bi7, Ha11, Ha12, Bo33, Ra9*], structure [*Ja3*], neutron diffraction [*Wo13*]	6
	R	5.332			$\alpha = 56° 37'$	*Kn2*	300 °C	
MnF_3	M	8.904	5.037	13.448	$\beta = 92° 44'$	*He9*	Neutron diffraction [*Wo13*], Prop. [*Bo33, Bo34, Ny1, Kl5, He10, Sm1*]	6
FeF_3	R	5.362			$\alpha = 58° 0'$	*He11*	Neutron diffraction [*Wo13*], Prop. [*Bi7, Sh5, We17, Bu1*], crystal transformation [*Cr5*]	6
CoF_3	R	5.279			$\alpha = 57° 0'$	*He11*	Neutron diffraction [*Wo13*], Prop. [*He8, Ny1*]	6
GaF_3	R	5.20			$\alpha = 57° 30'$	*Br6*	P&S [*Mu1*]	
ZrF_3	C	3.96				*Eh3*		
NbF_3	C	3.903				*Eh4*	P&S [*Sc2*], "doubtful"	6
NbO_2F	C	3.902				*Fr15*		
MoF_3	C	3.8985				*Gu8*	Neutron diffraction [*Wi6*], P&S [*La7*]	6
RuF_3	R	5.408			$\alpha = 54° 90'$	*He11*	Neutron diffraction [*Wi6*]	6
RhF_3	R	5.330			$\alpha = 54° 25'$	*He11*		
PdF_3	R	5.5234			$\alpha = 53° 55'$	*He11*	Neutron diffraction [*Wi6*], Prop. [*Ba19, Ba20, Ny1, Fi3*]	6
InF_3	R	5.722			$\alpha = 56° 15'$	*Mu1*		
TeO_3	R	5.180			$\alpha = 56° 25'$	*Du2*	Prep. [*Lo8*]	
TaF_3	C	3.9012				*Gu8*	Prop. [*Ny1*], "doubtful"	6
TaO_2F	C	3.896				*Fr15*		
WO_3	M	7.297	7.539	7.688	$\beta = 90° 55'$	*Lo6*	Structure [*Br1, Ta15*], neutron diffraction [*Lo6*], Prop. [*Cr7, Cr8, Ta15, Co16, Be22, Iw2, De16, Ke10*], optical properties [*Di3a*], phase transformations [*Pe3a*]	
$Re_{0.33}W_{0.67}O_3$	C	3.7574				*Sl2*		
ReO_3	C	3.7477				*Sl2*	P&S, [*Me11, Bi4, Bi5*], crystal growth [*Fe21*], Prop. [*Sl2, Fe21, Fe10, Gu6a*], structure vs. oxygen content [*Sl2*], DeHaas-Van Alphen effect [*Ma27a*], NMR [*Na11a*]	
IrF_3	R	5.418			$\alpha = 54° 8'$	*He11*	P&S [*Ro2*]	
UO_3	C	4.156				*Wa6*	P&S [*En2*]	

IrF_3	R	5.418			$\alpha = 54° 8'$	*He11*	P&S [*Ro2*]	
UO_3	C	4.156				*Wa6*	P&S [*En2*]	

Tab. 4c. □ $BB'X_6$ compounds

Compound	Sym	*a* Å	*b* Å	*c* Å	angle	Ref.	Remarks	Magnetic Data
								in 3.3.4, Tab.
$BB'X_6$							Structural review [*Gi2, Ke11, Co29*]	
$NaVF_6$	R	5.63			$\alpha = 56° 30'$	*Ke11*		
$LiVF_6$	R	5.30			$\alpha = 56° 18'$	*Ke11*		
$CaMnF_6$	R	5.59			$\alpha = 55° 36'$	*Ho14*		
$MgMnF_6$	R	5.26			$\alpha = 56° 54'$	*Ho14*		
$NaNbF_6$	C	8.26				*Ke11*	P&S [*Co29*]	
$LiNbF_6$	R	5.47			$\alpha = 58° 6'$	*Ke11*		
$NaMoF_6$	C	8.194				*Ed3*	Magnetic properties $80 < T < 300$ °K, $n_{eff} = 1.66$, $\Theta_p = -218$ °K [*Ha18*]	
$LiMoF_6$	R	5.43			$\alpha = 57° 6'$	*Bo18*		
$NaTcF_6$	R	5.77			$\alpha = 55° 48'$	*Ed4*	P&S [*Hu7*]	
$NaRuF_6$	R	5.80			$\alpha = 54° 30'$	*Bo18*		
$LiRuF_6$	R	5.39			$\alpha = 56° 0'$	*Bo18*		
$GePdF_6$	R	5.53			$\alpha = 54° 0'$	*Ba21*	Magnetic properties, $n_{eff} = 2.82$, $\Theta_p = 31$ °K [*Ba21*]	
$PdPdF_6$	R	5.52			$\alpha = 53° 54'$	*Ba21*	P&S [*He11*], see PdF_3	
$SnPdF_6$	R	5.70			$\alpha = 53° 6'$	*Ba21*	Magnetic properties, $n_{eff} = 2.98$, $\Theta_p = 28$ °K [*Ba21*]	
$PtPdF_6$	R	5.55			$\alpha = 54° 0'$	*Ba21*	Magnetic properties, $n_{eff} = 2.72$, $\Theta_p = 1.2$ °K [*Ba21*]	
$NaSbF_6$	C	8.184				*Te12*	P&S [*Sc22*]	
$LiSbF_6$	R	5.44			$\alpha = 57° 0'$	*Bu6*	Complete structure; P&S [*Ke11*]	
$CaHfF_6$	C	8.462				*Ke7*		
$NaTaF_6$	C	8.28				*Ke11*	P&S [*Co29*]	
$LiTaF_6$	R	5.48			$\alpha = 58° 0'$	*Ke11*		
$NaWF_6$	C	8.18				*Ke11*	Magnetic properties $80 < T < 300$ °K, $n_{eff} = 0.5$, $\Theta_p = -125$ [*Ha18*]	
$LiWF_6$	R	5.45			$\alpha = 57° 24'$	*Ke11*		
$NaReF_6$	C	8.18				*Ke11*	P&S [*Pe1*]; magnetic properties $80 < T < 300$ °K, $n_{eff} = 1.57$, $\Theta_p = -100$ °K [*Ha19*]	
$NaOsF_6$	R	5.80			$\alpha = 55° 12'$	*Bo18*		
$LiOsF_6$	R	5.43			$\alpha = 55° 30'$	*Bo18*		
$NaIrF_6$	R	5.80			$\alpha = 55° 12'$	*Bo18*		
$LiIrF_6$	R	5.41			$\alpha = 56° 0'$	*Bo18*		
$PdPtF_6$	R	5.55			$\alpha = 54° 0'$	*Ba21*		
$CaPbF_6$	C	8.476				*Ho15*		

Tab. 4d. $(AX)_n(ABX_3)_m$ compounds

Compound	Sym	*a* Å	*b* Å	*c* Å	angle	Ref.	Remarks	Magnetic Data
Halides								in 3.3.4, Tab.
Cs_2MgF_4							No cell dimensions [*Be22a*]	
Rb_2MgF_4	T	4.055		13.79		*Ba1*		
K_2MgF_4	T	3.955		13.706		*Re6*	P&S [*Wi12*], S.S. with K_2NiF_4 [*We20*]	
$(NH_4)_2MgF_4$	T	4.07		13.88		*Ch8a*		
Tl_2MgF_4	T	4.007		14.43		*Vo1*		
Na_2CrF_4	M	3.344	9.533	5.657	$\beta = 87^\circ 12'$	*Vo1*	Not K_2NiF_4 type	
Cs_2CrCl_4	T	5.215		16.46		*Se2*		
Rb_2CrCl_4	T	5.143		15.73		*Se2*		
K_2CrCl_4							Possibly distored K_2NiF_4 [*Se2*]	
Cs_2MnF_4	T	4.31		14.63		*Co25*		
Cs_2MnCl_4	T					*Le7*	K_2NiF_4 type	6
Rb_2MnF_4	T	4.228		13.89		*Co25*	P&S [*Vo1*], Prop. [*De20, Br5*]	6
K_2MnF_4	T	4.20		13.14		*Br5*	P&S [*Vo1, Co25*], Prop. [*De20, Co15*]	6
Rb_2FeF_4	T	4.20		13.38		*Tr1*		6
K_2FeF_4	T	4.140		12.98		*De12*		
$K_3Fe_2F_7$	T	4.130		21.15		*De12*		
Tl_2FeF_4	T	4.194		13.91		*Vo1*		
Rb_2CoF_4	T	4.135		13.67		*Ru6*	P&S [*Ru3, Ru8*]	6
K_2CoF_4	T	4.07		13.08		*Ru6*	Prop. [*Ru8, Sr3, Sr2, Va1, Le8*], dielectric properties [*La1a*]	6
Tl_2CoF_4	T	4.11		14.05		*Ru6*	P&S [*Ru3, Ru8*]	6
Rb_2NiF_4	T	4.087		13.71		*Ru8*	Prop. [*Ru5*]	6
K_2NiF_4	T	4.006		13.076		*Ba10*	Prop. [*Sr2, Go26, De20, Ru5, Ti5, We20*], dielectric properties [*La1b*], neutron diffraction [*Pl4, Pl5, Pl6, Pl7, Le6, Le7*]	6
$(NH_4)_2NiF_4$	T	4.08		13.78		*Ru8*		6
Tl_2NiF_4	T	4.051		14.22		*Ru8*		6
Rb_2CuF_4	T	4.238		13.28		*Ru6*	P&S [*Ru3*], optical properties [*Sc10a*]	6
K_2CuF_4	T	4.145		12.72		*Ru6*	Prop. [*Ru6, Va1*], P&S [*Kn1, Gu1a*]	6
Na_2CuF_4	M	3.261	9.354	5.601	$\beta = 87^\circ 30'$	*Ba3*	P&S [*Ru3*]—not K_2NiF_4 type	
Tl_2CuF_4	T	4.199		13.66		*Ru6*	P&S [*Ru3*]	6
$(NH_4)_2CuCl_4$	O	7.20	7.20	15.46		*Wi9*		
$(CH_3NH_3)_2CuCl_4$	O	7.30	7.54	18.55		*Gr7*	Prop. [*De20, Bo15, Ko8*], Prep. [*Re7*]	6
$(C_2H_5NH_3)_2CuCl_4$	O	7.35	7.47	21.18		*Wi9*	Prop. [*De20, Bo15, Ko8*], Prep. [*Re7*]	6
Rb_2ZnF_4	T	4.125		13.67		*Ba1*	P&S [*Sc10*]	
K_2ZnF_4	T	4.02		13.05		*Sc10*		
$K_3Zn_2F_7$	T	4.063		21.22		*Br12*		

$K_3Zn_2F_7$	T	4.063		21.22		*Br12*		

Compound	Sym	*a* Å	*b* Å	*c* Å	angle	Ref	Remarks	Magnetic Data
Halides (continued)								in 3.3.4, Tab.
$(NH_4)_2ZnF_4$	T	4.14		13.97		*Cr3*		
Tl_2ZnF_4	T	4.105		14.10		*Vo1*		
Rb_2CdF_4	T	4.414		13.98		*Co27a*		
$Rb_3Cd_2F_7$	T	4.403		22.71		*Co27a*		
K_2CdF_4							Prep. [*Co26, Co27a*]	
$K_3Cd_2F_7$							Prep. [*Co26, Co27a*]	
Cs_2CdCl_4	T	5.26		16.88		*Si3*		
Oxides								
$SrLaAlO_4$	T	3.75		12.5		*Ru1*	Eu^{3+} fluorescence [*Ni1*]	
Sr_2TiO_4	T	3.88		12.58		*Ba10*	P&S [*Ru1, Br11, Lu2, Po9, Ha19a*], Eu^{3+} fluorescence [*Ni1*]	
$Sr_3Ti_2O_7$	T	3.90		20.38		*Ru2*	P&S [*Lu2*]	
$Sr_4Ti_3O_{10}$	T	3.90		28.1		*Ru2*		
$Ca_3Ti_2O_7$	O	5.412	5.426	19.50		*Pe3*	P&S [*Ro17*]	
$Ca_4Ti_3O_{10}$	O	5.404	5.435	27.14		*Pe3*	P&S [*Ro17*]	
$NaLaTiO_4$	T	3.76		12.95		*Bl12*	(Na and Ln ordered). Fluorescence: Eu [*Bl12a*]	
$NaNdTiO_4$	T	3.76		12.79		*Bl12*		
$NaSmTiO_4$	T	3.77		12.59		*Bl12*		
$NaGdTiO_4$	T	3.77		12.46		*Bl12*	Fluorescence: Eu [*Bl12a*]	
$NaDyTiO_4$	T	3.77		12.22		*Bl12*		
$NaTmTiO_4$	T	3.78		12.05		*Bl12*		
$NaLuTiO_4$	T	3.78		11.92		*Bl12*	Fluorescence: Eu [*Bl12a*]	
$NaYTiO_4$	T	3.786		12.209		*Re2*	P&S [*Bl12*], fluorescence: Eu [*Bl12a*]	
$Na_3Y_3Ti_4O_{14}$	T	3.79		20.2		*Re2*		
$Na_2Y_2Ti_3O_{10}$	T	3.79		28.2		*Re2*		
Eu_2TiO_4	T	3.89		12.53		*Ro21*	P&S [*Mc1b*]	
$Eu_3Ti_2O_7$	T	3.899		20.295		*Ro21*	P&S [*Mc1b*]	
Sr_2CrO_4	T	3.82		12.4		*Lo1a*	Cr^{4+}, high pressure preparation	
$Sr_3Cr_2O_7$	T	3.82		20.1		*Lo1a*	Cr^{4+}, high pressure preparation	
$SrLaCrO_4$	T	3.84		12.52		*Bl9*		
Sr_2MnO_4	T	3.79		12.43		*Ba10*	Substitution of La [*Sr2*]	
Ca_2MnO_4	T	3.667		12.063		*Ma6*	P&S [*Ru1, Br11*]	6
$Ca_3Mn_2O_7$	T	3.709		19.44		*Ma6*	97% Mn^{4+}; P&S [*Ru1, Br11*]	6
$Ca_4Mn_3O_{10}$	T	3.724		26.90		*Ma6*	97% Mn^{4+}; P&S [*Ru1, Br11*]	6
$Sr_{1.5}La_{0.5}MnO_4$	T					*Le7*		6
$SrLaMnO_4$	T	3.88		12.5		*Bl9*		
Sr_2FeO_{4-x}	T	3.864		12.390		*Ga19*	$x = 0.3$	6
$Sr_3Fe_2O_{7-x}$	T	3.853		20.149		*Ga19*	$x = 0.1$, P&S [*Br10*], Prop. [*Ma7*]	6

Compound	Sym	*a* Å	*b* Å	*c* Å	angle	Ref.	Remarks	Magnetic Data
Oxides (continued)								in 3.3.4, Tab.
$Sr_3Fe_2O_{7-x}$ cont.	T	3.892		20.054		*Ga19*	$x = 1$, Prop. [*Ma7*]	
Sr_2FeO_3F	T	3.84		12.98		*Ga3*		
$SrLaFeO_4$	T	3.86		12.69		*Bl9*	Prop. [*As6*]	6
$SrLaCoO_4$	T	3.80		12.50		*Bl9*		
La_2CoO_4	O	5.482	5.539	12.66		*Ra2*	Prep. [*Fo1, Fo3*] substitution of Sr [*Sr2, Go6*]	
$La_2Co_{0.5}Li_{0.5}O_4$	T	3.77		12.58		*Bl9*		6
$La_{1.5}Sr_{0.5}CoO_4$	T						Prop. [*Sr2, Go26*]	6
$La_{1.5}Sr_{0.5}Co_{0.5}Mg_{0.5}O_4$	T	3.82		12.58		*Bl9*		6
$Sr_{1.5}La_{0.5}Co_{0.5}Ti_{0.5}O_4$	T	3.85		12.62		*Bl9*		6
La_2NiO_4	T	3.855		12.652		*Ra2*	P&S [*Fo1, Fo3*], Prop. [*Sm34, Sm24*]	6
Pr_2NiO_4							Prop. [*Sm34*]	6
Nd_2NiO_4	T	3.81		12.31		*Fo1*	Prop. [*Sm34, Sm24*]	6
$SrLaNiO_4$	T	3.80		12.51		*Bl9*		
$La_2Ni_{0.5}Li_{0.5}O_4$	T	3.75		12.89		*Bl9*		6
La_2CuO_4	O	5.36	5.41	13.17		*Lo1c*	Prep. [*Fr25, Fo1, Fo3*]	
	T	3.81		13.24		*Lo1c*	at 420 °C, tetr. $T > 250$ °C	
Pr_2CuO_4	T	3.96		12.23		*Fr25*		
Nd_2CuO_4	T	3.94		12.15		*Fo1*	P&S [*Fr25*]	
Sm_2CuO_4	T	3.91		11.93		*Fo1*	P&S [*Fr25*]	
Eu_2CuO_4	T	3.91		11.92		*Fr25*		
Gd_2CuO_4	T	3.89		11.85		*Fo1*	P&S [*Fr25*]	
$SrLaGaO_4$	T	3.84		12.71		*Bl9*		
Ca_2GeO_4	T	3.70		11.88		*Re2*	100 kbars, 900 °C required, P&S [*Ri8b*]	
Ba_2ZrO_4	T	4.187		13.48		*Sc18a*		
Sr_2ZrO_4	T	5.801		12.445		*Pe3*	P&S [*Sc18a*]	
$Sr_3Zr_2O_7$	O	5.798	5.808	20.94		*Pe3*		
$Sr_4Zr_3O_{10}$	O	5.795	5.814	29.34		*Pe3*		
K_2NbO_3F	T	3.96		12.67		*Ga2*		
Sr_2MoO_4	T	3.92		12.84		*Ba10*	P&S [*Sc16*], Prop. [*Ro2a*]	6
Ba_2TcO_4	T	4.011		13.40		*Ke9*		
Sr_2TcO_4	T	3.902		12.72		*Ke9*		
Sr_2RuO_4	T	3.870		12.74		*Ra6*	Prop. [*Ca2*]	6
Sr_2RhO_4	T	3.85		12.90		*Ra6*		
$SrLaRhO_4$	T	3.92		12.78		*Bl9*		
Ba_2SnO_4	T	4.130		13.27		*We8*	P&S [*Wa2*]	
Sr_2SnO_4	T	4.037		12.53		*We8*	P&S [*Wa2*]	
Ca_2SnO_4							Not K_2NiF_4 type, [*We8*]	
Ba_2HfO_4	T	4.161		13.45		*Sc18a*		
Sr_2HfO_4	T	4.089		12.52		*Sc18a*		

Compound	Sym	a Å	b Å	c Å	angle	Ref.	Remarks	Magnetic Data
Oxides (continued)								in 3.3.4, Tab. 6
Sr_2IrO_4	T	3.89		12.92		*Ra7*	Prop. [*Ro2a*]	
Ca_2IrO_4	H	9.423		3.195		*Ba5a*	Not K_2NiF_4 type	
Ba_2PbO_4	T	4.296		13.30		*We8*	P&S [*Wa2*]	
A_2PbO_4						*We8*	A = Sr + Ca, not K_2NiF_4 type	
Cs_2UO_4	T	4.38		14.79		*Ko11*		
Rb_2UO_4	T	4.345		13.83		*Ko11*		
K_2UO_4	T	4.335		13.10		*Ko11*		
β-Na_2UO_4	O	5.795	5.97	11.68		*Ko11*		

Tab. 4e: see next page

Tab. 4e. $Bi_2O_2(A_{n-1}B_nO_{3n+1})$ compounds

Compound	Sym	*a* Å	*b* Å	*c* Å	angle	Ref.	Remarks	Magnetic Data
								in 3.3.4, Tab.
Bi_2MoO_6	O	5.49	5.50	16.24		*Bl10*	P&S [*Ze3*]	
Bi_2WO_6	O	5.49	5.50	16.24		*Bl10*		
$BaBi_2Nb_2O_9$	O	5.533	5.533	25.55		*Au2*	P&S [*Su3*], S.S. with Sr and Ca [*Sm19*]	
$SrBi_2Nb_2O_9$	O	5.504	5.504	25.05		*Au2*	P&S [*Sm19*; *Su3*]	
$CaBi_2Nb_2O_9$	O	5.435	5.485	24.87		*Au2*	P&S [*Sm19*; *Su3*], dielectric properties [*Is3*]	
$PbBi_2Nb_2O_9$	O	5.492	5.503	25.53		*Au2*	P&S [*Su2*; *Su3*], S.S. with Ba and Sr [*Sm19*], dielectric properties [*Sm19*, *Is3*]	
	T	5.535		25.72		*Is3*	$T = 520$ °C	
$K_{0.5}Bi_{2.5}Nb_2O_9$	O	5.506	5.506	25.26		*Au2*		
$Na_{0.5}Bi_{2.5}Nb_2O_9$	O	5.47	5.47	26.94		*Au2*		
$BaBi_2Ta_2O_9$	O	5.556	5.556	25.60		*Su4*	P&S [*Sm19*; *Su3*]	
$SrBi_2Ta_2O_9$	O	5.509	5.509	25.06		*Au2*	P&S [*Sm19*; *Su3*]	
$CaBi_2Ta_2O_9$	O	5.435	5.468	24.97		*Is3*	Dielectric properties	
	T	5.479		25.085		*Is3*	$T = 600$ °C	
$PbBi_2Ta_2O_9$	O	5.496	5.496	25.40		*Su4*	P&S [*Sm19*, *Su2*, *Su3*]	
Bi_3NbTiO_9	O	5.405	5.442	25.11		*Au2*	P&S [*Su3*, *Sm19*], dielectric properties [*Is11b*, *Is3*]	
Bi_3TaTiO_9	O	5.402	5.436	25.15		*Au2*	P&S [*Su3*], dielectric properties [*Is11b*]	
$BaBi_3Ti_2NbO_{12}$	T	3.874		33.70		*Su2*		
$PbBi_3Ti_2NbO_{12}$	T	3.867		33.55		*Su2*		
$Bi_4Ti_3O_{12}$	O	5.410	5.448	32.84		*Au3*	Dielectric properties [*Kr1*, *Su4*, *Sm19*, *Va11*], S.S. with $BaTiO_3$ [*Is6*], S.S. with $Pb_2Nb_2O_7$ [*Su1*], tetragonal at 675 °C [*Su1*], Electrooptic properties [*Cu2*], switching behavior [*Cu1*], monoclinic symmetry [*Cu2*]	
$BaBi_4Ti_4O_{15}$	T	5.461		41.85		*Su4*	P&S [*Su3*, *Sm19*, *Au4*, *Is6*, *Su2*]	
$SrBi_4Ti_4O_{15}$	T	5.428		40.95		*Su4*	P&S [*Su3*, *Sm19*]	
$CaBi_4Ti_4O_{15}$	T	5.418		40.75		*Su4*	P&S [*Su3*, *Sm19*]	
$PbBi_4Ti_4O_{15}$	T	5.437		41.35		*Su4*	P&S [*Su2*, *Sm19*, *Su3*]	
$Bi_5Ti_3GaO_{15}$	T	5.408		41.05		*Su4*	P&S [*Su3*]	
$Bi_5Ti_3FeO_{15}$	O	5.445	5.455	41.31		*Is12*	Tetr. $T > 740$ °C, Prop. [*Is11a*]	
$K_{0.5}Bi_{4.5}Ti_4O_{15}$	T	5.440		41.15		*Su4*	P&S [*Su3*]	
$Na_{0.5}Bi_{4.5}Ti_4O_{15}$	T	5.427		40.65		*Su4*	P&S [*Su3*, *Ha9*], structure determination [*Ne9*]	
$Ba_2Bi_4Ti_5O_{18}$	O	5.514	5.526	50.37		*Is6*	P&S [*Su3*], tetr. at 310 °C [*Is6*]	
$Ba_2Bi_4Ti_3Fe_2O_{18}$	O	5.490	5.500	50.185		*Is12*		
$Sr_2Bi_4Ti_5O_{18}$	T	5.461		48.80		*Su4*	Probably orthorhombic	
$Pb_2Bi_4Ti_5O_{18}$	T	5.461		49.70		*Su4*	P&S [*Su3*]	
$Ba_5Bi_4Ti_3Fe_5O_{27}$	O	5.491	5.502	76.20		*Is12*		

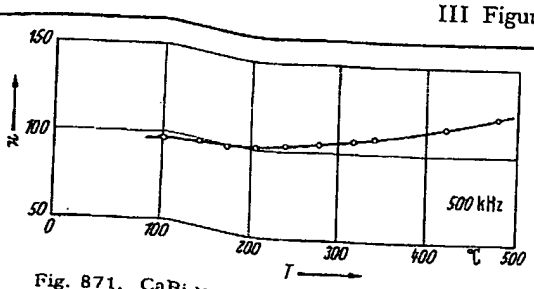

Fig. 871. $CaBi_2Nb_2O_9$ (ceramics). $\varkappa$ vs. T [61S11].

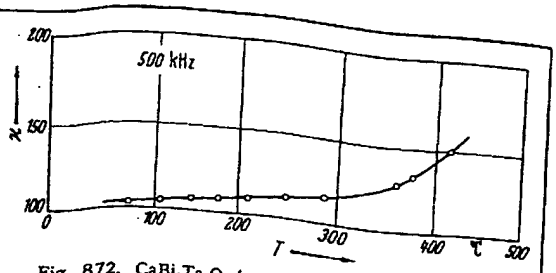

Fig. 872. $CaBi_2Ta_2O_9$ (ceramics). $\varkappa$ vs. T [61S11].

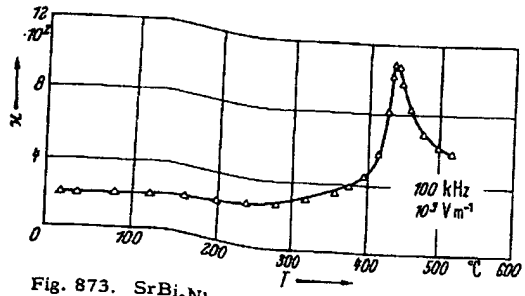

Fig. 873. $SrBi_2Nb_2O_9$ (ceramics). $\varkappa$ vs. T [62S17].

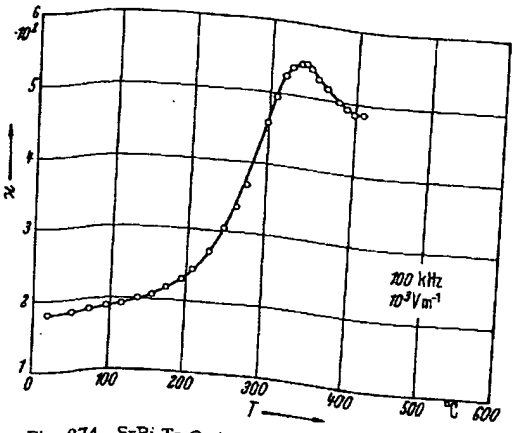

Fig. 874. $SrBi_2Ta_2O_9$ (ceramics). $\varkappa$ vs. T [62S17].

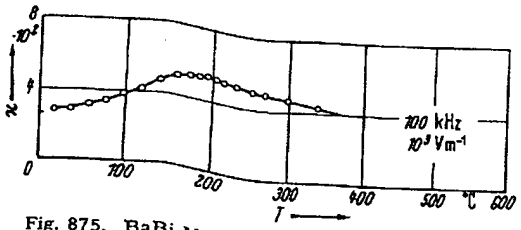

Fig. 875. $BaBi_2Nb_2O_9$ (ceramics). $\varkappa$ vs. T [62S17].

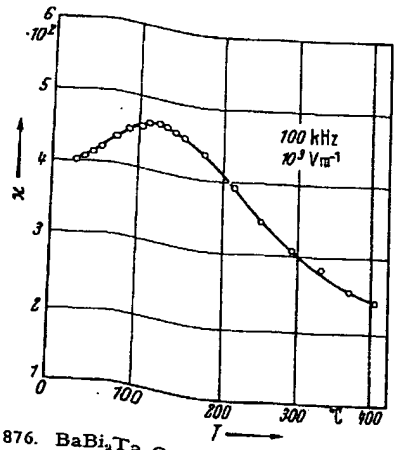

Fig. 876. $BaBi_2Ta_2O_9$ (ceramics). $\varkappa$ vs. T [62S17].

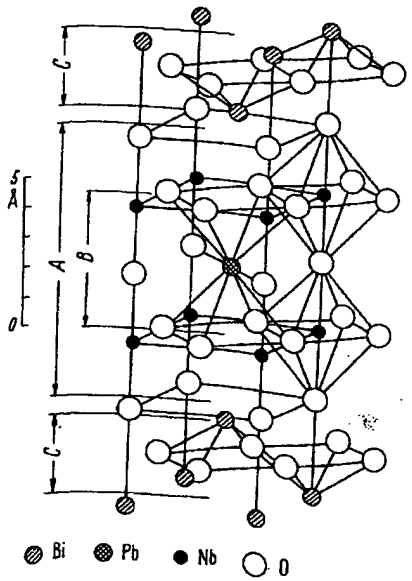

Fig. 877. $PbBi_2Nb_2O_9$. Schematic drawing of crystal structure. One half of the pseudotetragonal unit cell from $z \approx 0.25$ to $z \approx 0.75$ is given. A denotes the perovskite layer $PbNb_2O_7^{2-}$, B denotes a unit of hypothetical perovskite structure $PbNbO_3$ and C denotes $(Bi_2O_2)^{2+}$ layers [62S15].

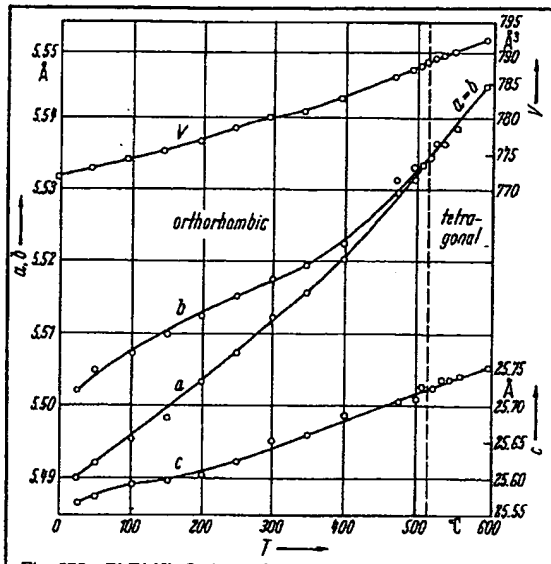

Fig. 878. $PbBi_2Nb_2O_9$ (ceramics). Lattice parameters vs. T [*6011*].

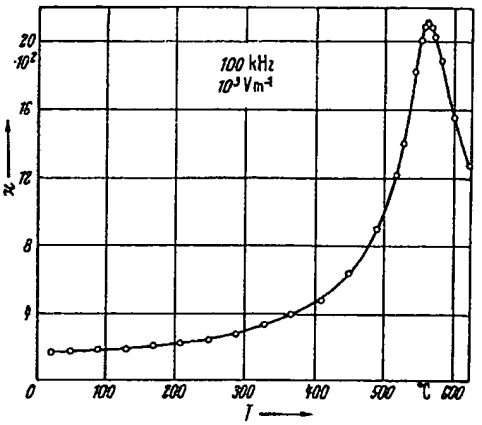

Fig. 879. $PbBi_2Nb_2O_9$ (ceramics). $\varkappa$ vs. T [*62S17*].

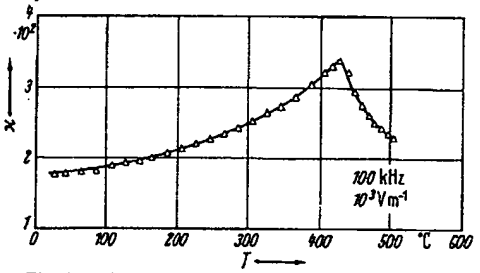

Fig. 880. $PbBi_2Ta_2O_9$ (ceramics). $\varkappa$ vs. T [*62S17*].

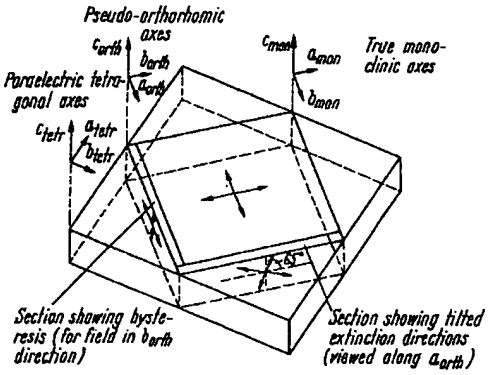

Fig. 881. $Bi_4Ti_3O_{12}$. Relationship between the three sets of crystallographic axes [*67C6*].

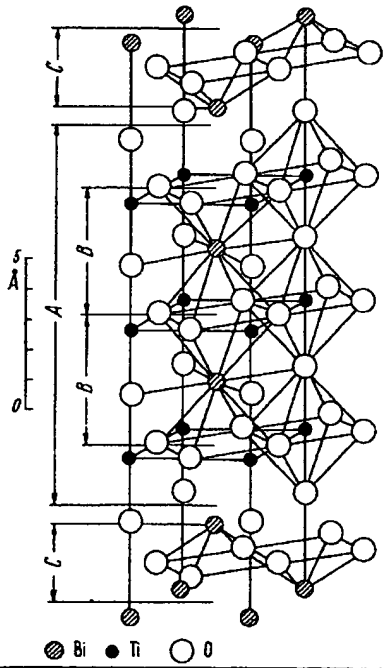

Fig. 882. $Bi_4Ti_3O_{12}$. Schematic drawing of crystal structure. One half of the pseudotetragonal unit cell from $z \approx 0.25$ to $z \approx 0.75$ is given. A denotes the perovskite layer $Bi_2Ti_3O_{10}^{4-}$, B denotes a unit of hypothetical perovskite structure $BiTiO_3$ and C denotes $(Bi_2O_2)^{2+}$ layers [*62S15*].

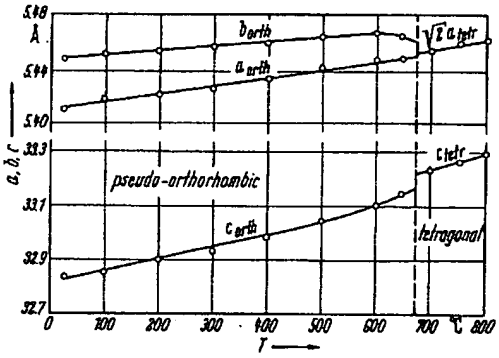

Fig. 883. $Bi_4Ti_3O_{12}$. Lattice parameters vs. T [*61S16*].

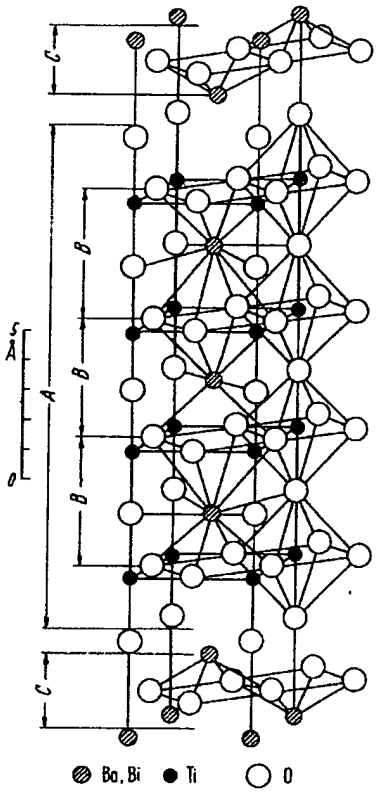

Fig. 890. $BaBi_4Ti_4O_{15}$. Schematic drawing of crystal structure. One half of the pseudotetragonal unit cell from $z \approx 0.25$ to $z \approx 0.75$ is given. *A* denotes the perovskite layer $BaBi_2Ti_4O_{13}^{2-}$, *B* denotes a unit of hypothetical perovskite structure $(Ba, Bi)TiO_3$, *C* denotes $(Bi_2O_2)^{2+}$ layers [*62S15*].

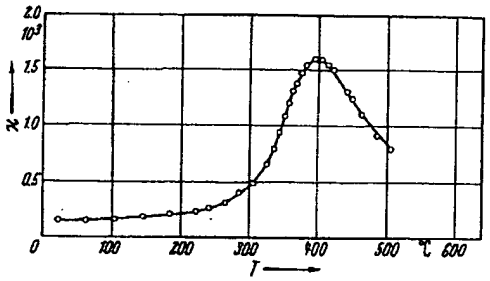

Fig. 891. $BaBi_4Ti_4O_{15}$ (ceramics). $\varkappa$ vs. T [*61S15*].

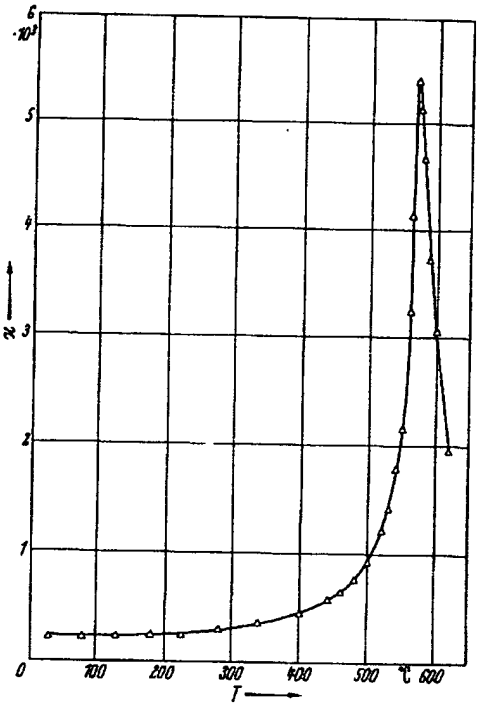

Fig. 893. $PbBi_4Ti_4O_{15}$ (ceramics). $\varkappa$ vs. T [*61S15*].

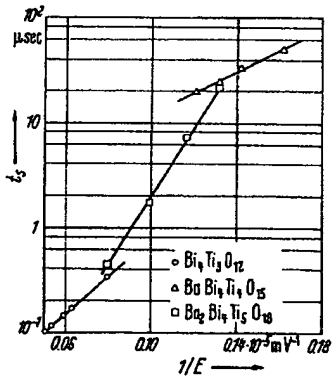

Fig. 892. $BaBi_4Ti_4O_{15}$, $Ba_2Bi_4Ti_5O_{18}$, $Bi_4Ti_3O_{12}$. t_s vs. $1/E$. [*62F1*]. t_s: switching time.

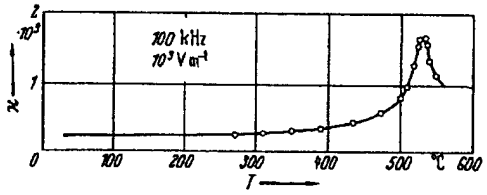

Fig. 894. $SrBi_4Ti_4O_{15}$ (ceramics). $\varkappa$ vs. T [*62S17*].

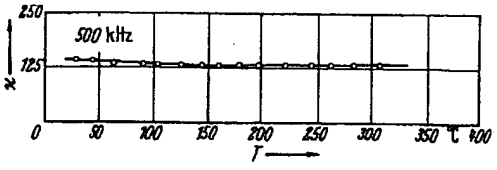

Fig. 895. $CaBi_4Ti_4O_{15}$ (ceramics). $\varkappa$ vs. T [*61S11*].

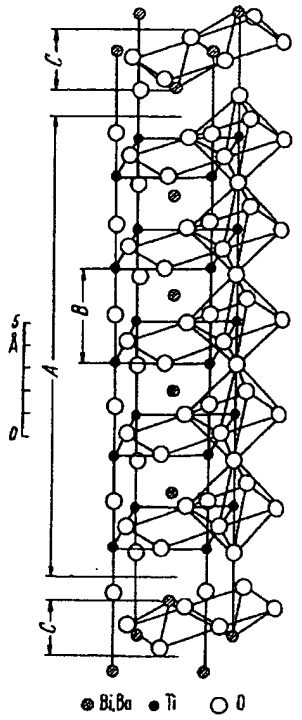

Fig. 896. $Ba_2Bi_4Ti_5O_{18}$. Schematic drawing of the crystal structure. One half of the tetragonal unit cell from $z = 0.25$ to $z = 0.75$ is given. *A* denotes the perovskitic layer of $Ba_2Bi_2Ti_4O_{16}^{2-}$, *B* denotes a unit cell of the hypothetical perovskite structure (Ba, Bi)TiO_3, and *C* denotes the layers of $(Bi_2O_2)^{2+}$ [*62A5*].

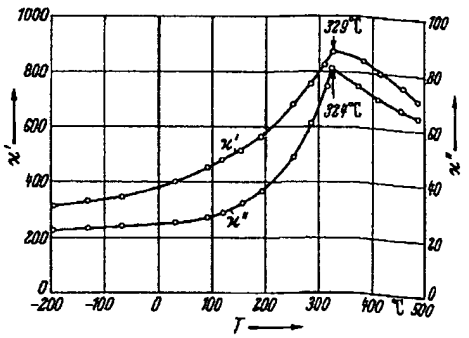

Fig. 898. $Ba_2Bi_4Ti_5O_{18}$. $\varkappa'$ and $\varkappa''$ vs. T [*62A5*].

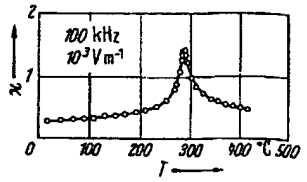

Fig. 900. $Sr_2Bi_4Ti_5O_{18}$ (ceramics). $\varkappa$ vs. T [*62S17*].

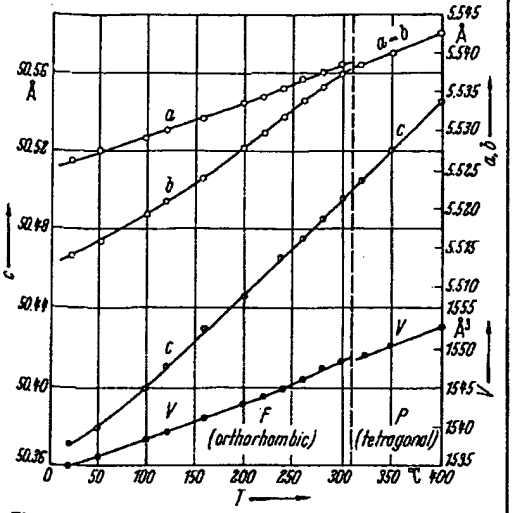

Fig. 897. $Ba_2Bi_4Ti_5O_{18}$. Lattice parameters vs. T [*63I5*].

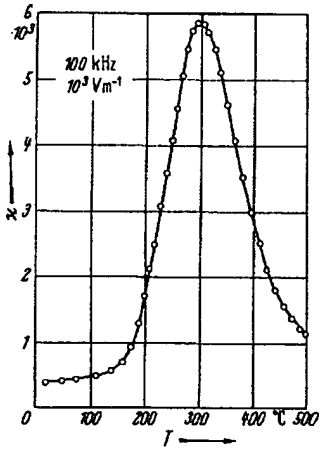

Fig. 899. $Pb_2Bi_4Ti_5O_{18}$ (ceramics). $\varkappa$ vs. T [*62S17*].

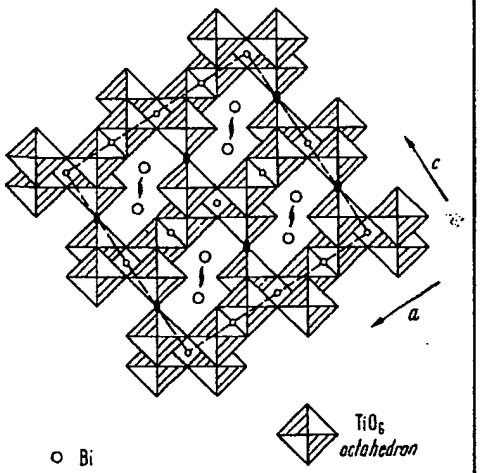

Fig. 901. $Bi_4Ti_4O_{11}$. Schematic projection of structure on $(010)_2$ [*65J4*].

This Page is Inserted by IFW Indexing and Scanning Operations and is not part of the Official Record

BEST AVAILABLE IMAGES

Defective images within this document are accurate representations of the original documents submitted by the applicant.

Defects in the images include but are not limited to the items checked:

- ☑ BLACK BORDERS
- ☑ IMAGE CUT OFF AT TOP, BOTTOM OR SIDES
- ☐ FADED TEXT OR DRAWING
- ☑ BLURRED OR ILLEGIBLE TEXT OR DRAWING
- ☐ SKEWED/SLANTED IMAGES
- ☑ COLOR OR BLACK AND WHITE PHOTOGRAPHS
- ☐ GRAY SCALE DOCUMENTS
- ☐ LINES OR MARKS ON ORIGINAL DOCUMENT
- ☐ REFERENCE(S) OR EXHIBIT(S) SUBMITTED ARE POOR QUALITY
- ☐ OTHER: _____

IMAGES ARE BEST AVAILABLE COPY.
As rescanning these documents will not correct the image problems checked, please do not report these problems to the IFW Image Problem Mailbox.